

A REVIEW OF COMPRESSIBLE DYNAMIC STALL CONTROL PRINCIPLES AND METHODS

M.S.Chandrasekhara

Navy-NASA Joint Institute of Aerospace Sciences
Department of Mechanical and Astronautical Engineering
Naval Postgraduate School, Monterey, CA, 93943, USA

ABSTRACT: Different methods of controlling dynamic stall are reviewed. Starting from fundamental principles of flow control, the methods with typical results obtained in the compressible dynamic stall facility are discussed.

1. INTRODUCTION

Dynamic stall is a complex, unsteady fluid mechanics problem involving the rapid production and transport of unsteady vorticity over an airfoil when it is pitched past the static stall angle. It can be induced by many different mechanisms depending on the flow conditions, [1]. However, as described in it, the abrupt coalescence of the unsteady vorticity is common to all onset mechanisms. Control of the problem is important to helicopters, maneuvering aircraft, wind turbines and turbomachinery. The passage of the dynamic stall vortex over the airfoil produces a large, nose-down pitching moment on the airfoil and can lead to unpredictable fatigue failure. This has primarily prevented designers from harnessing the significant lift increases associated with the phenomenon, which is its major benefit and reason for all the studies.

The dominance of the dynamic stall vortex in the flow dictates that exploiting the benefits of the phenomenon requires careful management of flow vorticity. This is because once the vorticity flux level exceeds a certain critical value (which is generally unknown and depends on the flow parameters); the vorticity coalesces into a vortex. Once a vortex forms, the flow cannot be controlled. However, if this vorticity can be diffused prior to this event, either through the boundary layer or in some other appropriate fashion, it might provide a way to control the flow. Since vorticity is an intractable quantity, indirect methods are required to estimate its levels in the flow to achieve this goal. Ref. 2 offers a way towards this by establishing that the vorticity flux at the surface is related to the adverse pressure gradient as follows:

$$\nu \frac{\partial \Omega}{\partial n} = \frac{\partial U_s}{\partial t} + \frac{1}{\rho} \frac{\partial p}{\partial s} + V\Omega$$

Here, the LHS is the vorticity flux, the first term on the RHS is the surface tangential acceleration, the second, the potential flow pressure gradient and the last term, represents the surface transpiration. According to [2], the first term is responsible for the generation of vorticity in the Stokes layer, which then diffuses outwards across the boundary layer. The vorticity produced by the third term is exactly balanced by the span-mean convection term and hence does not contribute directly to vorticity management. The way a flow is controlled by suction is through keeping the vorticity close to the surface. The most significant contribution to the whole process comes from the pressure gradient term. The vorticity flowing through the boundary layer arises from the strong pressure gradient near the leading edge. An order of magnitude estimate shows that the surface acceleration term is about one order smaller than the pressure gradient term. Consequently, for any flow control technique to be successful, the flow pressure gradient needs to be manipulated. However, the fixed geometry of the wing or airfoil makes it normally impossible. Thus, compressible dynamic stall is inherently a challenging task.

Many steady flow control methods exist, but the large amounts of vorticity involved due to the unsteady leading edge motion in this problem have primarily been the limitation why these are not directly applicable to the dynamic stall problem, especially when shocks are present. As part of a continuing study in the Navy-NASA Joint Institute of Aerospace Sciences, several new approaches were attempted and this paper describes each one of them along with the results obtained. These are the Dynamically Deforming Leading Edge (DDLE) airfoil, the slatted airfoil, the airfoil with zero-mass flux synthetic jet and the Variable Droop Leading Edge (VDLE) airfoils. In addition, a micro-jet blowing study was also conducted.

2. DESCRIPTION OF THE DIFFERENT APPROACHES

The experiments were conducted in the Joint Institute's Compressible Dynamic Stall Facility (CDSF). The CDSF is an in-draft wind tunnel with a 0.35 m x 0.25 m test section, operated by a

continuously running evacuation compressor. The airfoil is oscillated sinusoidally using an electro-mechanical drive system. The speed range of the CDSF and the oscillation parameters are: $0 \leq M_\infty \leq 0.5$, $0^\circ \leq \alpha_{\text{mean}} \leq 15^\circ$, $2^\circ \leq \alpha_{\text{amplitude}} \leq 10^\circ$, $0 \leq f \leq 100$ Hz, (a reduced frequency, $k = \pi fc/U_\infty = 0.15$ at $M_\infty = 0.5$). These are appropriate for the retreating blade flow over a helicopter. The tunnel is equipped with other necessary instrumentation. A brief description of the models is provided below before the results are described.

2.1 THE DDLE Airfoil

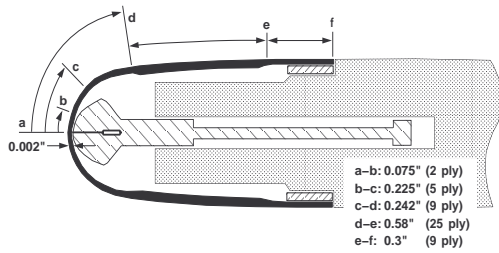


Fig. 1. Schematic of the DDLE airfoil (Ref. 3)

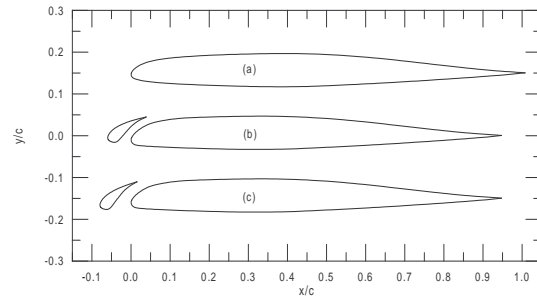


Fig. 2. Slatted airfoil profiles: (a) RC(6)-08; (b) RC(6)-08/106, 6 deg slat; (c) RC(6)-08/210, 10 deg slat (Ref.4)



Fig. 3. The NACA 0015 airfoil model with blowing slot (Ref. 5)

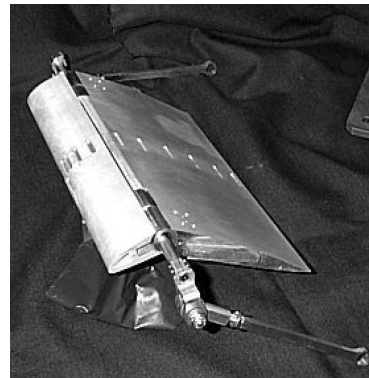


Fig. 4. Assembled VDLE airfoil (Ref. 6)

The Dynamically Deforming Leading Edge (DDLE) airfoil is a derivative of a 0.15 m chord NACA 0012 airfoil. Its leading 20% is cast from a carbon-fiber composite; the rest is machined from solid metal. The composite fiber airfoil leading edge is attached with a tang to a mandrel (housed inside the airfoil) shaped to the NACA 0012 profile (see Fig. 1). The stepper motor driven mandrel translates in the chordwise direction by less than 0.002 m to produce up to 320% continuous change in the airfoil leading edge radius. More details about the DDLE airfoil design can be found in Ref. 3.

2.2 The Slatted Airfoils

The slatted airfoils are special rotorcraft airfoil, identified as RC(6)-08/106 and RC(6)-08/210. (See Ref. 4 for an explanation of the notations. Two slat configurations were tested, along with the basic airfoil (RC(6) series). One had a 6 deg slat (106-series) and the other, 10 deg. These airfoils are shown in Fig. 2. All models had a 0.076 m chord.

2.3 Airfoil with Synthetic Jets

Two separate airfoil models, the NACA 0012 airfoil and the NACA 0015 airfoil were tested, but only the results for the 0.15 m chord NACA 0015 airfoil will be discussed. A 0.0005 m wide slot at $x/c = 0.033$ was used to introduce oscillatory blowing produced by a custom built actuator at 20° to the local tangent on the airfoil upper surface. The slot covered 98% of the tunnel span, with end caps at each end. The inside of the maximum thickness portion of the airfoil was used to create a plenum chamber and a contraction leading to the slot, as can be seen in Fig. 3. Air was fed into the plenum through the end caps. A Kulite unsteady pressure transducer provided an indication of the dynamically varying airfoil peak suction pressure and also the fluctuations of the plenum pressure due to the introduction of oscillatory blowing. A comparison of this pressure with the no-blowing case provided an indication of the success (or lack of it) of the method. See ref. 5 for more details.

2.4 The VDLE Airfoil

The VDLE airfoil is also a 0.15m chord VR-12 airfoil spanning the wind tunnel. The leading 25% of the airfoil rides on a hinge at the quarter-chord point to produce various droop angles. The hinge attaches to the main element, which is held in the CDSF windows and oscillates synchronously with them. 20 Kulite unsteady pressure transducers at selected locations provide the airfoil pressure distributions. The sensor electrical leads pass through the hollow hinge-shaft on the drooping front portion of the airfoil, which also protrudes from the CDSF windows. Fig. 4. It is linked to drive arms on both sides of the test section. When the arms are anchored to the windows, a fixed leading edge droop angle results, on the other hand, if the arms are anchored to the stationary tunnel sidewalls, a sinusoidally varying leading edge droop is obtained. The conditioned analog signal from the sensors were simultaneously acquired using a high speed A-D converter along with a digital encoder signal that provides the airfoil instantaneous angle of attack information. Since absolute pressures were measured, considerable care was taken during calibration and experimentation to account for changes in ambient pressure (caused by weather), noise, drift and other such extraneous factors, ref. 6.

For all cases, quantitative flow visualization was conducted using the Point Diffraction Interferometry (PDI) technique. PDI is a real-time technique and can produce a large number of flow interferograms that can be later analyzed for nonintrusively determining the quantitative flow pressures.

III. RESULTS AND DISCUSSION

3.1 THE DDLE Airfoil Flow



Fig.5. Comparison of flows over the NACA 0012 and the DDLE airfoils, $M = 0.4$, $k = 0.05$;
(a) $\alpha = 10.5^\circ$, (b) $\alpha = 13^\circ$, Shape = 3.5

An important variable in compressible dynamic stall control is the airfoil leading edge radius. It determines the leading edge potential flow distribution for a rotor blade profile and clearly governs the flow. To identify the range of radii (denoted by increasing shape numbers for increasing radii) for which the flow remained attached at different Mach numbers, steady flow experiments were first conducted. This allowed the determination of an attached flow envelope as a function of leading edge radius for each freestream Mach number. Based on the knowledge that there is a delay in the flow development under unsteady flow conditions, the shape was varied appropriately. A typical result at $M = 0.4$ and $k = 0.05$ is shown in the PDI images of Fig. 5 [3]. These represent quantitative density field lines in the flow and also serve as a useful flow visualization images. Even though the freestream flow is subsonic, shock induced dynamic stall onset for the NACA 0012 airfoil at $\alpha = 10.5^\circ$ is clear in Fig. 5a, whereas in Fig. 5b, for a

slightly rounded airfoil (when leading edge is retracted by about 0.00025 m) – shape 3.5, the flow over the DDLE airfoil has just entered the same state, but at a higher α of 13° indicating a delay of about 2.5° in stall onset. Thus notable benefits were achieved. In fact, for the $M = 0.3$, $k = 0.1$ case, no dynamic stall occurred for the whole cycle of $\alpha = 10^\circ + 10^\circ \sin \omega t$. The PDI images were quantitatively evaluated for pressure distributions from which the vorticity fluxes were calculated, which show that the peak values over the DDLE airfoil were considerably – 50% lower (ref. 3) than that over the basic NACA 0012 airfoil.

3.2. The Slatted Airfoil Flow

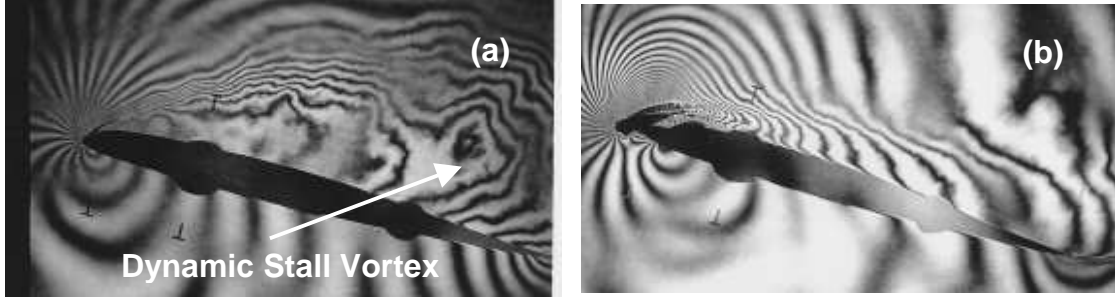


Fig. 6. PDI images of dynamic stall flow over RC(6)-08 Airfoil; $M = 0.4$, $k = 0.05$
(a) No slat, $\alpha = 14.5^\circ$, (b) 10-deg slat, $\alpha = 16.4^\circ$, attached flow

Figures 6a and 6b present two PDI images of the slatted airfoil flow for $M = 0.4$, $k = 0.05$. The basic airfoil without a slat experiences deep dynamic stall as is clear from the large dynamic stall vortex core indicated in Fig. 6a for $\alpha = 14.5^\circ$. The purpose of the slat is to mitigate the tendency of the airfoil to reach this state and it can be seen from the image in Fig. 6b for the case of the 10-deg slat, the flow remains fully attached at $\alpha = 16.4^\circ$, even when the slat itself experiences incipient separation. The primary reason for this difference is the natural blowing through the slat passage that energizes the local boundary layer. In this case, no additional momentum was supplied to the flow as blowing occurs due to the pressure difference between the near stagnation conditions at the slat and the lower pressure at the slat trailing edge. A sizeable lift benefit can be expected for this case due to the attached flow at the higher angle of attack. The cost of this benefit is the extra appendage that has to be carried throughout the oscillation cycle and its drag. Detailed analysis of this flow has shown [4] that the main element airfoil pressure distribution is modified significantly due to the resulting geometry and the bleed flow, with the result that the vorticity flux is also altered.

3.3 Flow over Airfoil with Synthetic Jets

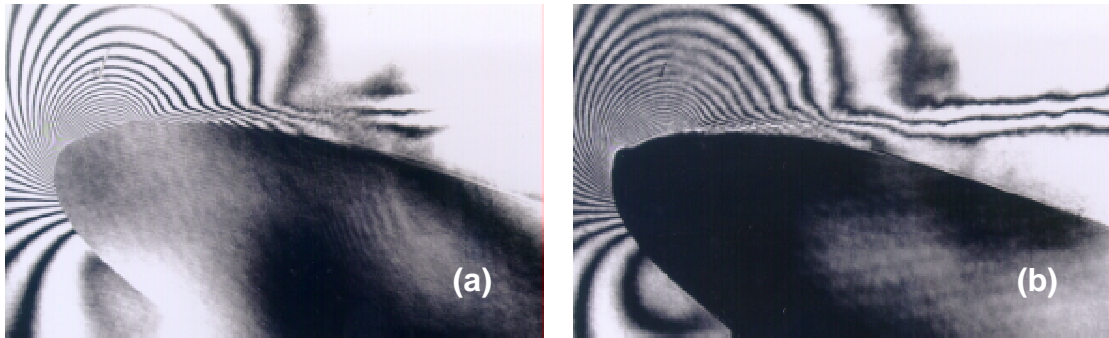


Fig. 7. PDI images of flow over NACA 0015 airfoil, $M = 0.3$, $k = 0.05$
(a) No blowing, $\alpha = 21.5^\circ$ (b) Oscillatory blowing at $F^+ = 0.7$, back pressure = 1.3.2 psia, $\alpha = 22.5^\circ$

In using synthetic jets to produce oscillatory blowing and control flow separation, it has been recommended by other researchers [5] that the blowing momentum coefficient $C_\mu (= U_j^2 h / U_\infty^2 c)$ should be $O(0.01\%)$ and the non-dimensional blowing frequency $F^+ (= f_{\text{blowing}} X_{\text{slot-trailing edge}} / U_\infty)$ should be ≈ 0.6 .

1. These are very demanding stipulations for any actuator that is used for the purpose; especially as the freestream Mach number increases. The airfoil does not stall fully for $\alpha = 20^\circ$ and hence, it was oscillated about a mean angle of 15° with an amplitude of 10 deg. The study first focused on the ability of the approach to control a lower Mach number flow at $M = 0.3$. The virtually identical interferograms presented in Fig. 7 for one-degree angle of attack difference show that the technique is only minimally successful. In fact, for all momentum and non-dimensional frequency parameters that were possible with the actuator in hand, the results were not positive. These negative results deferred any further work until the availability of a more powerful actuator.

3.4 VDLE Airfoil Flow

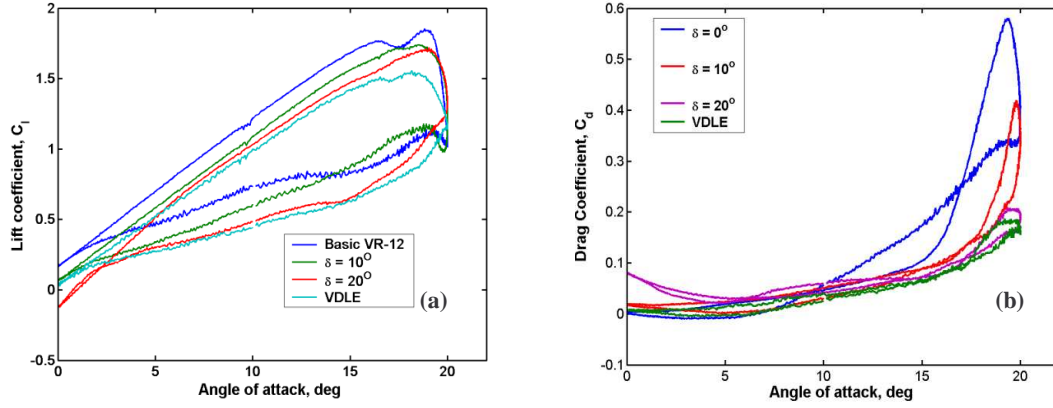


Fig. 8. Lift and Drag coefficients for the VDLE airfoil compared with basic VR-12 airfoil at different leading edge droop settings, $M = 0.3$, $k = 0.1$; (a) C_l , (b) C_d

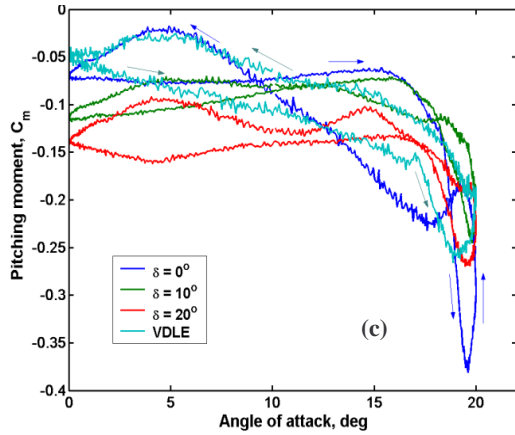


Fig. 8c. Pitching moment coefficients for the VDLE airfoil compared with basic VR-12 airfoil

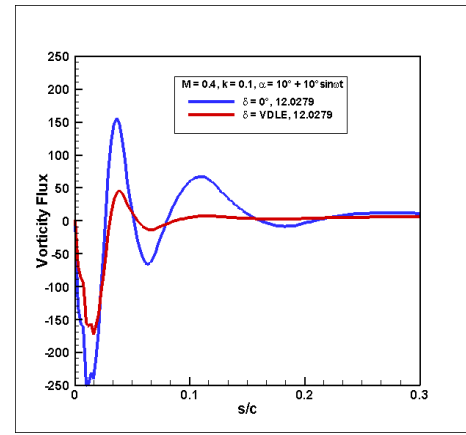


Fig. 9. Distributions of vorticity flux over the VR-12 and the VDLE airfoils, $M = 0.4$, $k = 0.1$

The VDLE airfoil was tested for a range of Mach numbers and reduced frequencies with pressure data collected from which the lift, drag and pitching moment coefficients were calculated using standard methods. These are shown in Figs. 8a, 8b and 8c respectively. Fig. 8a compares the cases at different fixed droop angles also, to show the effect of leading edge droop. It is clear that C_l values as high as 1.8 are attained with the basic airfoil and the values are about 10% larger than the corresponding VDLE airfoil. The maximum C_l progressively decreases with increasing droop angle. Fig. 8b shows that the drag on the basic airfoil is about 3-4 times that of the VDLE airfoil. The simple reason being the absence of the dynamic stall vortex which causes the basic airfoil wake to be substantially wide and hence, the large

drag. The **absence** of the dynamic stall vortex is borne out by Fig. 8c, where the pitching moment over the airfoils under comparison shows a much smaller value over the VDLE airfoil. The vortex, when present, convects over the airfoil and induces the large fluctuations in the pitching moment, the stated source for all structural failures if dynamic stall is allowed to occur on a blade. Of even greater value is the counter clockwise pitching moment loops, indicative of positive damping that actually alleviates the problems encountered with vortex convection. Once again, the favorable result demonstrated here is due to the gross instantaneous potential flow changes brought about by the drooping of the airfoil leading edge suitably.

A comparison of the vorticity flux for $M = 0.4$, $k = 0.1$ is presented in Fig. 9 which clearly shows that values over the VDLE airfoil upper surface are about $1/3^{\text{rd}}$ of those over the basic airfoil. It also establishes that much of the vorticity flux is generated around the leading edge, where the suction peak forms. The lower peak vorticity flux represents a lower lift also as was seen from Fig. 8a, but the critical need here is the avoidance of the dynamic stall vortex at large angles of attack. The VDLE approach has succeeded in managing the vorticity production over the airfoil, and also distributing the vorticity field satisfactorily because the lift is only 10% smaller, even though the peak vorticity flux is one-third of that of the basic flow field. Through this process, it has effectively delayed the development of the pressure field that would be encountered by the basic airfoil to higher angles of attack. The much decreased drag coefficient implies that the VDLE airfoil L/D performance is significantly superior as well.

IV. CONCLUSIONS

Four approaches of unsteady compressible flow control have been discussed. The approaches were applied to helicopter rotor blade sections under the same flow conditions. Three of these, the DDLE airfoil, the slatted airfoil and the VDLE airfoil demonstrated significant ability to control and delay the onset of compressible dynamic stall. The most improvement was obtained with the VDLE concept where the drag was also reduced by 75%. The pitching moment data pointed to positive damping as also one of the results. In both these methods, the vorticity flux was found to be lower than when no control was employed over the baseline airfoil. The slatted airfoil also used the natural blowing to produce the desired effects. The use of synthetic jets under compressible flow conditions was not found to be practical.

ACKNOWLEDGMENTS: This research was supported by the U.S. Army Research Office and the Army Aeroflightdynamics Directorate through grants to the Naval Postgraduate School. The contributions of Dr. M.C.Wilder and Dr. L.W.Carr to this research are highly appreciated.

REFERENCES

- [1] Chandrasekhara MS, Wilder MC, Carr, LW, Competing mechanisms of compressible dynamic stall, *AIAA J*, 1998, 36(3), 387-393.
- [2] Reynolds WC, Carr LW, Review of unsteady, driven, separated flows, AIAA-85-0527, 1985.
- [3] M.S.Chandrasekhara, M.C. Wilder and L.W.Carr, "Compressible Dynamic Stall Control Using Dynamic Shape Adaptation", (AIAA Paper 99-0655), *AIAA Journal*, Vol. 39, No. 10, pp. 2021-2024, Oct. 2001.
- [4] Chandrasekhara MS, Wilder MC, Carr LW, Compressible dynamic stall control using a shape adaptive airfoil, AIAA-99-0655, 1999.
- [5] M.S.Chandrasekhara, Fluid Mechanics of Compressible Dynamic Stall Control Using Dynamically Deforming Airfoils", Final Report submitted to ARO, Nov. 2001.
- [6] M.S. Chandrasekhara, P.B. Martin and C. Tung, "Compressible Dynamic Stall Control using a Variable Droop Leading Edge Airfoil", AIAA Paper No. 2003-0048, to appear in *Journal of Aircraft*,

MIXING ENHANCEMENT OF TWO LIQUIDS BY ACTIVE CONTROL IN A MILLIMETER-SCALE CHANNEL FLOW

T. Kaneko, S. Izawa, A. K. Xiong and Y. Fukunishi

Department of Mechanical Engineering, Tohoku University, Sendai 980-8579, Japan

ABSTRACT: The aim of this study is to develop a technique to enhance the mixing in a millimeter-scale channel by active control. In the mixing channel, liquids from two tanks are mixed. One of the tanks is sinusoidally moving vertically changing the flow rate. The effects of channel geometry and the period of sinusoidal forcing on the mixing are examined experimentally. It is shown that the most effective mixing can be accomplished by stratification of two liquids.

1. INTRODUCTION

Enhancement of mixing at very small-scale environment is a key issue in the field of biochemical engineering. The diffusion caused by turbulence cannot be expected because of the extremely low Reynolds number. The general approach has focused on increasing the interface between the two streams to optimize the effect of their molecular diffusion. Based on this strategy, Liepmann et al. used the pulsatile flow micropump activated by a bubble to deliver well-mixed fluids [1]. Branebjerg et al. tried to increase contact area by stratification of reagents and to approach the layer thickness to molecule diffusion length [2]. Using zigzag channel, Hubert et al. attempted to generate the recirculation area at the each angle and realize mixture advancement [3]. Although, they were successful in improving the mixing rate in their microchannels, those systems require a precise processing of the flow channel or a complicated control of the reagent. Compared with other methods, the approach in this research is much more simple. One of the tanks connected to the mixing flow channel is elevated up and down to create a sinusoidal wavy interface. Then the flow is lead to a path with a special configuration to enhance mixing. This study highlights on hydromechanical analysis of mixing process where chemical reaction is absent.

2. EXPERIMENT

Fig.1 is a schematic of the experimental setup. Tank A and B are filled with water colored by blue ink and normal water, respectively. Both liquids flow into the "mixing" channel and discharged to tank C. The valve shown in the figure adjusts the flow rate. Tank A moves up and down periodically with the amplitude H and period T by the traversing mechanism, while tank B is kept at rest. Flow channel is inscribed in an acrylic resin plate surface using a milling machine. Digital camera connected to a microscope is used to take photographs of the flow.

The following method was used to take the matching between the real mixture-ratio of the two liquids and the brightness observed at each observation point. The brightness was measured

against mixed liquids of various mixture-ratio R_m described by the following equation,

$$R_m = V_A/(V_A + V_B)$$

where, V_A and V_B are the volume of liquid A and B, respectively. Fig.2 shows the relation between the brightness and the mixture-ratio R_m . As the R_m increase, the brightness elements R (Red) and G (Green) decrease while B (Blue) increase. Therefore, it can be found that their ratio $2B/(R+G)$ increases almost linearly with mixture-ratio R_m , as shown in Fig.3. The straight line in the figure is obtained using the least square method. So, mixture-ratio can be obtained by measuring the relative brightness $2B/(R+G)$.

The Reynolds number based on typical channel width is in the range of 1-10 for all experiments.

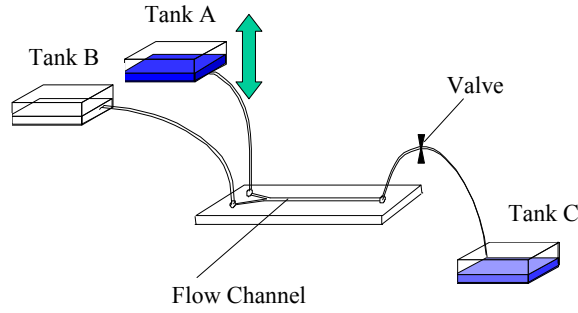


Fig. 1: Experimental equipment. Tank A is attached to the traversing mechanism.

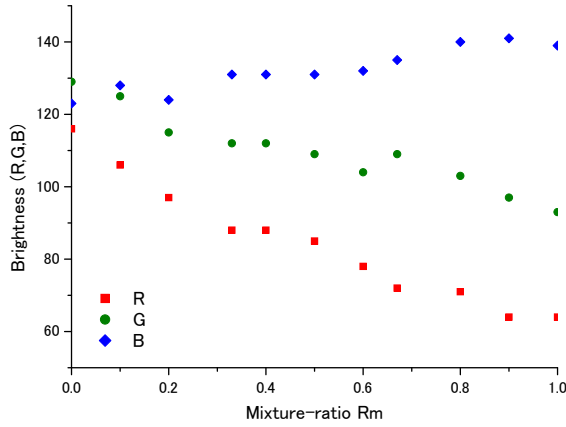


Fig. 2: Relation between brightness of the color-components and the mixture-ratio

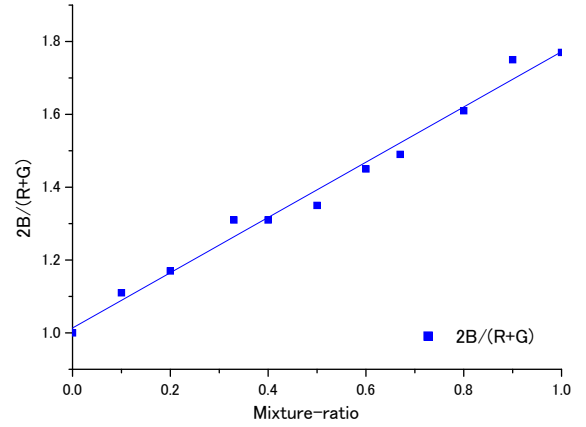


Fig. 3: Relation between mixture-ratio and relative brightness $2B/(R+G)$

3. RESULT AND DISCUSSION

3.1 Effects of Periodical Forcing

The first experience was carried out using a Y type channel which has a straight mixing section. The schematic is shown in Fig.4. Colored water (liquid A) and normal water (liquid B) meet at a junction (point **a**) and flow through the straight channel (point **b**). Fig.5 shows the flow patterns at each observation point. When the tank A is at rest, that is without sinusoidal forcing, a clear interface between the two liquids can be observed even in the down stream area [(1-b)]. Once tank A begins to move sinusoidally, the interface at the junction starts to make a wavy motion as shown in Fig.5(2-a) and this wavy pattern travels in the downstream direction. This leads to the increase of the contact area, and more mixing can be observed in the downstream area compared to the case without perturbation.

Fig.6 shows the profile of the mixture-ratio R_m at the cross-section near the outlet, point **b** in Fig.4. Z axis is normalized by the half width of the channel. The R_m profile without control case changes rapidly near the center of the flow channel, $Z = 0$. On the other hand, this transition becomes more gradual as the period of disturbance increase. If the two liquids are completely mixed with each other, R_m will become constant everywhere. So, the gradient of R_m will be used as the indicator of the mixing-enhancement effect.

Fig.7 shows the effect of periodical disturbance on the mixing enhancement of Y type channel. The mixing effect is clearly larger when control is taking place, compare to the no-control case. It can be found that the mixing is greatly enhanced by the sinusoidal forcing. It can also be found the amplitude does not have much influence on the mixing within $3 \leq T \leq 8$. The following experiments were carried out under the same amplitude $H = 4[\text{mm}]$.

3.2 Channel Geometry Effect

Three types of channels shown in Fig.8 are tested to investigate the effects their geometry have on the mixing. The flow patterns are observed at the point marked by a circle in each channel (Fig.9). It can be found that two liquids flow out without mixing when the periodical forcing is not imposed for all cases. Clear interfaces can be found. On the other hand, under periodical forcing, the interfaces becomes wavy which brings increase on the contact areas. These wavy patterns can be found regardless of the channel geometry. In the orthogonal type channel, the parabolic profile appears alternately. As for the trumpet type, the interface is stretched in the vertical direction of the figure. This snake-like pattern leads to the rapid increase of contact area. The stratification process similar to the trumpet type takes place when the flow passes over a cavity. Fig.10 shows the mixing effect caused by these channels. As the period of vibration T increase, two liquids are mixed more efficiently. The channel with cavities is found to be the most effective among the models tested. It is because the stratification process takes place at each cavity, over and over.

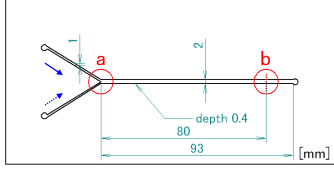


Fig. 4: The schematic view of Y type channel. The observation points are shown by \circ . The solid-line arrow and the dashed arrow show the flow directions of liquid A and B, respectively. The dashed lines denotes the location where the mixture-ratio profile is analyzed.

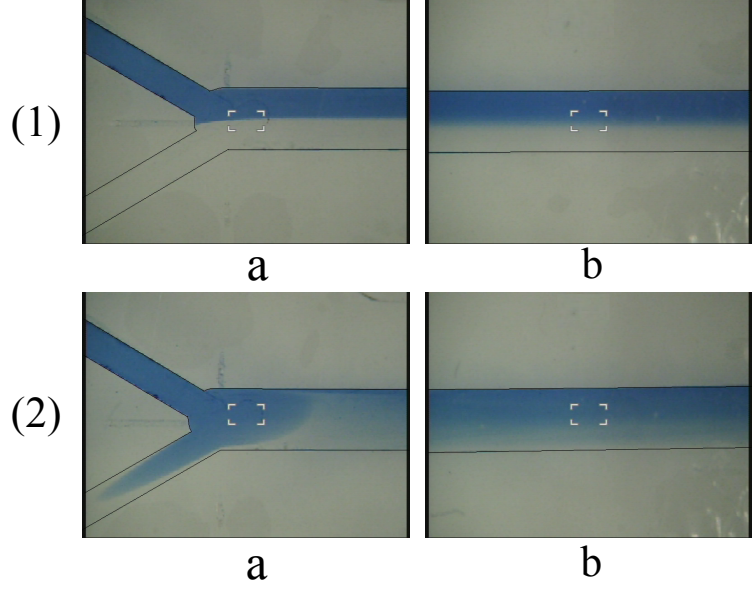


Fig. 5: Flow patterns using Y type channel. Period $T = 4$ [s]. (1) No oscillation, (2) With oscillation ($H = 4$ [mm] and $T = 4$ [s])

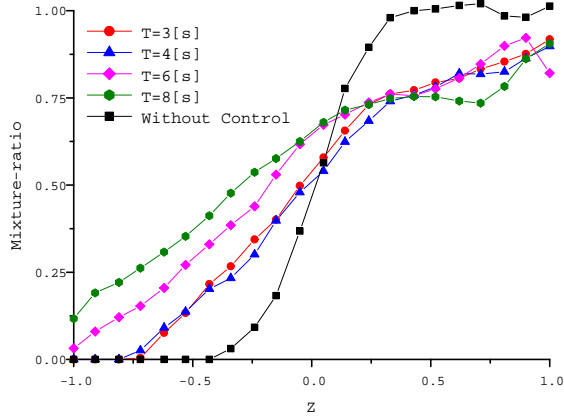


Fig. 6: Profile of the mixing ratio under periodical disturbance ($H = 4$ [mm]) measured at point b in Fig.4

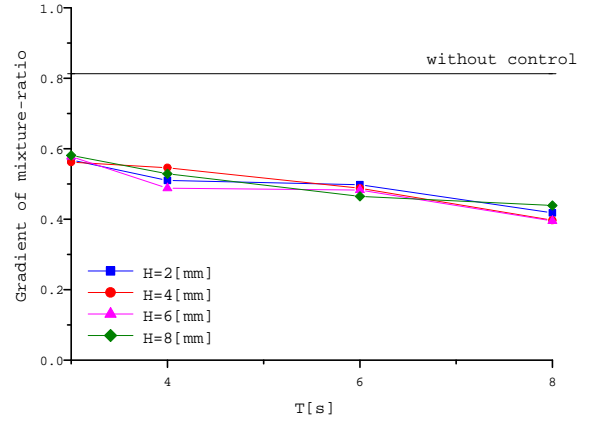


Fig. 7: The effect of periodical disturbance on the mixing enhancement of Y type channel

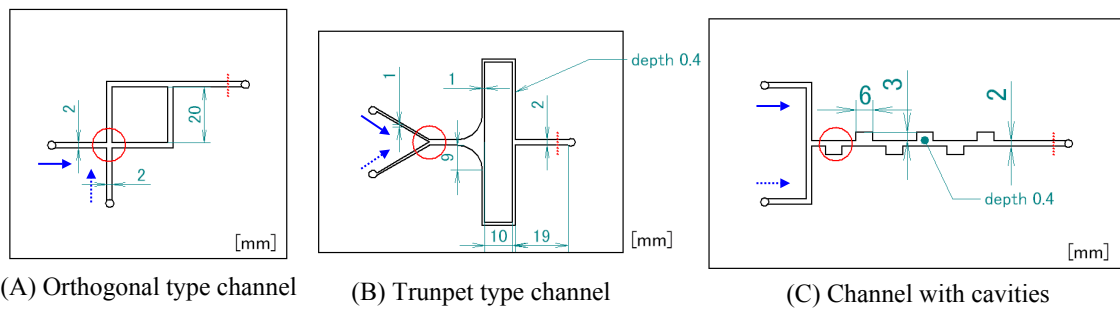


Fig. 8: The schematic view of three channels. The observation points are shown by \bigcirc . The solid-line arrow and the dashed arrow show the flow directions of liquid A and B, respectively. The dashed lines show the locations where the mixture-ratio profiles are analyzed.

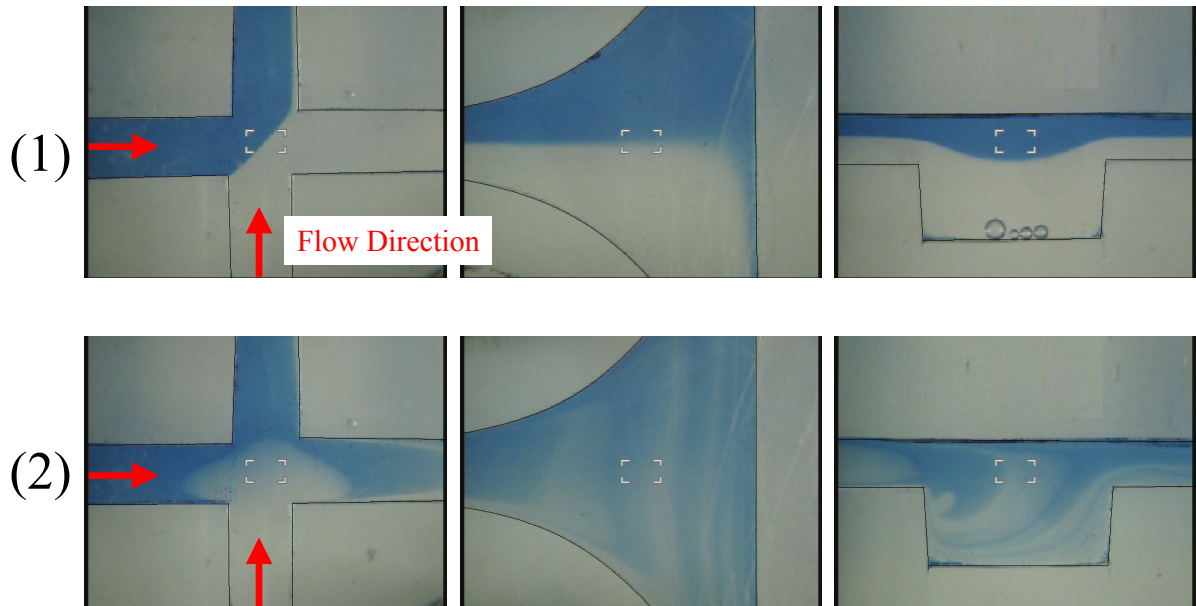


Fig. 9: Flow patterns at each observation point. (1) No oscillation, (2) With oscillation ($H = 4$ [mm] and $T = 4$ [s])

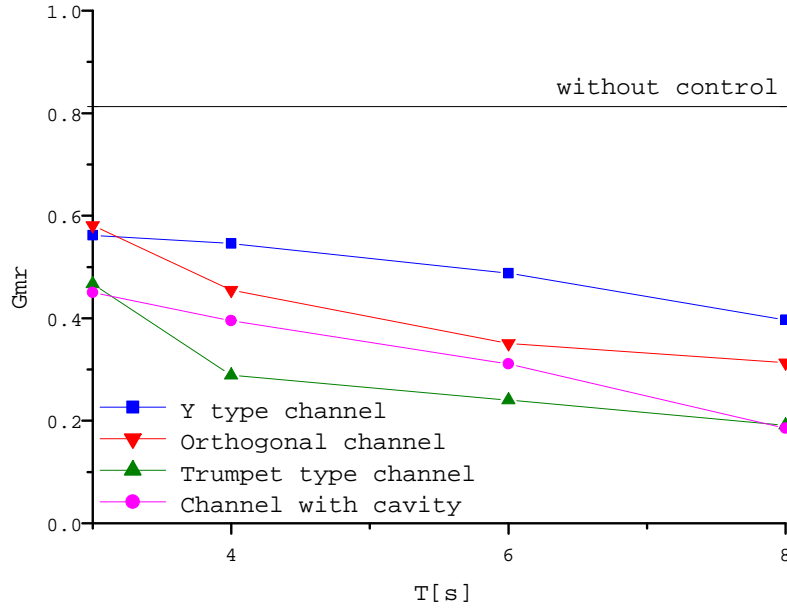


Fig. 10: The mixture-ratio gradient at $H = 4$ [mm].

4. CONCLUSION

Using a millimeter-scale channel, a simple and efficient method for mixing enhancement was developed. It was found that imposing sinusoidal forcing to the flow, the contact area of two liquids can be increased and the mixing enhanced. The channel geometry was changed to find a better configuration of the channel, and the best result was obtained when the channel with cavities was used.

REFERENCES

- [1] Desmukh, A. A., Liepmann, D. and Pisano, A. P., Solid-State Sensor and Actuator Workshop, Hilton Head, SC, 2000, pp.73-76.
- [2] Branebjerg, J., Gravesen, P., Krong, J., Nielsen, C., Proc. IEEE MEMS'96, San Diego, CA., 1996, pp. 441-446.
- [3] Virginie Mengeaud, Jacques Josserand, and Hubert H. Girault, Anal. Chem. 2002, Vol.74, pp.4279-4286.

ACTIVE CONTROL OF BOUNDARY LAYER INSTABILITIES ON A FLAT PLATE

Y. Li and M. Gaster

Department of Engineering, Queen Mary, University of London, UK

ABSTRACT: The active control of spatially developing instability waves has been discussed for the case of a zero pressure gradient laminar boundary layer. The effect of three-dimensionality of the disturbance field, which needs to be cancelled, on the performance of the control scheme is considered. An open loop control has been used. This requires a means of both detecting the on-coming waves and of exciting the out-of-phase cancelling waves. The process has been modelled by linear theory and follows the work reported by Gaster^[1]. A similar approach to the earlier work has been used to obtain the test geometry and control strategy for cancelling a fully three-dimensional disturbance field. It turns out to be impractical to fully implement a complete control setup in an experiment as it would involve a vast number of detectors and actuators. A simpler scheme using a local control has therefore been considered. The idea is to use only one detector to control a downstream excitation to provide a local zone of cancellation. This has been modelled and shown to provide some local reduction in the wave amplitudes. A number of local control elements could well be used to represent the behaviour of the full control scheme.

An experiment is being set up to investigate the behavior of a local controller. Results from the experiment will be presented at the conference.

1. INTRODUCTION

Transition from a laminar boundary layer to a turbulent one generally occurs through the selective amplification of naturally excited instability waves. The common approach used to control the behaviour is to introduce disturbance waves of the same amplitude but of opposite sign to the existing ones. First attempts to achieve control in this way have been published by Milling^[2], Liepmann et al.^[3] and Thomas^[4]. This control strategy has been shown to work both in real experiments and in numerical modelling^[5]. However, the large amplitude reductions of around 90% that can be achieved are on only two-dimensional wave systems. Three-dimensional waves are much more difficult to control.

In this paper, the naturally occurring three-dimensional disturbance field is modelled by an array of upstream mounted exciters driven by a random sequence of pulses. Hot wires close to the wall are used as sensors to detect the disturbance velocities and then further downstream, an actuator array is driven by appropriate signals to provide the cancelling field. Section 2 describes the numerical method used to model this scheme. Section 3 describes the control strategy and section 4 the experimental part of the investigation.

2. NUMERICAL METHOD

The approach described here uses two approximations, namely (i) that the mean flow is parallel and (ii) the disturbances are small enough to allow linearisation. The parallel flow assumption should only cause errors if solution are sought at large streamwise distances from the source, while control is only likely to be effective where the disturbances are weak. With the introduction of these two main assumptions, the perturbation equations separate in the space co-ordinates, enabling Fourier transforms to be taken in the streamwise and spanwise directions. This then generates the Orr-Sommerfield and Squire equations defining the transform of the velocity perturbations and their derivatives in the directions of the x , y & z axes. For convenience, these equations have been re-cast into equations for the three orthogonal velocities and the three vorticity components. The solutions then were separated into two parts: (1) the near field solutions which decay downstream and (2) eigen solutions, some of which amplify downstream. This separation is essential for the control problem as it is only possibly to cancel the eigenmodes and the control transfer function can only be generated by the eigenmodes.

The simulations were performed in a rectangular integration domain with the spatial codes developed by Gaster^[6]. The x -(streamwise) and z -(spanwise) directions were discretised at 1mm and in normal direction y , a non-dimensional $\eta = y\sqrt{U_\infty x/2\nu}$ was applied. The perturbation equations were integrated by a standard Runge-Kutta 4th order scheme from the outer boundary layer conditions marching towards the wall boundary. The variables were normalized with the mean velocity $U_\infty = 12$ m/s, the kinematic viscosity $\nu = 1.457 \times 10^{-5}$ m/s² and the boundary layer thickness δ_0 at the location of the source. The Reynolds number R based on the boundary layer thickness was set at 1000.

3. CONTROL MECHNISM

The control scheme to be modelled is shown schematically in Figure 1. It was necessary to introduce controlled disturbances at some upstream station to mimic the receptivity process. By creating the upstream disturbances artificially there was complete control of the wave field. X_e is the distance of the exciters from the leading edge while X_d the distance between the array of exciters and the detectors. X_{da} is the distance between the detector array and the actuator array. Z_d and Z_a are the spanwise spacing of the detectors and the actuators respectively. The detected signals were convolved in both the spanwise direction and time with the control transfer function to provide the driving signals. The cancelling signals at the some downstream target location from actuators were then obtained by convoluting the driving signals with the whole impulse response.

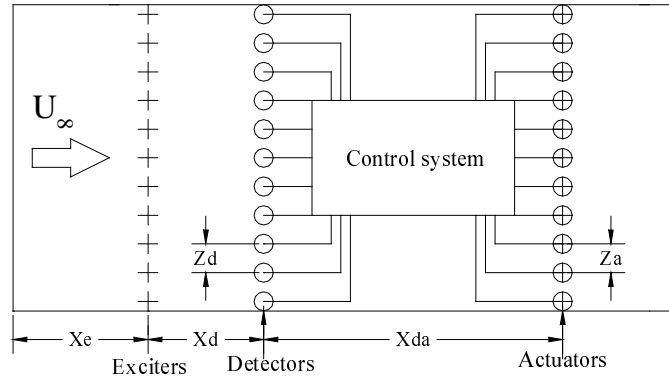


Figure 1. The schematic set up of multiple-sensor-multiple-actuator control system under the surface of the flat plate

The degree of cancellation obtained can be judged by the cross correlation, σ , of the original signal with the cancelling signal at this downstream location. In any practical implementation the correlation function actually is the wavenumber spectral density function of disturbances depending on the spanwise wavenumber and the temporal frequency. Therefore, It is important to consider the influence of the spanwise spacing as well as the sampling rate. The spacing of the transducers should be smaller than half the minimum spanwise wavelength found in the wavenumber spectrum of the original, and the sampling rate should be larger than twice the maximum frequency in the field according to the Nyquist theorem. In other words, the spanwise distribution of the cancelling waves must be smooth enough to account for the three-dimensional characteristic of the disturbances. In addition, spanwise cross-linking of the control system should be made so that each actuator control would use the information from the neighbouring detectors as well as the one directly upstream. However, cross-linking of all the detectors and the actuators would increase the complexity of the implementation. It turns out that the detector upstream is the most important component of the control. After using some appropriate control strategies, it seems that an uncoupled control can be used without any loss in performance, compared with the coupled mode.

The control problem amounts to determining the transfer function of the control system. A 20mm downstream separation ($X_{da} = 20$ mm) was chosen. The transfer function obtained from the unstable

eigenmodes is plotted in figure 2. The portion at negative time must be ignored in the calculations of the signal feeding the actuators because of causality. The transfer function is concentrated on the centre-line, having two peaks that dominate the function at positive time.

The target location of 350mm from the source was chosen to find the effectiveness of the control scheme. Table 1 shows the correlation coefficient at the different spanwise spacing, but with the same sampling time of 1ms. The correlation value 0.969 was maintained up to a spacing of 10 mm. But at larger spacing, a rapid fall off was evident. So a 10mm spanwise transducer spacing was chosen for the simulations. Figure 3 shows the distribution of the spanwise wavenumber spectra. It can be seen that most of the wavenumbers are between the Nyquist wavenumber when the spanwise spacing is 10 mm. As the transfer function was concentrated on the centre-line, the degree of cross-linking will be small and it seemed worth seeing what would result from removing the coupling. The value of 0.967 was obtained, showing that there was almost no loss in removing this constraint. In addition, the uncoupled transfer function can also be reduced to just two delta functions, since the two peaks dominated the function. The reason for doing this is that if digital control were to be used it would be relatively easy to implement this simple control function. A much higher value of 0.987 was obtained with this simplified transfer function if the discrete functions were optimized so that the effect of causality of the transfer function could be offset.

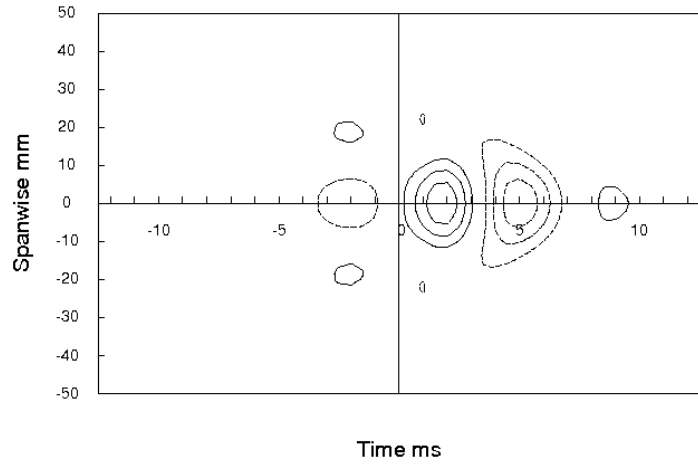


Figure 2. Space-time control transfer function of the three dimensional control at 20mm distance of the detectors array and the actuators array.

Table 1. The correlation coefficients with different spanwise spacing of the transducers

Spacings(mm)	Correlation-Co
Full transfer function	
1	$\sigma=0.970$
5	$\sigma=0.970$
10	$\sigma=0.969$
15	$\sigma=0.943$
20	$\sigma=0.679$

Figure 4 (a) depicts the time traces of the shear stress on the surface at the comparator station 350mm downstream the source line. The disturbances developing with the time were clearly random and could simulate the development process of the natural excited disturbances in the boundary layer. The three-dimensional control could also achieve a considerable reduction in amplitudes, shown in figure 4(b). The residue had the same characteristics as the original disturbances, so multi-streamwise control could probably be used downstream with further reduction in level.

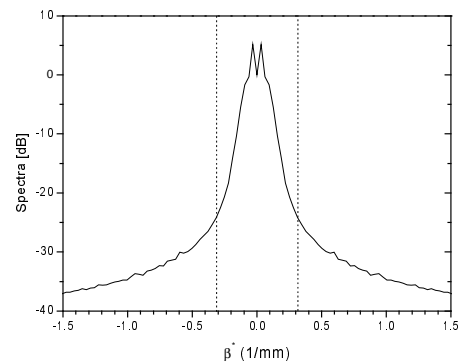


Figure 3. The distribution of the spanwise wavenumber spectra of the final disturbance. The area between two dot lines represents the Nyquist theorem of 10mm spacing. ($\beta^* = \pi / Z$)

Because the experimental work will, at first, be carried out using the idea of a local controller consisting of one detector and associate actuators, it was necessary to model this situation. One sensor & three actuators with same transfer function were considered and figure 5 (a) shows the degree of the cancellation over the region between $x = 120\text{mm}$ to $x = 400\text{mm}$. The maximum cancellation was 40% of the disturbances in the central region. In order to model the electronic noise of the detectors or in the control loop, external noise was added to the driving signal with SNR (signal-noise ratio) at 10:1. The result of cancellation, shown in figure 5 (b), suggests that with selected high sensitivity transducers in the implementation, noise will be not a big problem.

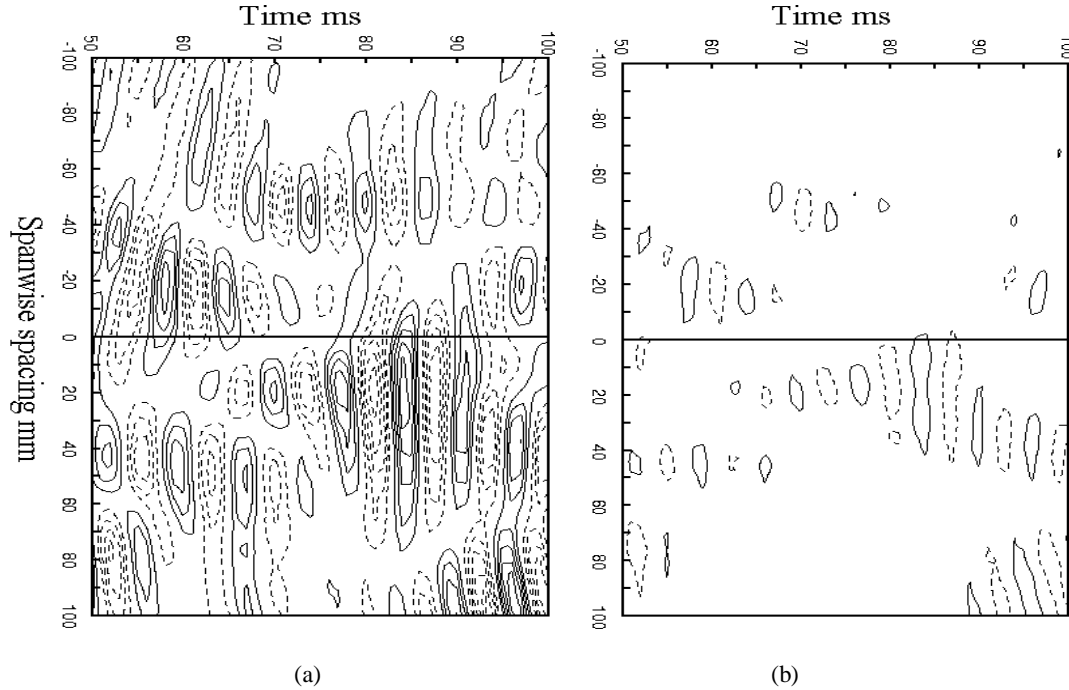


Figure 4. Contour plots of the shear stress at white noise excitation induced instabilities. (a) Original signal and (b) resultant signal after control (uncoupled mode control)

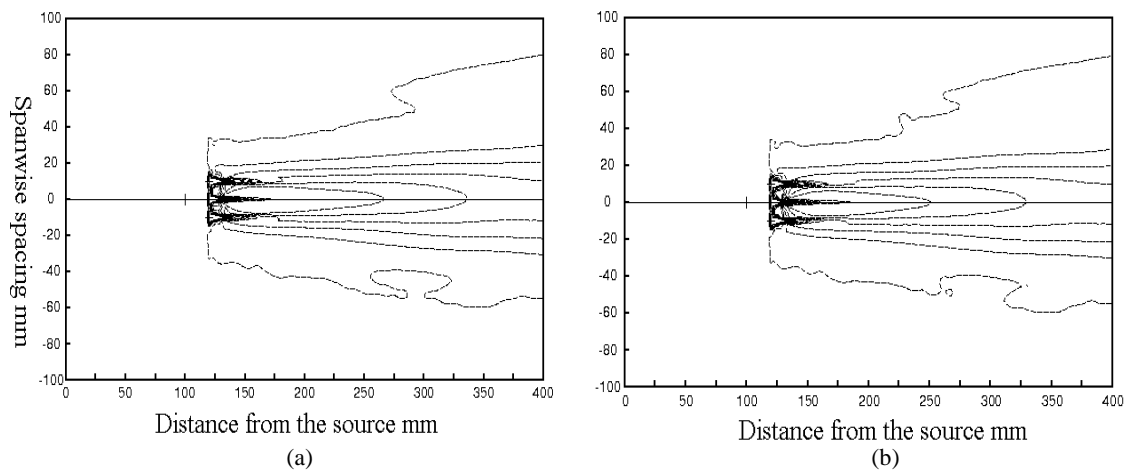


Figure 5. The percentage of amplitude cancellation with 1 detector, 3 actuators. $X_d = 100\text{mm}$ & $X_{da} = 20\text{mm}$. (a) without external noise; (b) with external noise. The line pitch is 8% and the first contour line is zero value.

4. EXPERIMENTAL INVESTIGATION

4.1 Experimental Set-up

The experiments were carrying out on a flat plate, with zero pressure gradient, in a low-turbulence close-return wind tunnel in the Engineering Department of Queen Mary, University of London. Figure 6 is the local controller set-up showing the position of the exciter, detector, actuator and downstream target sensor. An array of exciters (15 Miniature speakers at 10 mm spanwise pitch) was positioned at 410mm from the leading edge of the plate. Each speaker was controlled by one of outputs of a 16-bit module fed with a sequence of random binary numbers. The random binary numbers were stored in the memory of the module so that the output was repeatable. The output of each exciter was a random series of pulsed excitations. The amplitude levels of the excitations were kept within the linear range. The detector was a single hot-wire probe of 5 μ m diameter and 1.0mm sensing length, mounted 0.4 mm off the surface. Only the probe and prong portion of the hot wire were exposed to the flow in order to minimize aerodynamic interference with the probe body. It turned out that the effect of the hot wire on the instability could be tolerated. Three actuators (the same as the exciters) were all connected to the upstream detector on the centre-line via the control system. Each actuator had a reasonable flat frequency response over the range required. The detected signals were multiplied with a transfer function and stored in one D/A converter to produce the driving signal. Velocities from the anemometer and the timing signal of the actuator were simultaneously sampled at a rate of 2 kHz and they were converted to digital format using an A/D converter. The downstream sensor was a traversible hot wire, located downstream of the actuator and the control objective was thus to minimize the streamwise u' fluctuations at the location of this sensor. The convenience of a movable sensor for diagnostics and optimization dictated the choice of u' for most of the experiments, although at the later stage we will also consider other sensors, such as wall-mounted shear or pressure sensor, with corresponding objective of controlling wall shear or pressure fluctuations.

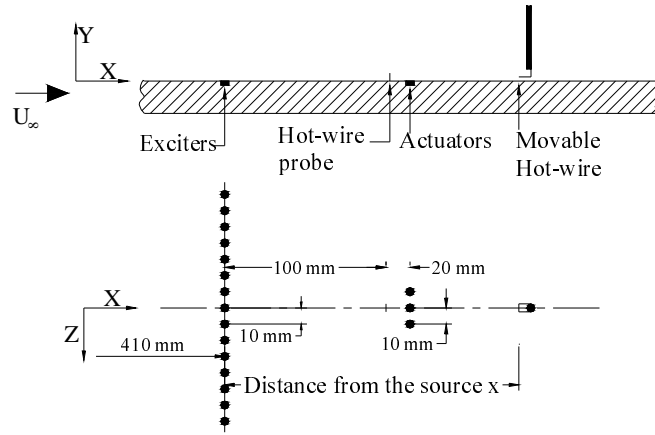


Figure 6. Experimental set-up, schematic of the active control and the spanwise exciter-sensor-actuator arrangement.

4.2 Natural Excited Disturbances

Figure 7 shows a number of time series obtained in the experiment using computer-generated white-noise excitation via the buried loudspeakers. The boundary layer was excited 50 times by the same white-noise sequence and the hot wire was used to measure the response downstream. The response was then ensemble averaged to generate a spatio-temporal evolution of the disturbance flow. Figure 7 (a) shows two time series at $x = 650$ mm and $\eta = 0.5$. The upper trace is the ensemble average while the lower trace provides a measure of the standard deviation. The averaged signal shows amplitude-modulated oscillations that correspond to T-S disturbances in the flow. The relatively low value of the standard deviation indicated that the response of the boundary layer to the white-noise excitation was essentially

deterministic and repeatable. Figure 7 (b) shows similar traces from non-dimensional wall positions given by $\eta = 1.2$.

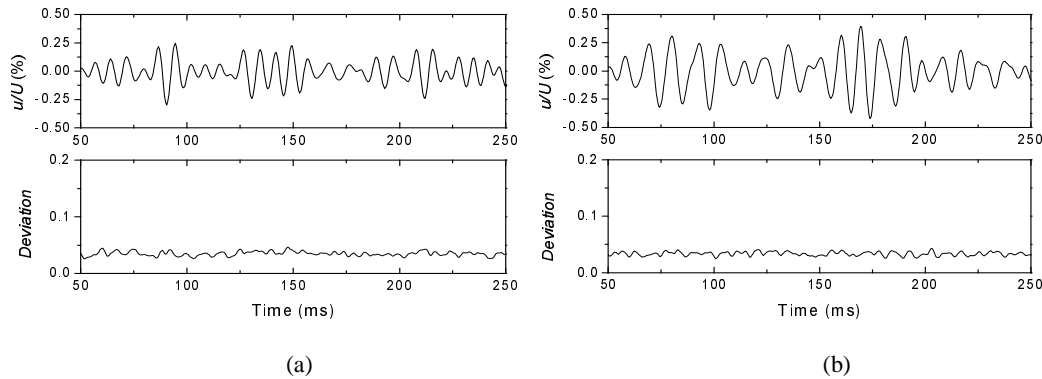


Figure 7. Ensemble-averaged velocity time record and associated standard deviation measured at $x = 650\text{mm}$ and non-dimensional normal locations (a) $\eta = 0.5$ and (b) $\eta = 1.2$.

4.3 Control Development

Control will initially be implemented off-line. The noise excitation sequence will be run and the hot-wire detector signal recorded. The hot-wire signal will then be processed off-line to create an appropriate control signal. The experiment will be re-run using the control to drive the exciters. The success of the control will be assessed by the measurement of the fluctuating velocities at the target station. The target hot-wire will be traversed over the zone downstream and the result compared with the prediction. With the off-line control, more complex transfer functions can be explored. At some later stage a real-time control will be implemented in hardware with the chosen transfer function.

5. CONCLUSIONS AND EXPECTATIONS

A practical control scheme has been developed that can reduce the amplitudes of a three-dimensional wave field significantly. A simplified scheme for a local controller using one detector has also been discussed and shown to reduce the signals in a small domain. An array of these devices can produce a very significant degree of control, but the initial experiment will only explore one local controller. If the modelling is shown to be reflected by the measurement, it will then be used to consider the behaviour of an arrangement of isolated controllers distributed over the plate.

At some future time it is hoped to use a small number of local controllers with hardware in real time.

6. ACKNOWLEDGEMENTS

The study was supported by the British Aerospace.

REFERENCES

- [1] Gaster M. Active control of boundary layer instabilities using MEMs. *Current science*, 2000, **79**, No. 6, 774-780.
- [2] Milling RW. Tollmien-schlichting waves cancellation. *Physics of Fluids*, 1981, **24**, 979-981.
- [3] Liepmann HW, Brown GL, Nosenchuck DM. Control of laminar-instability waves using a new technique. *J. Fluid Mech.* 1982, **118**, 187-200.
- [4] Thomas ASW. The control of boundary layer transition using a wave-superposition principle. *J. Fluid Mech.* 1983, **137**, 233-250.
- [5] Thomas ASW. Active control of boundary layer transition, *Viscous Drag Reduction in Boundary layers*, Progress in Astronautics and Aeronautics, (Eds. Bushwell, DM, Hefner JN.), 1989, **123**, 179-199.
- [6] Gaster M and Shaikh, FN, Report, Department of Engineering. Queen Mary College. 1996.

LAND PREPARATION WATER MANAGEMENT BY CANAL SIMULATION IN A PADDY ESTATE IN MALAYSIA

M.M.M. Najim

Department of Agricultural Engineering, Faculty of Agriculture, University of Peradeniya, Peradeniya, Sri Lanka.

T.S. Lee

Faculty of Engineering, Universiti Putra Malaysia, 43400 Serdang, Selangor, Malaysia.

M. Aminul Haque

Water Resources Planning Organization, Ministry of Water Resources, Dhaka, Bangladesh.

M.I.M. Mowjood

Department of Agricultural Engineering, Faculty of Agriculture, University of Peradeniya, Peradeniya, Sri Lanka.

ABSTRACT: A canal simulation study was conducted in an intensively cultivated paddy estate in Malaysia. CanalMan software was applied to main and selected secondary canals that have difficulty in land preparation supply within the scheduled time periods. The study revealed that the CanalMan is capable of simulating different scenarios possible in the project area. Canal simulations also revealed that the land preparation supply management could be completed in three days, which is two days less than the current practice, when the canals are supplied with design discharges. Canal simulations combined with a water balance study revealed a minimum of 20 mm of effective rainfall is needed to complete land preparation within the desired period. When the water levels along main canal drops, the required rainfall is much higher. This forces the management to start supply by pumping or shift land preparation water management in critical blocks to the drainage period soon after seeding in other blocks.

1. INTRODUCTION

Proper operation of the canal system in a large irrigation system is important in order to supply the exact amount to each plot at right time. The operation and management policy of the irrigation system is vital to satisfy the supply required by the crop in each plot. The water levels along main canals need to be maintained according to the system guidelines in order to supply the required flows to each location within the irrigation system. However, the operation of the irrigation system is not a simple task as needs and supplies or flows vary due to temporal and spatial variability. Therefore, it is essential to have an appropriate management policy with feasible options for widely variable ranges of conditions possible in an irrigation scheme.

Widely varying flow conditions along canals are difficult to be judged. The judgment of such visibilities is possible through mathematical modeling of the system. Computer models based on mathematical relationships, which govern such variations and other conditions along canal systems are good tools to help managers to achieve management goals.

The emergence of estate paddy cultivations in Malaysia paved the way for intensive paddy cultivation. These paddy estates try to utilize the whole cropping area with a maximum cropping intensity. Therefore, a close coordination between canal system management and on farm water management is a precondition for efficient water management in an irrigation system with intensive mechanized cultivation. But, most of studies on canal flow modeling concentrated hydraulic modeling of canal systems mainly emphasizing on flow behaviors rather than an aid to decision making. Few models have been developed in order to address both of these issues.

The major reason for poor irrigation performance in large irrigation schemes in Asia is due to inadequate attention paid to main system management^[1,2]. Many researchers tried to answer the canal water scheduling problems using linear programming. A linearized finite difference model of open channel flow was utilized to convert a canal operation problem to an optimal control problem^[3]. This method is appropriate to derive control algorithms to run irrigation canals on either demand or limited-rate demand delivery schedule. A linear programming technique was used to devise an improved method of water allocation to different canals in a canal system^[4]. A simulation model based on water balance and soil moisture simulations was developed to estimate water deliveries at the tertiary and secondary canal levels^[5]. Most of such models do not allow interactive irrigation system management for unsteady flows along canal networks. The public domain hydraulic simulation model for unsteady flow in branching canal networks; CanalMan^[6] is capable to address these issues.

CanalMan model, which supports unsteady flow regimes was applied in the watershed of Rio Itata, Chile to study irrigation efficiency^[7]. The results of the studies offer an evaluation of the actual situation of an irrigation system, and tools for the improvement of the efficiency on the different levels.

CanalMan, was also used for the Pehur High-Level, tail of Machai Branch and Maira Branch canal network because this software package contains an algorithm for automatic gates. The design was subjected to a series of severe operating conditions, which showed that; in general, the system could be expected to perform well^[8].

Consultancy and engineering firms also used the CanalMan model in nonsteady state hydraulic modeling and verification of operational designs. Davey-Cairo Engineering, Inc. (DCE) used CanalMan for non-steady state hydraulic modeling and verification of operational design criteria in rehabilitation and lining projects, Gila River Indian Community, Sacaton, Arizona^[9].

The land preparation could smoothly be completed if the canal system is capable of delivering design discharges together with supplemental rainfall. Both canal supply and rainfall play a major role in this aspect. Therefore, a study was done with the objective to simulate the canal flows in order to assist the management to make decisions that enables to complete land preparation water management within the required time in the selected paddy estate.

2. METHODOLOGY

2.1 Study Area

Seberang Perak paddy estate (4° 7' N and 101° 4' E) located in the west coast of Peninsular Malaysia is the largest and oldest paddy estate in the country with 4353ha. This paddy estate is managed by Federal Land Consolidation and Rehabilitation Authority (FELCRA) a government owned company. The paddy estate is divided into three sub-divisions and under three managers responsible for day-to-day management activities. The estate management increased the cropping intensity from 200% to 250%. Adherence to 250% cropping intensity is only possible if the management could strictly maintain the cropping schedules and field practices within prescribed time schedules. Major field operation needs to be completed within time is the land preparation. The delay in land preparation period postpones all other field activities that will hinder the achievement of the cropping intensity desired. Three most critical secondary blocks in terms of difficulty in supplying land preparation was selected. The secondary canals selected are L1B1, L5 and R7 (Figure 1)

2.2 Data Collection

The data needed for canal simulation was collected from many sources related to water management in the project area. The weather data were collected from the Malaysian Meteorological Services for the

stations Sitiawan and Ulu Dedap. The canal flow levels at different gauging points were recorded from the Department of Irrigation and Drainage (DID), Ulu Dedap. The entire canal related information such as dimension of canals, lengths, full supply levels, and information on structures along the canal systems were also collected either from FELCRA Seberang Perak, DID and Ulu Dedap.

Information on crop schedules practiced in the project was collected from the FELCRA Seberang Perak management. The discussions with the management of the project revealed that the water level reduction due to low rainfall and drop in river levels would cause serious problems in water supply during land preparation water management operations.

2.2 Flow Modeling

Canal Management Software (CanalMan)^[6], developed for performing hydraulic simulations of unsteady flow in branching canal networks, was selected for this study. This model was selected because of many reasons. The model incorporates turnout structures and in-line structures. It can simulate canal operations in a manual mode. CanalMan implicitly solves an integrated form of the Saint-Venant equations of continuity and motion for one-dimensional unsteady open-channel flow. Simulations can be started by filling an empty canal system, continuing a previous simulation or from a specified steady or unsteady flow condition.

Based on the canal flow simulations, time to complete an irrigation operation with a known or a simulated flow, the land area to be cultivated if there is a shortage of supply and filling time of the canals are decided. In this process, the water availability from the river diversion together with the rainfall is considered. The simulations were done to find the canal filling time, and to analyze the water supply during land preparation supply period with many possible water level scenarios.

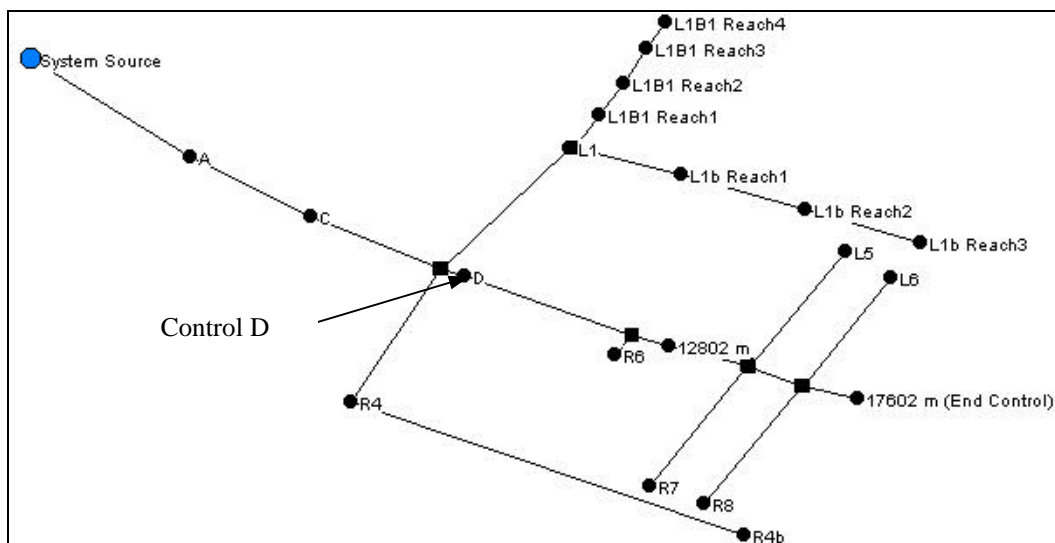


Figure 1 Simulated canal system layout from Seberang Perak paddy estate

The collected data was used to determine data input to the model in order to simulate flows along main, sub-mains and secondary canals. The canals were divided into reaches according to the canal structural and dimensional differences. Table 1 shows the reach information used for secondary canal L1B1. With all information on canal system, the simulations were done to determine the validity of the simulation results. In this process, the available data from the field observations at different control structures (Control D, at Gate R6, at Gates R7/L5 and at Gates R8/L6 in Figure 1) were used. Several canal simulations were done to check the validity of the canal simulations with the measured water depths

at control D, gate R6, gates R7/L5 and gates R8/L6. The maintained level along the right branch canal (RBC) canal is measured mainly at control D. The department of irrigation and drainage maintains water depth at control D at 2.7 m or more in order to make sure the supply is enough to meet the design discharges in all the secondary and tertiary canals in the project area.

Table 1. Reach information for secondary canal L1B1

Reach	Length (m)	Section*	Bed Slope	Type
Reach 1	343.0	1.067/0.914/0.125:1	0.00025	Concrete
Reach 2	1502.0	1.067/0.914/0.125:1	0.00020	Concrete
Reach 3	877.0	0.914/0.762/0.125:1	0.00018	Concrete
Reach 4	877.0	0.610/0.610/0.125:1	0.00017	Concrete

* Bottom width/Depth/Side Slope (height: width)

Water level reduction along main canal would cause difficulty in irrigation water supply. As water level reduction and irrigation supply information was not kept as records, the levels along the main canals were simulated with a percentage drop from the optimum level needed to supply the project without any difficulty. Simulations were carried out to find the land preparation supply durations. Land preparation should be completed within 16 days in L1B1 and R5 and within 14 days in R7 secondary blocks. When the simulation is not capable of supplying the required depths as needed during the specified period, the minimum effective rainfall needed to complete land preparation within the prescribed time period is calculated using a water balance approach. Other alternative management practices are also proposed when it is not possible to complete land preparation within desired time period.

3. RESULTS AND DISCUSSIONS

Four simulations were done with design flow in RBC main canal because of data availability. The first simulation was done with specified flows from the gates R4 and L1. The specified flows are the design discharges maintained in L1 and R4 main canals. The second simulation was done giving R4 the specified flow with the L1 gate control where the gate diverts the design discharge to the L1 main canal. The third simulation was done with all the gates adjusted to supply the design discharge. The fourth simulation was done with the gate L1 with specified flow while the R4 is fully opened. All these four simulations done were maintaining the design discharges in the L1 and R4 main canals while maintaining the full supply level (FSL) in the RBC main canal. The simulation results are shown in Figure 2. The simulation results show a deviation of less than $\pm 5\%$ at all the locations. The highest average deviation shown is at gate R7/L5 (4.4%) while the lowest average deviation is at gate R6 (-0.6%).

Land preparation water supply to the fields has to be started soon after the canal system is filled. The time required filling the main canal; its sub-mains and some secondary canals are considerable. Just before the supply to field lots, all the canals need to be filled to the full supply level. The main canal and sub-mains are filled in a step. After the main canal and its branches are filled, the second step is to fill the secondary canals. When all the secondary canals are filled, the tertiary canals are filled according to the land preparation supply schedules. Simulations done for canal filling shows that the first step of canal filling needs 36 hours if the canal system is supplied with the design discharge along the main canal. When the flow level in main canal reduces, the time required increases. It needs 42 hours to fill the main canal system if the flow level along main canals is in between 10.1 to 9.5 m³/s.

Out of three secondary canals considered in this study, the L5 secondary needs the longest duration to fill. If the main canal is supplied with the design discharge, it needs 25 hours for secondary L5 to be filled. This will increase to 31 hrs when the flow level along main canal is in between 10.1 to 9.5 m³/s. According to the canal filling time, it needs a minimum of 2.5 days for the canals to be filled in case of the design discharge is supplied along main canals. This could increase to 3 days if the flow level decreases in between 10.1 to 9.5 m³/s. The management takes 5 days to complete the canal filling process. Considering all the management requirements to canal and flow management in the study area,

it needs 3 days to 5 days to fill the canal system for the both cases described above respectively. Therefore, there is a possibility to save two days during canal filling process if the canals are supplied with design discharges.

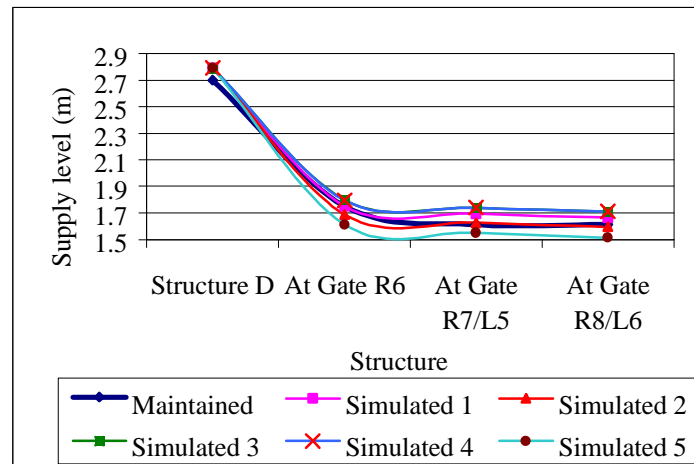


Figure 2. Canal simulation results at different gauging stations

The canal simulations with the optimum water levels in main canals and the possible scenarios along main canals show the flow variations along the secondary canals. The optimum water levels in the RBC main canal could supply the design discharges in all the branches of main canal, secondary and tertiary canals. When the flow level in the main canal RBC is reduced, it is difficult to supply the design discharges in most of the secondary canals. The water level reductions in the RBC main canal as tested through simulations are given in Table 2. When the water level at control D is reduced beyond 2.163 m level, then most of the secondary and tertiary canals could not be supplied with the design discharges, which will ensure a smooth supply for land preparation. Land preparation needs to be coincided with rainfall. It is difficult to supply the land preparation requirement when the flow levels are reduced in secondary and tertiary canals. Therefore, the management has to depend on rainfall in order to complete land preparation. If the rainfall received is not sufficient, pumping or postponing land preparation in some plots become inevitable.

Table 2. Water levels at control D and minimum possible supply to secondary canals

Depth at control D (m)	Supply to secondary canal (m ³ /s)		
	L1B1	L5	R7
Depth 2.163	0.546*	0.748*	0.885*
2.119 Depth < 2.163	0.546*	0.748	0.863
2.069 Depth < 2.119	0.540	0.689	0.795
2.022 Depth < 2.069	0.525	0.656	0.756
1.969 Depth < 2.022	0.509	0.610	0.703

* Design discharge

Table 3 shows the effective rainfall needed in order to complete the land preparation within the desired time period. According to the finding, the land preparation needs to coincide with rainfall. Minimum of 20 mm of effective rainfall is needed to complete land preparation supply within the time schedule. If the rainfall is less or the canal flow level at control D drops or different combinations of these scenarios will force the management to practice other management alternatives in order to complete land preparation within the scheduled time. These management alternatives could be either pumping or shifting land preparation to the period of field drainage soon after seeding in other secondary blocks.

Pumping can supply the shortage of land preparation required in L1B1 and R7 canals. Only the L5 block land preparation need to be postponed if the flow level at control D decreases less than 2.069 m.

Table 3. Water levels at control D and effective rainfall needed to complete land preparation within desired time

Depth at control D (m)	Effective rainfall needed to complete land preparation within desired time (mm)		
	L1B1	L5	R7
Depth 2.163	11	20	0
2.119 Depth < 2.163	11	20	7
2.069 Depth < 2.119	13	22	12
2.022 Depth < 2.069	20	35	16
1.969 Depth < 2.022	26	66	23

4. CONCLUSION

Canal simulation for land preparation water management in a paddy estate was done using CanalMan software. The simulations were initially done along the main canal and found that the deviations are less than $\pm 5\%$. After calibration, the simulations were done with three secondary canals, which supply the largest secondary block in each sub-estate. The canal simulations revealed that 3 – 5 days are required to fill the whole canal system. Filling the canal system needs only three days when the canals supply with design discharges. Canal simulations combined with water balance approach determined the duration needed to complete land preparation supply in each selected secondary block. Alternative management approaches are proposed when the land preparation could not be completed within the scheduled time. This study revealed that canal simulations by CanalMan could be used as an effective way to make decisions on canal management during land preparation water management in an intensive rice cultivation system.

REFERENCES

- [1] Bhuiyan, S.I. 1981. Experience in field research in irrigation system management in the Philippines– more methodological issues. Paper presented at the international seminar on Field Research Methodologies for improved irrigation system management, Coimbatore, Tamilnadu Agricultural University College of Agricultural Engineering, Sept 15-18.
- [2] Bottrall, A. 1981. Action research towards improved water distribution. Paper presented at the international seminar on Field Research Methodologies for improved irrigation system management, Coimbatore, Tamilnadu Agricultural University College of Agricultural Engineering, Sept 15-18.
- [3] Reddy, M. Dia, A. and Oussou, A. 1992. Design of control algorithm for operation of irrigation canals. Journal of Irrigation and Drainage Engineering, 118(6): 852 – 867.
- [4] Shyam, R. Chauhan, H.S. and Sharma, J.S. 1994. Optimal operation scheduling model for a canal system. Agricultural Water Management, 26: 213 – 225.
- [5] Kemachandra, R.A.D. and Murty, V.V.N. 1992. Modeling irrigation deliveries for tertiary units in large irrigation systems, Agricultural Water Management, 21: 197 – 214.
- [6] Merkle, G.P. 1997. CanalMan: A Hydraulic Simulation Model For Unsteady Flow In Branching Canal Networks, Version 5.30, Department of Biological and Irrigation Engineering, Utah State University, Logan, Utah 84322-4105.
- [7] Billib, M. and Holzapfel, E. 2002. Study of the Irrigation Efficiency in the Watershed of Rio Itata / Chile, <http://www.iww.uni-hannover.de/forschung/abgeschlossene%20projekte.htm>
- [8] Skogerboe, G.V. Habib, V. Pongput, K. Vehmeyer, P.W. and Khan, A.H. 1998. Canal modernization in the Indus Basin irrigation system, In Modernization of irrigation system operations: proceedings of the 5th ITIS network international meeting, Aurangabad., FAO, Rome.
- [9] Cairo, G.J. Davey, J.V. 2002. Statement of qualifications, www.daveycairo.com/index_files/dce_irrigation_district_sq.pdf 2121 West University Drive, Tempe, Arizona.

EFFECT ON WAVE RUN-UP OF SHALLOW WATER CONDITIONS IN FRONT OF A SMOOTH SLOPING STRUCTURE

D.A. Peiris and J.J. Wijetunge

Department of Civil Engineering, University of Peradeniya, Peradeniya, Sri Lanka

ABSTRACT: This paper describes an experimental study carried out in a laboratory wave flume to examine the effect on the wave run-up of shallow water conditions in front of a smooth sloping structure. The run-up measurements were carried out over practically important ranges of the wave steepness, the relative water depth, the structure slope and the foreshore slope. The results indicate an increase in the wave run-up at shallow depths compared to deep water conditions. This increase is up to about 20% for plunging breakers and is as much as 65% for surging breakers. The measurements also seem to suggest a slight increase in the wave run-up with increasing foreshore slope angle.

1. INTRODUCTION

Wave run-up is the upper limit of wave uprush above the still sea level. The run-up height is required to determine the crest level of structures that are designed for no or only marginal overtopping such as revetments, dikes and breakwaters for small craft fishery harbours. The wave run-up on a coastal structure depends on the incident wave properties as well as on the structure characteristics such as the slope angle, the surface roughness, the water depth at the toe of the structure and the slope of the foreshore.

Moreover, most coastal structures are located in relatively shallow water, and consequently, such structures are likely to be exposed to depth limited waves, particularly during design storms. Accordingly, we would expect the wave conditions in front of shallow water structures to depend, among other factors, upon the wave transformation on the foreshore as well as on the structure itself. The wave field in front of coastal structures is probably further affected by the likely interaction of the hydraulic processes at the structure with the wave transformation on the foreshore. However, unfortunately, most laboratory experiments on wave run-up on coastal structures (e.g., [1-4], among several others) have been conducted in relatively deep water, and consequently, little is known about the effect of wave transformation including possible breaking of waves due to the foreshore on the subsequent run-up over shallow water coastal structures [5]. The limited number of experimental studies of wave run-up under shallow water conditions include those reported in [6] and [7] with irregular waves breaking on foreshores inclined at 1:30 and 1:100, respectively. They found that breaking of irregular waves on a shallow foreshore results in lower maximum run-up heights, although higher mean run-up heights could sometimes occur. However, an explanation as to what caused the higher mean run-up heights in some of the tests is not provided. Moreover, both these studies examined only the influence of the foreshore induced breaking of higher wave heights in an irregular wave train on the subsequent wave run-up, thus making specific observations and conclusions on the effect of water depth not possible.

Accordingly, there is a need to shed further light on the way in which depth-limited wave conditions influence the wave run-up over shallow water coastal structures. Therefore, the primary objectives of the present paper are to examine the effects of the relative water depth as well as the slope of the foreshore on the wave run-up on sloping structures over a range of the relevant dimensionless parameters.

2. EXPERIMENTAL PROCEDURE

The experiments were carried out in a wave flume in The Fluids Laboratory of University of Peradeniya. This flume consists of a regular wave generator and a 12.75 m long, 0.52 m wide and 0.70 m deep Perspex walled channel (see Fig. 1). A wooden model of a sloping structure together with a 2 m

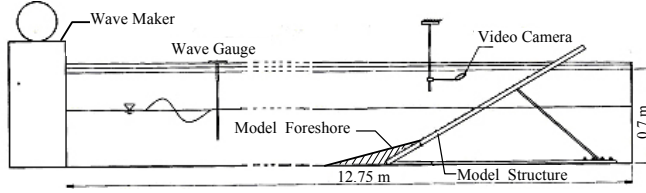


Fig. 1: Experimental set-up.

long foreshore was placed at the far end of the channel. The inclination of both the structure and the foreshore could be changed according to the requirement. A Perspex sheet was also placed on the face of the model structure to obtain a smooth surface.

The wave parameters were recorded using an Armfield H40, resistant type, twin-wire probe whilst a video camera was employed to obtain the wave run-up on the slope. The video clips obtained in this way were played on a Personal Computer (PC) at 25 frames per second to obtain run-up levels, averaged at 5 cm intervals across the slope. Moreover, the run-up measurement for a given wave setting was repeated twice and the average was taken.

About 400 tests were performed in this way over a range of water depths at the toe of the structure by changing the water level in the channel for several values of the wave steepness, the structure slope and the foreshore slope that are practically important.

3. DIMENSIONAL ANALYSIS

It will help in the interpretation of the experimental results if we identify the relevant dimensionless groups. The wave run-up (R) over a smooth, impermeable slope under the present experimental conditions depends on d_s , the depth of water at the toe of the structure; g , the acceleration due to gravity; H_0 , the deep water wave height; T , the wave period; α , the slope angle of the structure; and β , the slope angle of the foreshore.

Thus, the non-dimensional run-up (R/H_0) may be expressed as a function of the following dimensionless groups:

$$\frac{R}{H_0} = \phi \left(\frac{gT^2}{H_0}, \frac{d_s}{H_0}, \tan \alpha, \tan \beta \right) \quad (1)$$

We now define a breaker parameter for wave action slopes [8]: $\zeta_0 = \frac{\tan \alpha}{\sqrt{s_0}}$, where, $s_0 = \frac{2\pi H_0}{gT^2}$.

Following many previous investigations of wave run-up on slopes (e.g., [1-8]), the present study employs the breaker parameter ζ_0 to represent the dual dependence of the non-dimensional wave run-up on gT^2/H_0 and $\tan \alpha$ for waves that break on the structure.

4. TEST CONDITIONS

The test ranges of the main parameters relevant to the present study are summarized in Table 1.

Table 1: Test Conditions.

Parameter	H_0 (cm)	T (s)	α (deg.)	β (deg.)	ζ_0	d_s/H_0
Study Range	4.2 – 14.5	0.7 – 1.1	24.8 – 32.7	2.6 – 8.1	1.5 – 3.6	0 – 6

The run-up measurements are available for $\alpha = 24.8, 28.7$ and 32.7 deg. to the horizontal and for $\beta = 2.6, 3.7, 4.8, 5.9, 6.8$ and 8.1 deg. to the horizontal, over a range of d_s/H_0 .

5. RESULTS AND DISCUSSION

Fig. 2 shows two examples of the way in which the non-dimensional run-up (R/H_0) varies with the non-dimensional water depth at the toe of the structure (d_s/H_0). Note that the values of the wave steepness (gT^2/H_0) for the measurements in both figures are confined to a narrow range of 178 – 199 whilst the slope angle of the foreshore is kept at 3.7 deg. to the horizontal. However, the slope angle of the structure is 24.8 deg. to the horizontal for the measurements in Fig. 2(a) and is 32.7 deg. to the horizontal for those in Fig. 2(b). Accordingly, the breaker parameter (ζ_0) corresponding to the waves that break on the structure is 2.5 for the run-up measurements in Fig. 2(a), indicating that the type of wave breaking on the structure is plunging. On the other hand, the value of ζ_0 applicable to the run-up measurements in Fig. 2(b) is 3.5, so the type of wave breaking is surging.

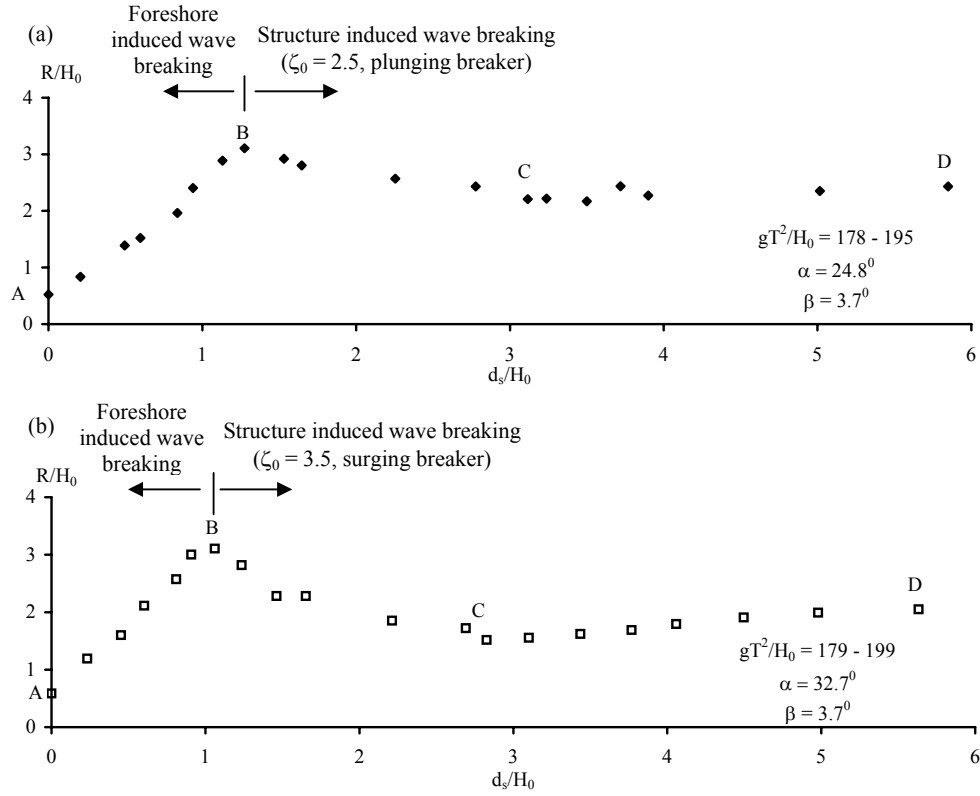


Fig. 2: Variation of R/H_0 with d_s/H_0 : (a) $\zeta_0 = 2.5$, (b) $\zeta_0 = 3.5$.

We see in Fig. 2 that R/H_0 initially increases with d_s/H_0 and reaches a peak value (segment AB of the curves), then declines with further increase of d_s/H_0 (segment BC) before reaching a nearly constant value for relative depths larger than about 2.5 (segment CD). Accordingly, we see that, although R/H_0 is affected little or perhaps not at all by the relative water depth at values of d_s/H_0 larger than about 2.5, the water depth does have a significant influence on R/H_0 at low values of d_s/H_0 , i.e., segments AB and BC.

As would be expected, the run-up records shown in segment AB were due to waves that were breaking on the foreshore. Consequently, it is not surprising that R/H_0 in segment AB reduces gradually with decreasing d_s/H_0 because waves break progressively away from the toe of the structure as d_s/H_0 is reduced. On the other hand, wave breaking was primarily due to the structure at values of d_s/H_0 in

segments BC and CD of the curves. Now, an interesting question is what causes significantly higher values of R/H_0 at low values of d_s/H_0 around the peak at B compared to higher values of d_s/H_0 , say at C. So, to find a clue to the processes that are responsible for this behaviour, let us have a closer look at the event immediately preceding the run-up, i.e., wave breaking. Accordingly, video records of the wave breaking and the subsequent run-up corresponding to data points B and C were made through the side panels of the wave channel, and played in slow motion simultaneously at 25 frames/s, to enable a direct comparison of the two cases.

The examination of the video records of plunging breakers revealed that the wave height in front of the structure just before breaking was about 20 – 30% higher at B than at C. This, however, is not entirely surprising as we expect the waves to shoal over shallow foreshores thus increasing the wave steepness, and then the higher breaker heights to give higher run-up levels. Further, as mentioned earlier, wave transformation on the foreshore could also be influenced by the hydraulic responses at the structure. More importantly, video records at B and C for surging breakers revealed that the increase in the wave height just before breaking at B was quite substantial, over 100%, compared to that at C. The run-up measurements at other values of the wave steepness, the structure slope and the foreshore slope covered in the present study too showed a qualitatively similar behaviour.

We have already seen from the curves of wave run-up variation with d_s/H_0 that the run-up is higher in segment BC and in part of AB than the mean run-up for segment CD. It is interesting to examine the range of d_s/H_0 values in which R/H_0 is higher than the mean R/H_0 for segment CD. This is shown in Fig. 3 for all measurements over a range of values of ζ_0 and for six different values of β . The inset in Fig. 3 indicates the region where shallow water effects could be important in the design of coastal structures. The inset also identifies the lower bound (L) and the upper bound (U) of d_s/H_0 within which shallow water depths could cause an increase in the run-up, together with the d_s/H_0 value corresponding to the peak R/H_0 .

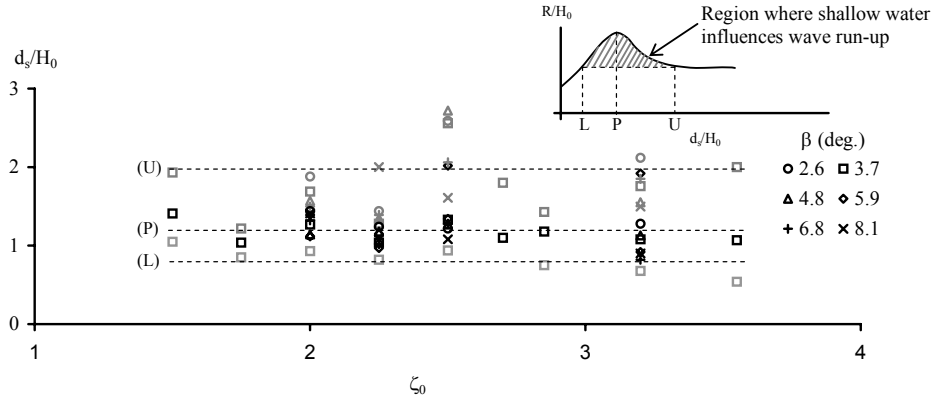


Fig. 3: Range of d_s/H_0 in which shallow water causes an increase in R/H_0 .

In Fig. 3, the symbols in black show the values of d_s/H_0 at which the peak values of R/H_0 occur whilst the symbols in grey indicate the lower bound and the upper bound of the region where shallow water effects are important. The curves drawn through the data points for the peak, the lower bound and the upper bound of R/H_0 are approximate lines to merely indicate the corresponding mean values of d_s/H_0 , despite the scatter of data. Accordingly, we see that the peak value of R/H_0 mostly occurs at $d_s/H_0 \approx 1.2$ whilst, on the whole, it appears that shallow water causes an increase in the run-up for values of d_s/H_0 falling between 0.8 and 2.

Fig. 4 shows the variation with ζ_0 for a range of foreshore angles (β) of the peak value of R/H_0 (peak of run-up with d_s/H_0 , at B) and the mean R/H_0 value of the segment CD. Apparently, the mean R/H_0 for segment CD (ie, for $d_s/H_0 > 2.5$) follow the usual pattern of most previous measurements in relatively deep water conditions, with an initial increase of R/H_0 with ζ_0 , reaching a peak at about $\zeta_0 = 2.5$ before beginning to decline with further increase of ζ_0 . We also see in this figure, that R/H_0 appears to be a little sensitive to the slope angle of the foreshore (β), which topic we will be discussing further later. The peak value of R/H_0 (with d_s/H_0) that occurs at $d_s/H_0 \approx 1.2$ too show a qualitatively similar variation to that of the mean R/H_0 . However, the maximum value of the peak R/H_0 variation is shifted to around $\zeta_0 = 3$. We also see that the peak R/H_0 is considerably larger than the mean R/H_0 for $\zeta_0 > 2.5$, i.e., at values of ζ_0 for which wave breaking type is surging.

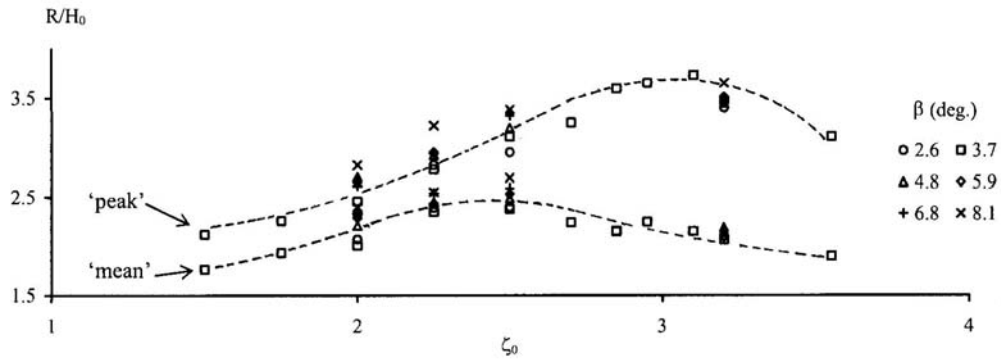


Fig. 4: Variation with ζ_0 of the “peak” and “mean” values of R/H_0 with d_s/H_0 .

We now examine in Fig. 5 the maximum percentage increase of R/H_0 at low values of d_s/H_0 with respect to the mean value. Also indicated on this figure are the types of wave breaking obtained from the examination of video records as well as from visual observations of wave breaking on the structure. Accordingly, $\zeta_0 < 2.5$ belongs approximately to the plunging breaker; $2.5 < \zeta_0 < 3$, to the collapsing breaker; and $\zeta_0 > 3$, to the surging breaker. However, it must be added that the change from one type of breaker to another does not happen suddenly, but over a transition region.

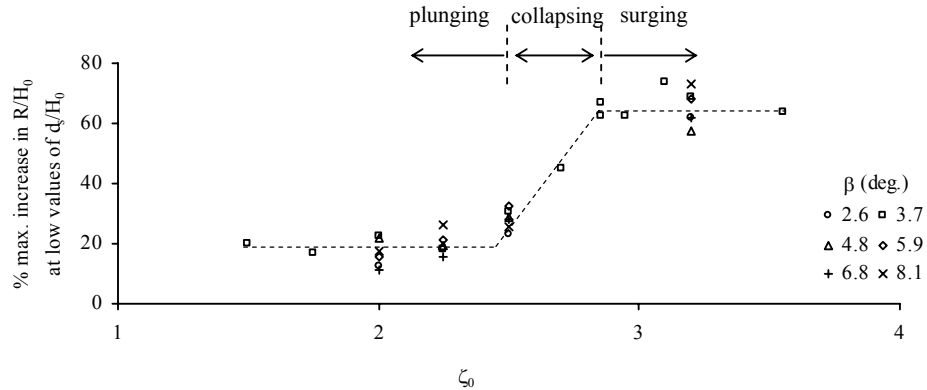


Fig. 5: Variation with ζ_0 of the maximum increase in R/H_0 at low values of d_s/H_0 .

The broken line shown in Fig. 5 is drawn to merely guide the eye through the data points. We see that the increase in R/H_0 for plunging breakers at low values of ζ_0 is about 20%. However, this figure increases sharply through the collapsing breaker region up to as much as about 65% for surging breakers.

We have already seen in Fig. 4 that R/H_0 appears to be slightly sensitive to the foreshore slope angle. So, we now use the present measurements to investigate the influence of the foreshore slope on the wave run-up over a range of relative water depths. Accordingly, Fig. 6 shows two examples of the way in which R/H_0 varies with d_s/H_0 at several values of the foreshore slope angle and for two values of the breaker parameter, one in the plunging breaker region and the other in the surging breaker region. It must also be added that detailed run-up measurements were not obtained for values of d_s/H_0 in the foreshore induced breaking region.

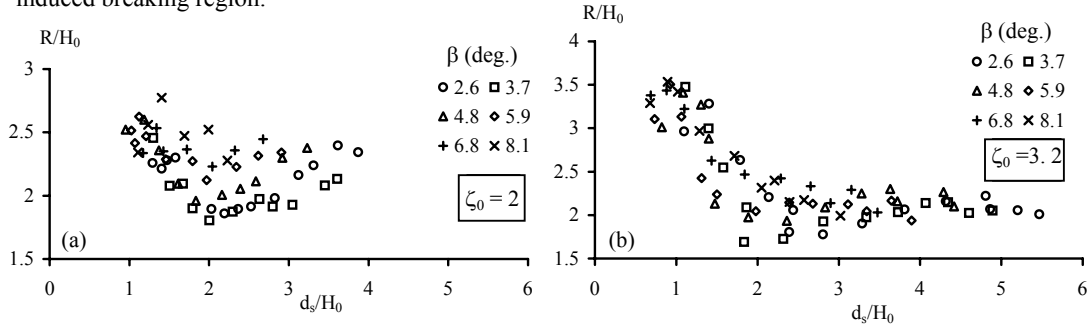


Fig. 6: Variation of R/H_0 with d_s/H_0 at several values of β : (a) $\zeta_0 = 2$, (b) $\zeta_0 = 3.2$.

The influence of β on R/H_0 is not at once discernible from Fig. 6. Therefore, smooth curves were drawn by eye through the data points for each value of β to obtain R/H_0 with β at several values of d_s/H_0 (see Fig. 7).

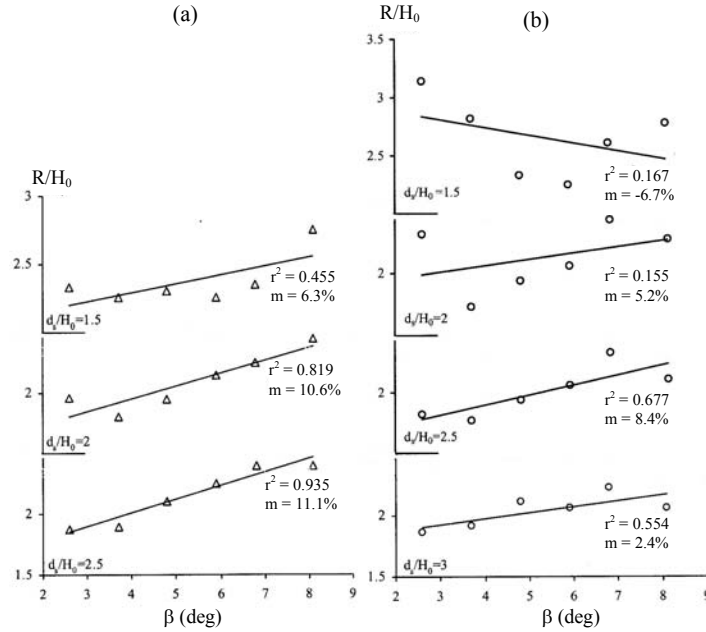


Fig. 7: Variation of R/H_0 with β : (a) $\zeta_0 = 2$, (b) $\zeta_0 = 3.2$.

The correlation coefficient (r^2) and the slope (m) of the best-fit curves drawn through each set of data points are also shown on these figures. Now, if we discard the curves at $d_s/H_0 = 1.5$ and 2 in Fig. 7(a) owing to the low values of r^2 , it appears that R/H_0 increases slightly at a rate of about 5 – 10% with β in degrees.

Finally, a word of caution. The wave run-up measurements reported in the present paper have been made over a smooth, impermeable slope, and therefore, it is not entirely clear whether these results are valid for rough, permeable slopes of coastal structures as well.

6. CONCLUSIONS

The following conclusions are drawn for the range of conditions covered in the present experiments of wave run-up over smooth sloping structures. The non-dimensional wave run-up (R/H_0) initially increases with the non-dimensional water depth at the toe of the structure (d_s/H_0), reaches a peak value at $d_s/H_0 \approx 1.2$, before beginning to fall and approach a nearly constant value for d_s/H_0 larger than about 2.5. The measurements also indicate that shallow water effects are important for values of d_s/H_0 falling between 0.8 and 2 with the maximum effect occurring at $d_s/H_0 \approx 1.2$. The maximum percentage increase of R/H_0 at shallow water depths with respect to the mean value in deep water ($d_s/H_0 > 2.5$) is about 20% for plunging breakers and about 65% for surging breakers. The measurements also seem to indicate that R/H_0 increases slightly with the foreshore slope angle.

ACKNOWLEDGMENT

The first author wishes to gratefully acknowledge the financial support from the Science & Technology Personnel Development Project of the Ministry of Science & Technology, Sri Lanka to enable him to carry out the experimental work described in the present paper.

REFERENCES

- [1] Ahrens J.P., "Irregular wave run-up on smooth slopes", *Tech. Aid No. 81-17*, Coastal Engineering Research Centre, Waterways Experiment Station, Vicksburg, Miss., 1981.
- [2] Losada M. A. and Gimenez-Curto L. A., "Flow characteristics on rough, permeable slopes under wave action", *Coastal Eng.*, 1981, **4**, 187-206.
- [3] Shankar N.J. and Jayaratne M.P.R., "Wave run-up and overtopping on smooth and rough slopes of coastal structures", *Ocean Eng.*, 2003, **30**, 221-238.
- [4] Wijetunge J.J. and Sarma A.K., "Effectiveness of 2D strip elements in wave run-up reduction over smooth slopes". *Engineer*, Journal of the Institution of Engineers, Sri Lanka, 2003, Vol. XXXVI, No. 3, Section-I, 39-46.
- [5] Kobayashi N., "Wave runup and overtopping on beaches and coastal structures", pp. 95-154, in Philip L.-F. Liu, *Advances in Coastal and Ocean Engineering*, Vol. 5, World Scientific, Singapore, 1999.
- [6] Van der Meer J.W. and Stam C.M., "Wave run-up on smooth and rock slopes of coastal structures", *ASCE J. Waterway, Port, Coastal and Ocean Eng. Div.*, 1992, **118** (5), 534-550.
- [7] De Waal J.P. and Van der Meer J.W., "Wave run-up and overtopping on coastal structures", Proc. 23rd Int. Conf. Coastal Eng., Venice, 1992, 1759-1771.
- [8] Battjes J.A., "Computation of set-up, longshore currents, run-up and overtopping due to wind-generated waves", Report 74-2, Committee on Hydraulics, Dept. of Civil Engrg., Delft Univ. of Technology, Delft, the Netherlands, 1974.

ORGANIZATION

The Asian Fluid Mechanics Committee

Chairman : Prof. M. Kiya (Japan)

Vice-Chairmen : Prof. E. Cui (China)
Dr T. S. Prahlad (India)

Members :

Prof. Y. T. Chew (Singapore)
Prof. M. S. Chong (Australia)
Prof. Y. Fukunishi (Japan)
Prof. B. H. Lakshmana Gowda (India)
Prof. F. Hussain (USA)
Prof. A. K. M. Sadrul Islam (Bangladesh)
Prof. Jameel Ahmad Khan (Pakistan)
Prof. R. Narasimha (India)
Prof. H. Sato (Japan)
Prof. E. Shirani (Iran)
Prof. S. Sivasegaram (Sri Lanka)
Prof. R. M. C. So (Hong Kong)
Prof. M. Sun (China)
Prof. H. J. Sung (Korea)

ACFMX Organizing Committee

Chairman : Prof. S. Sivasegaram

Secretary : Dr S. B. Weerakoon

Treasurer : Dr K. P. P. Pathirana

Editor : Dr J. J. Wijetunge

Members :

Dr D. C. Bandara
Dr P. B. Boyagoda

Dr U. I. Dissanayake
Dr J. B. Ekanayake
Dr G. B. B. Herath
Dr D. G. G. P. Karunaratne
Dr H. H. J. Keerthisena
Dr K. D. W. Nandalal
Dr S. D. Pathirana
Prof. M. P. Ranaweera
Dr K. B. N. Ratnayake
Dr U. R. Ratnayake
Dr I. M. S. Satyaprasad
Prof. Nimal Seneviratne
Mr S. K. Seneviratne
Dr R. Shanthini
Dr K. S. Walgama
Dr D. R. I. B. Werellagama
Mr S. B. Wijekoon

ACFMX National Advisory Committee

Dr Sarath Abeywardene, *International Water Management Institute*
Mr N. A. Amaradasa, *Department of Meteorology*
Mr Ajit de Costa, *Central Environment Authority*
Mr K. S. R. de Silva, *National Water Secretariat*
Mr Russel de Zilva, *The Institution of Engineers, Sri Lanka*
Prof. Luxman Dissanayake, *Postgraduate Institute of Science*
Dr R. Galappatti, *Lanka Hydraulic Institute*
Dr P. P. Gunaratne, *University of Ruhuna*
Ms L. Haturusinghe, *Mahaweli Authority of Sri Lanka*
Prof. S. S. L. Hettiarachchi, *University of Moratuwa*
Mr H. B. Jayasekara, *Central Engineering Consultancy Bureau*
Mr Tissa Jinasena, *Jinasena Limited*
Mr M. A. Ranjit Kularatne, *National Aquatic Resources Research and Development Agency*
Prof. C. M. Madduma Bandara, *National Water Secretariat*
Mr Malith Mendis, *Lanka Hydraulic Institute*
Ms V. Nallathambi
Dr S. M. A. Perera
Mr L. L. Premanath, *National Water Supply and Drainage Board*
Mr Nimal Rajapakse, *Ceylon Petroleum Corporation*
Mr Ranjit Rodrigo, *National Engineering Research and Development Centre*
Dr R. A. D. B. Samaranayake, *Coast Conservation Department*
Mr Mahinda Samarasekara, *Mahaweli Authority of Sri Lanka*
Prof. K. Tennakoon, *Institute of Fundamental Studies*
Mr D. W. R. Weerakoon, *Irrigation Department*
Dr Nalin Wickramanayake, *The Open University of Sri Lanka*
Mr D. C. Wijeratne, *Ceylon Electricity Board*
Mr Koichi Yamanaka, *Colombo Dockyard Limited*

ACFMX Invited Lecturers

Plenary Lectures

Prof. Hassan Aref
Prof. Lord Julian Hunt
Dr P. N. Shankar
Prof. Shigeo Kida
Prof. K. R. Sreenivasan

Special Lectures

Prof. G. S. Bhat
Prof. H. J. S. Fernando
Prof. Hiroshi Hayami
Prof. Guowe He
Prof. Jae Min Huyn
Prof. Tissa Illangasekare
Prof. Lin Jianzhong
Prof. Rene Kahawita
Prof. Joseph H. W. Lee
Prof. Sanjay Mittal
Prof. B. N. Raghunandan
Prof. Yasushi Takeda

EFFECT OF ROUGHNESS HEIGHT AND REFERENCE BED LEVEL ON BED SHEAR STRESS IN OPEN CHANNEL FLOWS

P.C. Ranasinghe, K.P.P. Pathirana and U.R. Ratnayake

Department of Civil Engineering, University of Peradeniya, Peradeniya 20400, Sri Lanka

ABSTRACT: An accurate estimation of bed shear stress is vital for sediment transport studies in open channels, rivers and streams. Although, several methods are available for calculation of bed shear stress, they do not produce comparable results due to the variability of the hydraulic parameters involved. Among these roughness height and reference bed level are predominant. A series of laboratory experiments were carried out in order to investigate the effect of these parameters on bed shear stress. Velocity profiles were measured and shear velocities were calculated using five different methods. Comparison of the results showed that the shear velocity estimated by these methods vary within a wide range. Roughness height and the reference bed level significantly influenced the shear velocity. This paper also addresses the sensitivity of these two parameters on shear velocity and an attempt has been made to correlate them with the governing parameters that define the hydraulic problem.

1. INTRODUCTION

Bed shear stress is one of the important parameters required in estimating the sediment transport rates in streams, rivers, canals etc. This parameter plays a vital role in designing stable channels on alluvial plains. An accurate estimation of this parameter is therefore essential. Although, several methods are available for calculation of the shear stress with different underlying assumptions, they do not produce comparable results^[3]. As a result, it is difficult to develop sediment transport models for accurate prediction.

As the sediment transport phenomenon is a problem of two phase motion, calculation of bed shear stress relates to the properties of the fluid, sediments and the mechanical characteristics of the flow. Among the parameters required to describe these properties, equivalent roughness height and the water depth have a significant role and are highly sensitive to shear velocity. However, estimation of a representative value of roughness height for natural bed is difficult and also, no established methods are available for this purpose. In addition, defining a datum level for measurement of water depth is also difficult. This paper highlights the sensitivity of these two parameters on bed shear stress.

As a direct relationship between the bed shear stress and the shear velocity is available, estimation of shear velocity can be used to represent the bed shear stress. During this study, a series of laboratory experiments were carried out to measure the velocity profiles in open channel flows on fixed rough bed. Using these velocity profiles, the shear velocity was estimated with five different methods and they were compared to establish a preliminary guideline for specifying the representative roughness height and water depth.

2. COMPUTATION OF SHEAR VELOCITY

Shear velocity (u_*) was calculated using the following five different methods. In each method, the sensitivity of k_s and y on u_* was investigated.

Method 1:

For a hydraulically rough bed, velocity distribution over the water depth is given by the following logarithmic equation^[2].

$$\frac{u}{u_*} = 8.5 + 2.5 \ln \left(\frac{y}{k_s} \right) \quad (1)$$

where, k_s is the equivalent roughness height, u the velocity and y the water depth. u_* is obtained from the gradient of the plot of u vs. $\ln(y/k_s)$ for the near-bed observations. This method has the important advantage that the gradient of the line is independent of k_s .

Method 2:

By using the intercept of the same plot of u vs. $\ln(y/k_s)$ the values of u_* were calculated. But in this case, the intercept of the line is dependent on k_s value.

Method 3:

Compute values of u_* using equation (1) for individual velocity measurements at near-bed depths of the section considered. u_* of the section was then calculated by taking the average. This requires an independent estimation of k_s .

Method 4:

The relationship between mean velocity and u_* is given by ^[4],

$$\frac{U}{u_*} = 6.25 + 5.75 \log \left(\frac{R_h}{k_s} \right) \quad (2)$$

where U is the mean velocity and R_h is the hydraulic radius. u_* is calculated using the mean velocity of the flow at a particular section using equation (2). This again requires an independent estimation of k_s .

Method 5:

The shear velocity for steady uniform flow is given by;

$$u_* = \sqrt{g R_h s} \quad (3)$$

where, R_h is the hydraulic radius and s is the channel bed slope.

3. EXPERIMENTAL SETUP

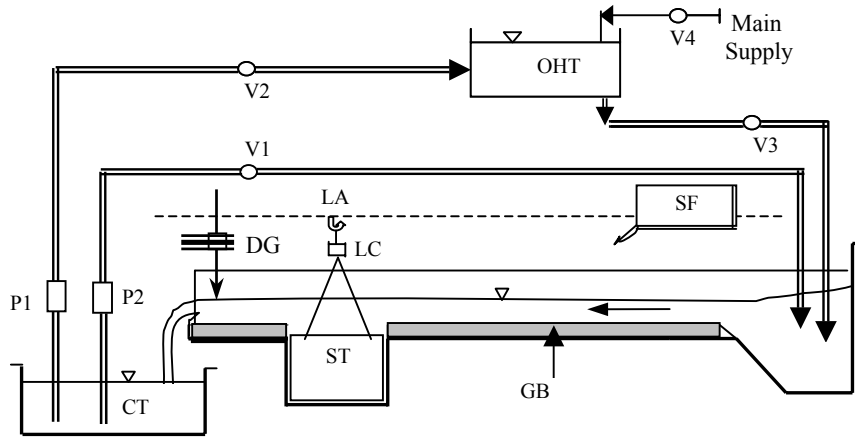


Figure 1. Experimental set-up

P1, P2 - Pumps

CT - Collection tank

LA - Lifting arrangement

ST - Sediment trap

V1, V2, V3, V4 - Valves

DG - Depth Gauge

LC - Load cell

SF - Sediment feeder

GB - Fixed gravel bed

OHT - Overhead tank

UT - Upstream tank

The experiments were carried out in a 10 m long, 0.4 m wide, 0.5 m deep, rectangular, re-circulating, tilting flume in the Hydraulics Laboratory of University of Peradeniya. A sharp crested weir is fixed at the end of the channel with a depth gauge to facilitate the estimation of flow discharges. A schematic diagram of the experimental set-up is shown in Figure 1.

4. EXPERIMENTAL PROCEDURE

Several experiments were performed for four different discharges and four different slopes, keeping the same fixed bed. The channel bed was prepared using natural river sediments with a non-uniform grain size distribution and d_{50} of 4 mm. For each experiment, the velocity profiles were measured at 10 different sections along the channel. Based on these observations, it was found that the fully developed flow was established by the section at 4.5m.

The velocities were measured by a 5 mm diameter micro propeller current meter coupled with an A/D converter. The readings were recorded at a 50 Hz frequency for 30 seconds per point. Water depths were recorded at a section 5.5 m downstream from the channel flow entrance.

5. RESULTS AND DISCUSSION

A set of measurements taken on velocity profiles at the 5.5m section are shown in Figure 2.

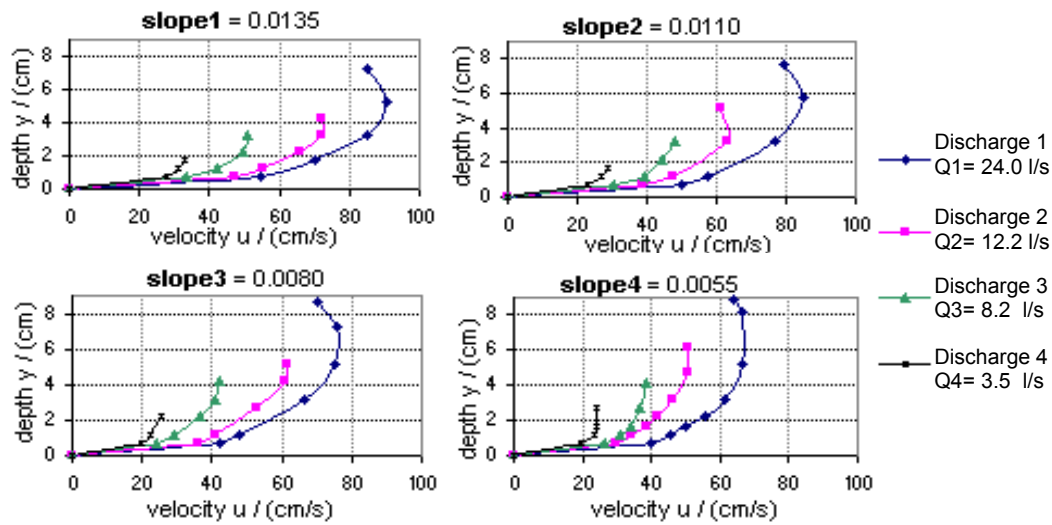


Figure 2 : Velocity profiles measured at 5.5 m section.

There are different empirical formulas proposed by several investigators to estimate the roughness height k_s . Some of them are listed in Table 1^[1] with the corresponding k_s values for the sediments used in this study.

The reference bed level for the velocity measurements was taken to be 4 mm below the top most level of grains as illustrated in Figure 3. The sign convention adopted to show the change of reference bed level is also given in the same figure.

Table 1. Equivalent roughness heights proposed by different investigators

Investigator(s)	Empirical Formula for k_s	Corresponding k_s value / (mm)
Ackers-White	$1.25 d_{35}$	3.8
Engelund-Hansen	$2.0 d_{65}$	10.0
Kamphuis	$2.5 d_{90}$	16.8
van Rijn	$3.0 d_{90}$	20.1
Hey	$3.5 d_{85}$	21.7
Charlton	$3.5 d_{90}$	23.5
Mahmood	$5.1 d_{84}$	31.6

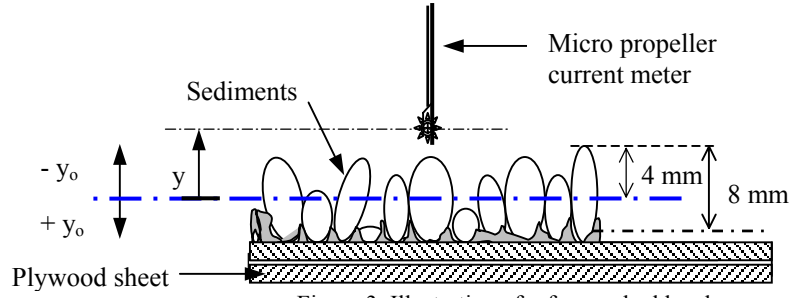


Figure 3. Illustration of reference bed level.

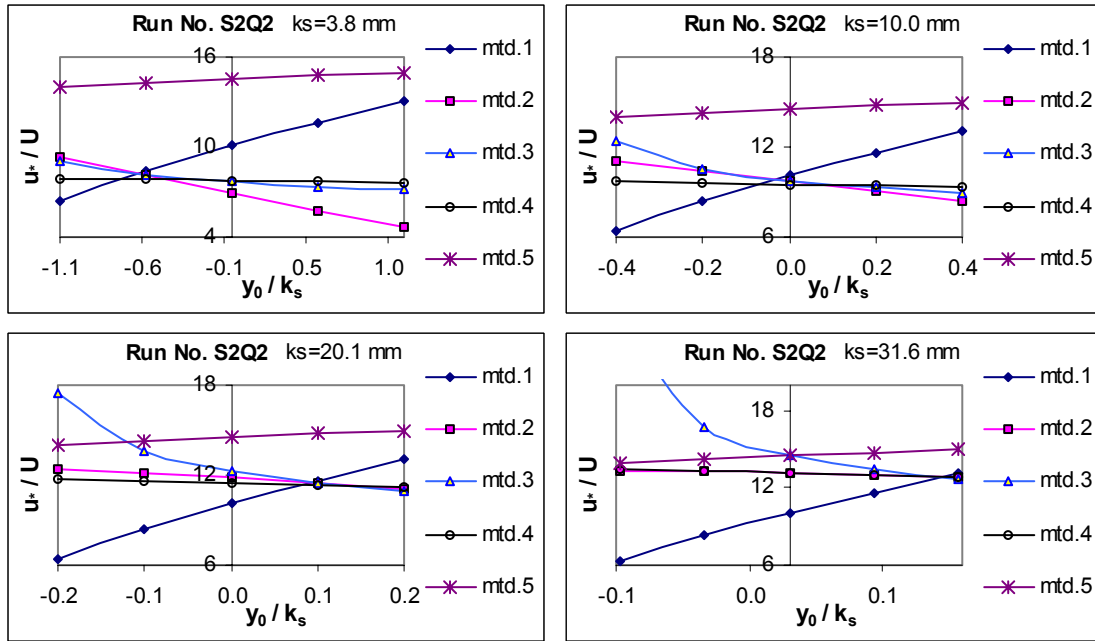


Figure 4. Typical Variation of different u^*/U values with y_0/k_s .

To see the variation of shear velocity with reference bed level, the bed level was changed by ± 2 to 4 mm in steps and then shear velocities were computed using five different methods. Figure 4 shows the non-dimensional plots of (u^*/U) vs. (y_0/k_s) obtained with 12.2 l/s discharge and 0.0110 bed slope, for four different values of k_s .

These plots clearly show that the shear velocities calculated by method 1 are highly sensitive to the changes in the datum for measurement of water depth. Method 3 also becomes sensitive with increasing values of k_s . These two methods behave in opposite manner with the change of datum. Shear velocities given by the second and fourth methods show less sensitivity to change of datum. However, it is interesting to note that the shear velocities computed by first four methods are nearly the same at a particular value of reference bed level. This value also varies with the channel bed slope, discharge and roughness height and Table 2 summarizes the values of the datum for this common point for all the experimental runs.

Figure 4 also shows that the shear velocities calculated by the fifth method overestimates compared to the methods 1, 3 and 4 and it has a low sensitivity to the change of datum. Discrepancy of the results from fifth method from others may be due to the invalidity of the underlying assumptions, such as, validity of hydrostatic pressure distribution.

Table 2. y_0 values corresponding to common point for different k_s

Run No	Slope S	k_s /(mm)	3.8	10	16.8	20.1	23.5	31.6
		Q / (l/s)						
S1Q1	0.0135	24.0	-2.0	-0.2	1.2	1.8	2.4	3.6
S2Q1	0.0110	24.0	-2.2	-0.4	1.2	1.8	2.4	3.6
S3Q1	0.0080	24.0	-2.4	-0.4	1.2	1.8	2.2	3.6
S4Q1	0.0055	24.0	-0.6	1.4	2.8	3.2	3.8	5.0
S1Q2	0.0135	12.2	-1.6	0.2	1.6	2.2	2.8	4.0
S2Q2	0.0110	12.2	-2.4	-0.2	1.0	1.8	2.4	3.6
S3Q2	0.0080	12.2	-2.4	-0.6	1.0	1.4	2.2	3.2
S4Q2	0.0055	12.2	-1.2	0.4	1.6	2.2	2.8	3.6
S1Q3	0.0135	8.2	-1.6	0.4	1.8	2.4	3.0	4.4
S2Q3	0.0110	8.2	-1.4	0.6	2.2	2.8	3.4	4.6
S3Q3	0.0080	8.2	-1.8	0.0	1.4	1.8	2.4	3.6
S4Q3	0.0055	8.2	-0.2	1.6	3.0	3.6	4.2	5.2
S1Q4	0.0135	3.5	1.2	3.2	4.8	5.6	5.8	6.0
S2Q4	0.0110	3.5	0.6	2.8	4.4	5.2	5.6	6.0
S3Q4	0.0080	3.5	-0.8	0.8	2.0	2.6	3.2	4.2
S4Q4	0.0055	3.5	-0.4	1.4	2.8	3.4	3.8	5.0

6. CONCLUSIONS

Effect of roughness height and datum for measurement of water depth on bed shear stress was analyzed in detail using a laboratory experimental setup. Five different methods as described in section 2 were used for calculating bed shear stress using the experimental results. The shear velocities computed by the methods 2, 4 and 5 show a less sensitivity to the change of reference bed level, while the other two methods were highly sensitive. In general, the five methods resulted in a wide variation of the shear velocity calculated with same hydraulic conditions. However, it is not possible to state which method is more reliable as the actual values of shear velocities to estimate bed shear stresses are not available.

As a preliminary result of this study, it is noted that for a given set of hydraulic parameters, the first four methods resulted in approximately the same shear velocity at a particular reference bed level. Further investigations covering wider range of experimental conditions are necessary to establish a reliable relationship between the bed shear stress and the hydraulic parameters.

ACKNOWLEDGMENTS

The authors wish to acknowledge the financial support given by the National Science Foundation, Sri Lanka, Grant Number CRG/98/P/02. and the scholarship through the Science and Technology Development Programme of ADB.

REFERENCES

- [1] Chang, HH: *Fluvial Processes in River Engineering*. John Wiley and Sons, Inc, 1988.
- [2] Chien N, Wan Z: *Mechanics of Sediment Transport*. The American Society of Civil Engineers, ASCE Press, 1998.
- [3] Kabir MR, Trofs H: Comparison of different methods to calculate bed shear stress, Wat. Sci. Tech., Vol.25, No.8, 1992, 131-140.
- [4] Keulegan GH: Laws of turbulent flows in open channels, J. Res., Nat. Bureau of Standards, Vol.21, No.6, 1938, 707-741.

DISTRIBUTION OF EDDY VISCOSITY IN OPEN CHANNELS

M. Mohammadi

Faculty of Engineering, Azad University, Khoy branch, Khoy, Iran. (*part time*)
Department of Civil Engineering, Faculty of Engineering, Urmia University, Urmia 57169-33111, Iran.

ABSTRACT: In open channel flows, the estimation of local and global eddy viscosity are the most important tasks and sometimes very difficult. This difficulty arises from the existence of the secondary flow cells and boundary induced turbulence, both of which affect the distributions of velocity and boundary shear stress, and consequently the eddy viscosity. A series of measurements were undertaken for velocity and boundary shear stress in fully developed turbulent uniform flow for a smooth open channel. Using the measured local depth-averaged velocity, U_d , and the local bed shear stress, τ_b , the local depth-averaged bed friction factor, f_b , was calculated for each lateral position. Using the analysis of local friction factor and apparent shear stress, τ_a , the distribution of depth-averaged eddy viscosity, ε_{yx} , is analyzed by applying $\bar{\tau}_a = \rho \bar{\varepsilon}_{yx} (\partial U_d / \partial y)$. The distribution of depth-averaged eddy viscosity was found to increase from the channel centerline to the sidewalls. The results reveal that the overall values of eddy viscosity increase as Froude number increases. The averaged values of depth-averaged dimensionless eddy viscosity, λ_{ave} , show that there is a significant reduction in λ_{ave} values as the flow discharge increases. The results point out that the value of λ_{ave} is not necessarily a constant, as often assumed in several computational models.

1. INTRODUCTION

Viscosity is an internal property of a fluid that offers resistance to flow. It is also a property of a fluid manifest as a resistance to flow. Eddy viscosity refers to the internal friction generated as laminar (smooth, steady) flow becomes irregular and turbulent as it passes over irregularities on the surface. Eddy motions created by obstructions are commonly referred to as mechanical turbulence. Turbulence is an irregular motion in fluid flows. The various flow quantities thus show random variation with time and space and only statistically averaged values are distinctively discerned. Turbulence is one of the most important unsolved problems of classical physics. The development of modern computer technology has changed this situation and provided opportunities for engineers to argue with turbulent flows using Computational Fluid Dynamics (CFD) techniques.

It has been a difficult task for the majority of researchers to find an applicable way to measure the local eddy viscosity and its distribution around a wetted perimeter. The problem is complex, especially for the case of turbulent flow which rules out rigorous analysis on the basis of boundary layer theory. In spite of the difficulty of the direct measurement, which is due to the small shear forces, a number of investigators have attempted to use it. This paper deals with the analysis of experimental data taken for velocity and boundary shear stress, together with analysis of the results obtained so far for apparent shear stress as well as eddy viscosity.

2. BACKGROUND THEORY

Using the Navier-Stokes equations and solving these equations for open channels, it is possible to predict the eddy viscosity distribution. It is also possible to measure local velocity and local boundary shear stress and thus applying Navier-Stokes equations solution, the eddy viscosity can be computed. Some of the recent studies in open channel flows on the subject of boundary shear stress have been made by Nezu & Rodi (1986), Knight et al (1994); Mohammadi (1998) and Mohammadi & Knight (2004). The structure of flow in open channels is directly affected by the shear stress distribution along the channel wetted perimeter and consequently the shear velocity and eddy viscosity are put into account. It has long been established that many factors influence this distribution, such as the variation of longitudinal and

lateral boundary roughness type, geometry of cross section, longitudinal variation of planform geometry, sediment concentration and its deposition on the bed.

To understand the lateral distribution of eddy viscosity, the general 3D flow structure in prismatic channels needs to be examined by referring to the governing equations, such as the momentum equations of Navier-Stokes or Reynolds for unsteady 2D open channel flows i.e. $\partial/\partial y = 0$ is given as (Nezu & Nakagawa, 1993)

$$\frac{\partial U}{\partial t} + \frac{\partial U^2}{\partial x} + \frac{\partial UW}{\partial z} = gS_s + \frac{\partial}{\partial z} \left(\frac{\tau}{\rho} \right) \quad (1)$$

where, U and W are the mean velocity components in streamwise and normal directions, respectively, $S_s = \sin \theta - (dh/dx) \cos \theta$ is the surface slope (unsteady flow), and h is the flow depth. Since $|\partial U / \partial t| \gg |\partial U^2 / \partial x|$, the local shear stress τ , can be obtained by integrating eq. (1), from z to the free surface $z=h$ as:

$$\frac{\tau}{\rho} = gS_s(h-z) + \int_h^z \frac{\partial U}{\partial t} dz \quad (2)$$

or:

$$\frac{\tau_b}{\rho} = gS_s h - \int_0^h \frac{\partial U}{\partial t} dz \cong gS_s R - \frac{\partial Q}{B \partial t} = u_*^2 - \frac{1}{B} \frac{\partial Q}{\partial t} \quad (3)$$

in which, Q is the flow discharge, B is the channel width, u_* is the shear velocity and R is the adopted hydraulic radius for the sidewall effects. Nezu & Nakagawa (1993 & 1995) have provided a detail account of the bed shear stress in unsteady open channel flows. They also used LDA technique to measure the velocity distributions, from which boundary shear stress has been evaluated. In the case of steady flows in prismatic straight channels, Shiono & Knight (1991) solved the N-S equation in 2D form and showed that the local bed shear stress, τ_b , may be derived as

$$\tau_b \sqrt{1 + 1/s^2} = \rho g h S_0 - \frac{\partial}{\partial y} \left\{ h \left[(\rho \bar{U} \bar{V})_d - \bar{\tau}_{yx} \right] \right\} \quad (4)$$

where, h is the local depth, S_0 is the channel bed slope, s denotes the channel side slope ($s.h:1.v$), $(\rho \bar{U} \bar{V})_d = \bar{\tau}_{yx} - \bar{\tau}_a$ is the depth-averaged secondary current term, $\bar{\tau}_a$ is the depth-averaged apparent shear stress acting on a vertical interface given by

$$\bar{\tau}_a = -\frac{1}{h} \int_0^y \left[\rho g h S_0 - \tau_b \sqrt{1 + (1/s^2)} \right] dy \quad (5)$$

and $\bar{\tau}_{yx}$ is the depth-averaged Reynolds stress obtained by

$$\bar{\tau}_{yx} = \rho \bar{\epsilon}_{yx} \frac{\partial U_d}{\partial y} \quad (6)$$

in which $\bar{\epsilon}_{yx} = \nu_t / \rho$ is the depth-averaged eddy viscosity determined by

$$\bar{\epsilon}_{yx} = \lambda u_* H \quad (7)$$

where, H is total flow depth, u_* is the shear velocity, ν_t is the eddy viscosity due to turbulence, and λ is the dimensionless eddy viscosity. Nezu & Rodi (1986) obtained experimental values of eddy viscosity, $[\nu_t / (hu_*)]$, distribution for a given z/h using LDA data shown in Fig. 1.

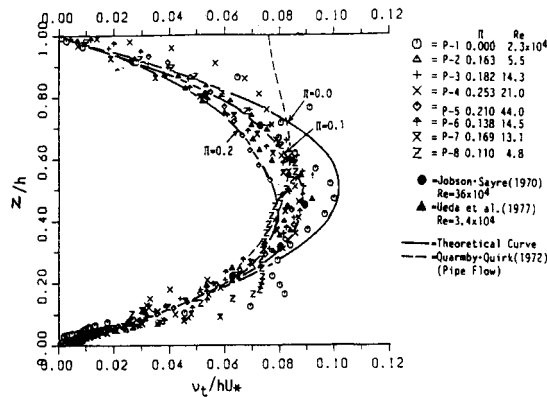


Fig. 1 Distribution of dimensionless eddy viscosity in an open channel (after Nezu & Rodi, 1986)

3. EXPERIMENTAL APPARATUS AND PROCEDURE

To investigate the hydraulic characteristics of a channel cross section, a series of experiments was conducted for measuring *point velocity* and *boundary shear stress* around wetted perimeter. The experimental channel (see Fig. 1) was built inside the existing 15 m long tilting flume. A Preston tube was used for measuring dynamic pressures to evaluate boundary shear stress (Preston, 1954, Head & Rechenberg, 1962 and Patel, 1965). Propellers were used to measure point velocities. For a certain channel bed slope, a discharge was introduced and uniform flow was established using stage-discharge results and discharge-tailgate relationships. The flume was supported by two hydraulic jacks and rotated about a hinge joint beneath the middle of the channel. The flume also had a motorized slope control system with a mechanical visual read out on a ruler at the upstream end of the flume used for determining the precise channel bed slope. Water was supplied to the channel by an overhead tank through a 101.6 mm pipeline for discharges up to 30 l/s and a 355.6 mm pipeline for discharges higher than 30 l/s. To reduce large-scale disturbances, and in order to ensure that the flow was uniformly distributed, a system of honeycombing was placed at the upstream end of the channel where the entrance tank and bell-mouth shaped inlet transition section were located. However for the case of supercritical flow i.e. $Fr > 1$ the honeycomb was not very useful. Individual bell-mouth shaped transition sections were designed and made for each channel types and served to reduce separation and improve the development of the mean flow into the channels. Discharge measurements (up to 30 l/s) were made by means of a Venturi meter connected to mercury and air/water manometers at the head of the flume. For the case of higher discharges a dall-tube connected to an air/water manometer was used in the 355.6 mm diameter supply line. A slatted tailgate weir was installed in the downstream end of the channel in order to minimize upstream disturbance of the flow, and hence allowed a greater reach of the channel to be employed for experimental measurement in subcritical flows.

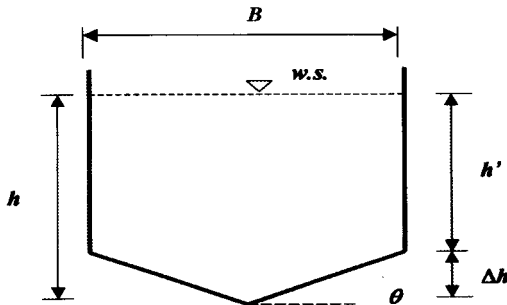


Fig. 2 Geometry of a V-shaped bottom channel and notation: $B=460$ mm, $\Delta h=50$ mm; & $h_{max}=300$ mm.

4. APPARENT SHEAR STRESS ANALYSIS

Using the balance of the resolved gravity force in the flow direction and the opposing shear force over the section bounded by the channel boundary and a vertical interface, the apparent shear force acting on any vertical slice of channel cross section is evaluated. The measured boundary shear stress results were therefore used for the evaluation of the apparent shear stress, τ_a . Integrating eq. (5) and using the local boundary shear stress, τ_l , gives the depth-averaged apparent shear stress, $\bar{\tau}_a$, calculated by

$$\bar{\tau}_a = \frac{1}{h} \left\{ \int_0^y \rho g S_0 dA - \int_0^y \tau_l dP \right\} \quad (8)$$

where h is the flow depth from lower point of the channel cross section, P is the total wetted perimeter, A is the cross sectional area, y is the lateral location of the vertical interface elements measured from the extreme left hand side of the channel towards the centerline. Fig. 3 shows an example of the lateral distribution of apparent shear stress along wetted perimeter. Using the force balance analysis, it is assumed that the apparent shear stress is zero in centerline, as the channel section has a symmetric cross section. Therefore it can be seen that both values of the apparent shear stress and shear force generally increase from channel centerline reaching a value of wall shear stress at the channel wall. It can also be seen that as the flow discharge increases both apparent shear stress and shear force increase (Mohammadi, 1998). The results also indicate that for a certain flow discharge, as the channel gets steeper, both the apparent shear stress and shear force increase. This result confirms that the energy due to the gradient and gravity is more dominant.

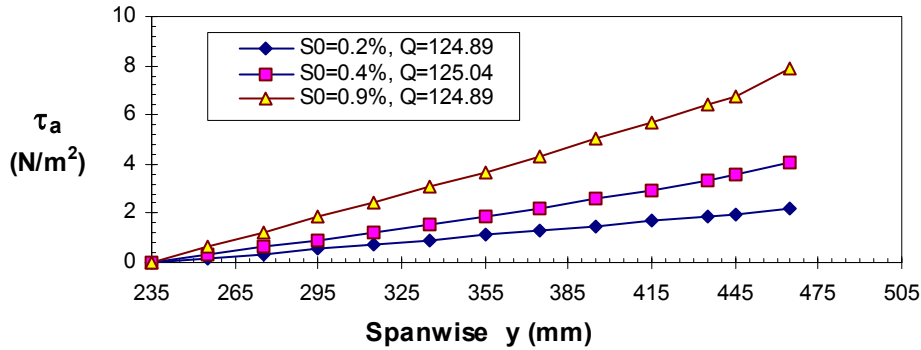


Fig. 3 Lateral distribution of depth-averaged apparent shear stress at different channel bed slope, S_0 , for $Q=125$ l/s.

In some cases the values of apparent shear stress and consequently apparent shear force values along wetted perimeter obtain some reduction values near wall. Herein, this means that the boundary shear force in the considered subsection is greater than the fluid weight component and thus the apparent shear force along wetted perimeter acts as a balancing force and sustains the flow in this subsection (see Mohammadi, 1998). This suggests that a net momentum is brought into the subsections near the corners crossing the vertical interface from the faster moving fluid in the corner of the channel. The apparent shear force results were used for estimating the depth-averaged eddy viscosity distributions, as explained in the following section.

5. DEPTH-AVERAGED EDDY VISCOSITY AND DIMENSIONLESS EDDY VISCOSITY, λ ,

Another use to which the boundary shear stress and shear force data may be put is in the determination of depth-averaged eddy viscosity and dimensionless eddy viscosity. As explained in previous section, eq. 8 gives the depth-averaged apparent shear stress in the spanwise direction, y . According to Knight et al (1994), in open channel flows analysis based on the depth-averaged parameters, the apparent shear stress on a vertical interface is often related to the lateral gradient of the depth-

averaged velocity by the depth-averaged eddy viscosity, $\overline{\varepsilon}_{yx}$. Introducing an equation for apparent shear stress like eq. 6 gives

$$\overline{\tau}_a = \rho \overline{\varepsilon}_{yx} \frac{\partial U_d}{\partial y} \quad (9)$$

Therefore using the calculated values of $\overline{\tau}_a$ and polynomial equations which express the depth-averaged velocity gradients, for every position of the channel section, the values of $\overline{\varepsilon}_{yx}$ were calculated. Eq. 7 calculates the depth-averaged eddy viscosity values in a non-dimensionalized form using the local boundary shear velocity values. Equations 7 & 8 were used to evaluate the depth-averaged eddy viscosity and its dimensionless value, λ . Eq. 8, however, adopts some ancillary equations for the polynomials to explain the depth-averaged velocity gradients. The depth-averaged velocities are again arranged to define equations for U_d as a function of y . Fig. 4 shows an example of the lateral distribution of depth-averaged eddy viscosity, $\overline{\varepsilon}_{yx}$. It can be seen from the Figures likewise Fig. 4 that the depth-averaged eddy viscosity values are approximately constant over a part of the channel bed region ($300 < y < 400$ mm). The lateral distribution of dimensionless depth-averaged eddy viscosity, λ , reveals that the trends for λ are similar to those obtained for $\overline{\varepsilon}_{yx}$. It is clear that either the values of $\overline{\varepsilon}_{yx}$ or the values of λ do not remain constant approaching the wall and centerline of the channel. It may be seen that for a certain flow discharge both of them increase as the channel getting steeper or Froude number increases.

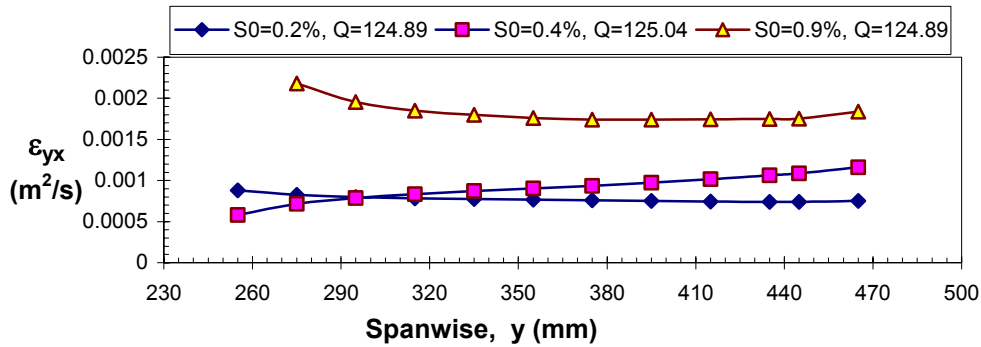


Fig. 4 Lateral distribution of depth-averaged eddy viscosity: $Q=125$ l/s.

In order to construct the variation of λ with channel bed slope, S_0 , and flow discharge, Q , a Table of data analysis was constructed (see Mohammadi, 1998). The variations of λ with channel bed slope, S_0 are analyzed. The results illustrate that the values of λ generally increase as the channel becomes steeper. Fig. 5 shows the variation of averaged values of λ with flow discharge, Q , in the range of experiments carried out. This Figure gives a good power-law relationship between the averaged values of depth-averaged dimensionless eddy viscosity, λ_{ave} , and flow discharge, Q , as

$$\lambda_{ave} = 2.5631Q^{-0.6732} \quad (10)$$

This equation clearly shows that the value of averaged λ reduces as the flow discharge increases.

It may be noted that the peak value for depth-averaged λ , near the channel wall, was not taken into account for estimating the values used to produce Figures likewise Fig. 4. The writer believes that λ is a very sensitive parameter and an important one for developing 2D models in open channel flows. It is worth mentioning that the viscosity due to the turbulence behavior denoted by ν_t is often used in open channel flow analysis, and is given by $\nu_t = \overline{\varepsilon}_{yx}$.

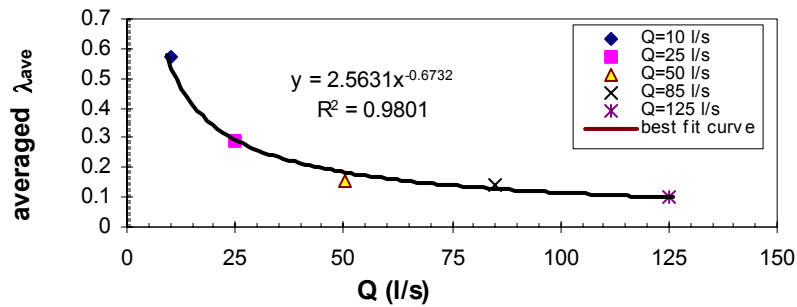


Fig. 5 The averaged depth-averaged values of dimensionless eddy viscosity, versus flow discharge, Q .

6. CONCLUDING REMARKS

Based on the results already presented in previous sections, the main findings are as follows:

1. The depth-averaged apparent shear stress and apparent shear force distributions have been shown to be a function of the transverse distance.
2. The dissipation of turbulence kinetic energy is shown to increase with increasing channel bed slope, i.e. increasing Fr number. This is associated with increased production rates of turbulence kinetic energy in the near wall region which is in accordance with the decrease of viscous sublayer in turbulent flows with steeper slopes. Turbulence intensity measurements are required in order to prove this proposition.
3. The distribution of the depth-averaged eddy viscosity was found to increase from the channel centerline to the sidewalls. It was found to follow a non-linear relationship with spanwise distance. The overall values of eddy viscosity increase as the Froude number increases.
4. The averaged values of depth-averaged dimensionless eddy viscosity, λ_{ave} , show that there is a significant reduction in λ_{ave} values as discharge increases. The results indicate that the value of λ_{ave} is not necessarily a constant value for any flow condition, as often assumed in several computational models.
5. The information in this paper may prove useful to any computational modelers dealing with channels with a similar shape. The work may also be valuable to river engineers.

REFERENCES

- [1] Head, MR and Rechenberg, I: The Preston Tube as a means of Measuring Skin Friction. *J. Fluid Mechanics*, 1962, Vol. 14, UK.
- [2] Knight DW, Yuen, KWH and Alhamid, AAI: Boundary Shear Stress Distributions in Open Channel Flow. in *Physical Mechanisms of Mixing and Transport in the Environment*, Ch. 4, (ed. K. Beven, P. Chatwin & J. Millbank), *J. Wiley*, 1994, pp. 51-87.
- [3] Mohammadi, M. Resistance to Flow and the Influence of Boundary Shear Stress on Sediment Transport in smooth Rigid Boundary Channels. *PhD Thesis*, School of Civil Engineering, Birmingham University, 1998, England.
- [4] Mohammadi, M and Knight, DW: Boundary Shear Stress Distribution in Open Channels. *Proceedings International Conference on Dams & River Structures*, KNT University of Technology, 26-28 April, 2004, Tehran, Iran. (*accepted*)
- [5] Nezu, I and Rodi, W: Open-Channel Flow Measurements with a Laser-Doppler Anemometer. *J. Hydraulic Eng.*, 1986, 112, 335-355.
- [6] Nezu, I and Nakagawa, H. *Turbulence in Open-Channel Flows*. IAHR-Monograph, 1993, Balkema.
- [7] Nezu, I and Nakagawa, H: Basic Structure of Turbulence Structures in Unsteady Open-Channel Flows. in 1994 Scientific Research Activities on Turbulence Structure and the Related Environment in Various Water Flows, (edited by Nakagawa & Nezu), 1995, Vol. 8, April.
- [8] Patel, VC: Calibration of the Preston Tube and Limitations on Its Use in Pressure Gradients. *J. Fluid Mechanics*, Vol. 23, Part 1, 1965, pp. 185-208.
- [9] Preston, JH: The Determination of Turbulent Skin Friction by Means of Pitot Tube. *J. Royal Aeronautical Society*, 1954, Vol. 58, February.
- [10] Shiono, K and Knight DW: Turbulent Open Channel Flows with Variable Depth across the Channel. *J. Fluid Mechanics*, 1991, Vol. 222, pp. 617-646.

FLOW AROUND A CIRCULAR CYLINDER WITH PERIODIC DISTURBANCE

Y.Kozato and S.Imao

Department of Mechanical and Systems Engineering, Gifu University,
1-1 Yanagido, Gifu, 501-1193, Japan

ABSTRACT: In order to verify the effect of the periodic disturbance on the control of the force exerted by a fluid, an experimental investigation of a flow around a circular cylinder with the high-frequency acoustic excitation was conducted. The mean and fluctuating pressure on the cylinder surface were measured and phase-averaged pressure distributions were calculated. The acoustic excitation which affect on the forces has a frequency corresponds approximately with that of the transition waves in separated shear layers. In particular, the fluctuating lift force has been increased and decreased about 20 % compared with the case of no excitation.

1. INTRODUCTION

If the bluff body such as a circular cylinder is located in the uniform flow, fluctuating aerodynamic force arises by the vortex shedding in the wake. Since these periodic vortices frequently bring about aero-elastic vibration and noise, serious damage in the structure and surrounding environment is brought.

The incidence of periodic vortices as typified by Karman vortex street, is concerned with the boundary layer separated from the surface (separated shear layer). It is known that this shear layer is very unstable to the disturbance and is disposed to amplify only a disturbance with specific frequency. Furthermore, this unstable fluctuation is called a transition wave and the order of this fluctuation is dozens times larger than that of Karman vortex shedding frequency is known. Consequently, several approaches are reported to control the separation and aerodynamic characteristics by exciting this unstable fluctuation.^[1-5] According to these report, the time-mean flow field and forces are affected by the acoustic excitation for the transition waves in separated shear layers. However, it has not been reached to the clarification of the effects on the fluctuating forces yet.

The objective of this study is to clarify aerodynamic characteristics and flow structure around a circular cylinder, vortex shedding characteristics and also the behaviour of disturbance in the separated shear layer imposing the acoustic excitation with simple and high frequency to the flow.

In this report, the possibility and the effect of the control for the force, especially the fluctuating components, exerted on a circular cylinder are studied.

2. EXPERIMENTAL SETUP AND PROCEDURE

The experiment was conducted in the wind tunnel that has the square section of 500×500 mm. Figure 1 shows the overview of measurement segment and main notations in this report are also shown. The resin pipe that diameter $D = 40$ mm is used for the cylinder and it is placed horizontally at the central part of the test section, which locates 750 mm downstream from the inlet section. Also, the pressure hole with the diameter of 0.4 mm is established in the span centre and the small pressure transducer (KULITE: XCS-062-5D) is inserted inside the cylinder. This pressure hole was able to set up with a given angle α by rotating the cylinder.

The characteristic frequency of the pressure measurement section that consists of pressure detection hole and sensing space is very high (about 10 kHz) and it may be disregarded the influence to the measured value by resonance with the acoustic disturbance.

The velocities were measured with a single-type hot-wire probe. Both the linearized output signal from the constant-temperature anemometer and amplified signal from the pressure transducer with a DC amplifier were converted by an A-D converter (resolution: 12 bit, sampling frequency: 10 kHz, observing

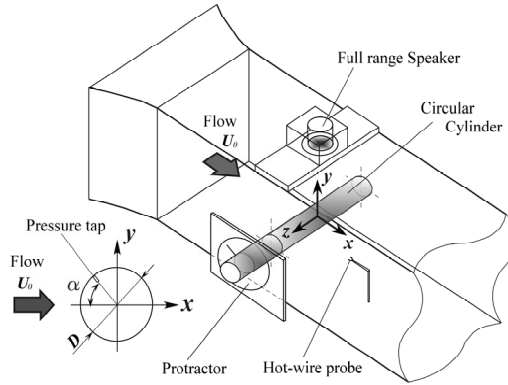


Fig.1 Experimental setup and main notations

time: about 13 sec), and the data was computed with a personal computer.

The acoustic excitation with the sine wave signal was generated from the function synthesizer and it is imposed to the flow by a speaker, which placed upper part of the test section. The sound pressure level was measured by a sound level meter located at the cylinder centre position and its level was kept constant every each frequency.

In this study, the sound pressure level (*SPL*) was kept to 120 dB at calm condition and the uniform flow velocity U_0 was varied from 10 to 20 m/s. Reynolds number based on a cylinder diameter was changed about 27000 to 53000.

3. EXPERIMENTAL RESULTS AND DISCUSSION

First of all, the influence of the acoustic excitation to the back pressure (surface pressure at the position $\alpha = 180$ deg) was checked. Figure 2 shows the variations of the back pressure to the disturbance frequency in the case that uniform flow velocity $U_0 = 20$ m/s. The vertical axis of figure **a**) denotes the non-dimensional time-mean back pressure in each excited condition P_b divided by the one without excitation P_{b0} , and figure **b**) shows the dimensionless RMS value of the fluctuating pressure p_b' / p_{b0}' . Both time-mean and fluctuating pressure increases and decreases in the same range of particular frequency compared with the case of no excitation. Furthermore, it is found that the degree of the variation of fluctuating pressure is more remarkable than that of the time-mean value. This tendency was observed similarly even if the main flow velocity was changed.

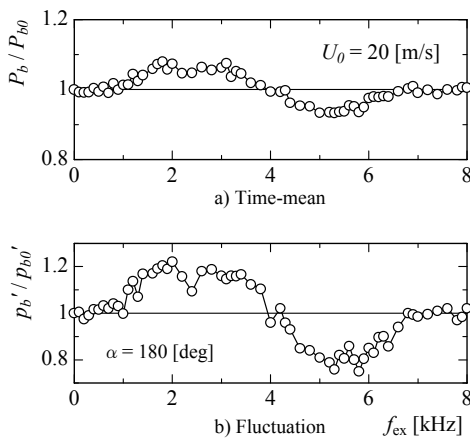


Fig.2 Variations of the cylinder back pressure

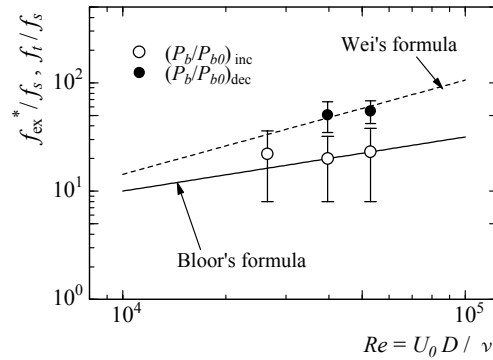


Fig.3 Effective frequencies

Figure 3 shows the frequencies that the influence of disturbance was detected against the mainstream velocity (i.e. the Reynolds number). The vertical axis shows the non-dimensional centre frequency f_{ex}^* when the back pressure is increased and decreased divided by Karman vortex shedding frequency f_s . The error bar shows the range of the frequency that the effect was found. In this figure, the solid line and broken line show the regression curves with the non-dimensional transition wave frequency f_t/f_s that are obtained by Bloor^[6] and Wei^[7], respectively. It seems that the effective frequency of the excitation corresponds to the frequency of the infinitesimal fluctuation called transition wave and the pressure field of cylinder surface can be handled by stimulating with the acoustic disturbance.

Figure 4 shows the pressure distribution on the circular cylinder with the acoustic excitation of close frequency to the centre value shown in Fig. 3. The vertical axis of figure **a**) shows the pressure coefficient of time-mean pressure based on the dynamic pressure of uniform flow ($C_p = P/(1/2 \rho U_0^2)$), and the vertical axis of figure **b**) is the pressure coefficient notation of the RMS value of fluctuating pressure ($C_p' = p'/(1/2 \rho U_0^2)$). Also, the coefficient of drag force calculated from the time-mean pressure distributions is denoted in the upper part of the figure. It is understood that the influence of disturbance appears near the trailing stagnation point ($\alpha = \pm 180$ deg) and it gives a little change to the mean drag force. On the other hand, the effect of the disturbance to the fluctuating pressure becomes remarkable behind the vicinity of separation point ($|\alpha| > 70$ deg) and it is expected that the disturbance give rise to a big change of the fluctuating forces.

In order to compare the frequency component of the fluctuating pressure in each condition, the power spectra are shown in Fig. 5 in the case of $\alpha = 80$ deg where the fluctuating pressures are biggest. The vertical axis of the figure represents a non-dimensional amplitude spectrum density of fluctuation divided by the dynamic pressure of the uniform flow. It is found that the component of Karman vortex shedding frequency distinguishes even in either condition and the obvious difference arises for the peak value corresponding to the increase and decrease of the RMS value that was described above. Furthermore, it is confirmed that even the frequency that shows a peak value varies slightly.

Consequently, to explain in which position of the cylinder surface the fluctuation of vortex shedding frequency component appears, the components are separated into the one originated in Karman vortex and the other component. Figure 6 shows the distribution of the separated fluctuating pressure component. The vertical axis shows the dimensionless RMS value given by the band-pass filtered fluctuating component around the vortex shedding frequency and that given by the band-eliminated component. Although the component that is originated in the vortex shedding is dominant except for the backward

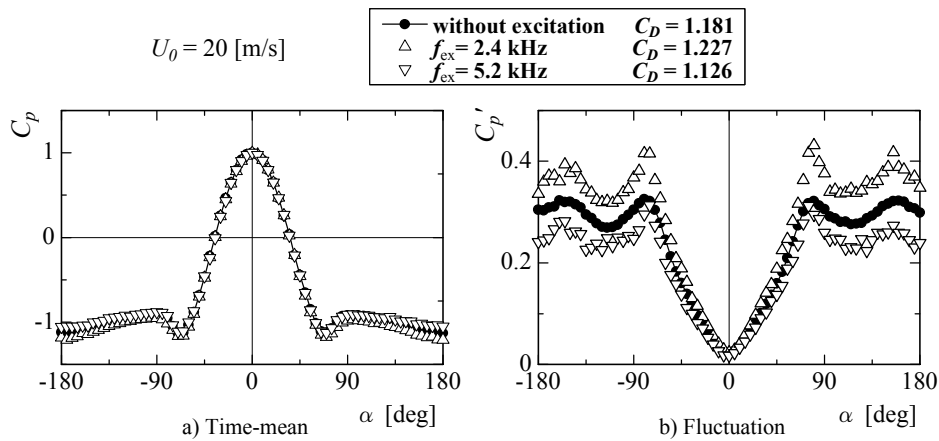


Fig.4 Pressure distributions on the cylinder surface

area ($|\alpha| > 160$ deg) in any condition, the effect of excitation is found to be especially conspicuous at the cylinder top and bottom sections. This result brings us expectations that the periodic disturbance may cause a large influence on the fluctuating lift force, which acts on a cylinder.

On the basis of the above result, the simultaneous measurement of the cylinder surface pressure and the velocity in the wake was conducted. The fluctuating component consistent with Karman vortex shedding was picked out and phase averaged processing was applied.

Figure 7 explains the phase detecting technique that was carried out in this experiment. Band-passed signal (middle row on the right figure) was used as the phase reference signal that is based on the velocity signal from the hot-wire probe (upper row on the right figure) placed at the left figure position, and the phase angle ϕ was determined by dividing each 1 cycle of signal equally. And, the pressure (lower signal on the right figure) in the time corresponding to each phase was picked out. As for the phase detecting position, it was chosen where the velocity fluctuation corresponding to the vortex shedding appears most clearly.

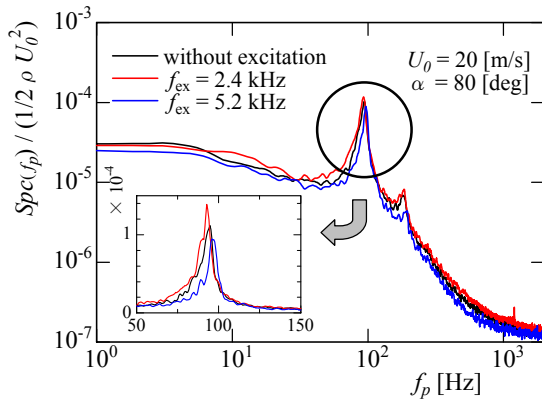


Fig.5 Power spectrum of the fluctuating pressure

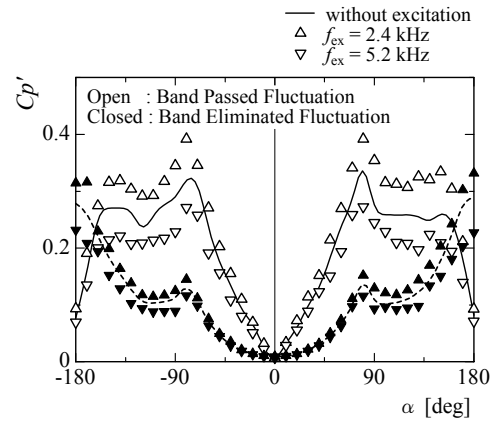


Fig.6 Distributions of the fluctuating pressure component

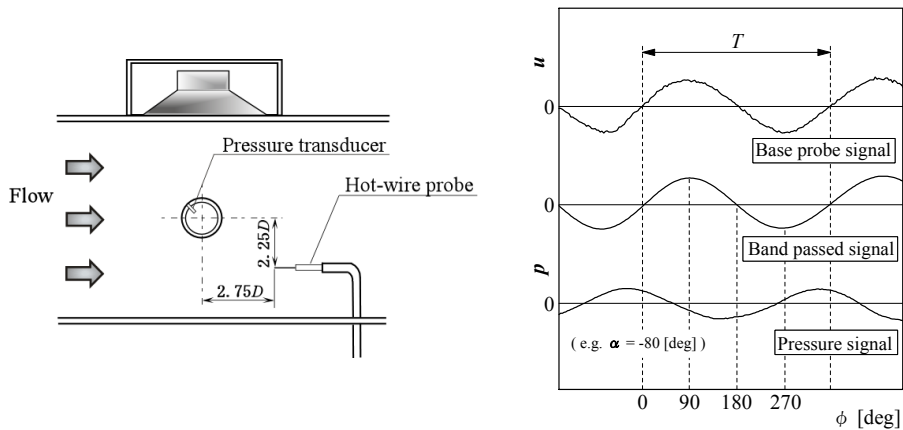


Fig.7 Conditional sampling technique

The example of the distribution of the phase averaged surface pressure given by above method is shown in Fig. 8. Here, figure a) and b) represents a different phase angle situation, it needs an attention to the phase difference with the pressure signal because this phase angle is based on the velocity signal (see Fig. 7). Even though the disturbance hardly affects on the state that the fluctuating pressure is small (i.e. close to time-mean value), the pressure in the lower pressure side ($-160 < \alpha < -70$ deg in the right side figure) increases and decreases as compared with the non-excited case.

Finally, Fig. 9 shows the coefficient of the drag and lift force calculated from the surface pressure distribution in each phase angle. Also, Table 1 shows the standard deviation of all phase angles data in each condition (i.e. the fluctuating drag and lift coefficient in the narrow meaning). It is found that the acoustic disturbance acts upon the fluctuating force and especially brings about 15 to 20% changes of the fluctuating lift force compared with the non-excited case. Furthermore, it is expected that these acoustic excitations affect on the formation of the Karnam vortex, which is a primary vortex.

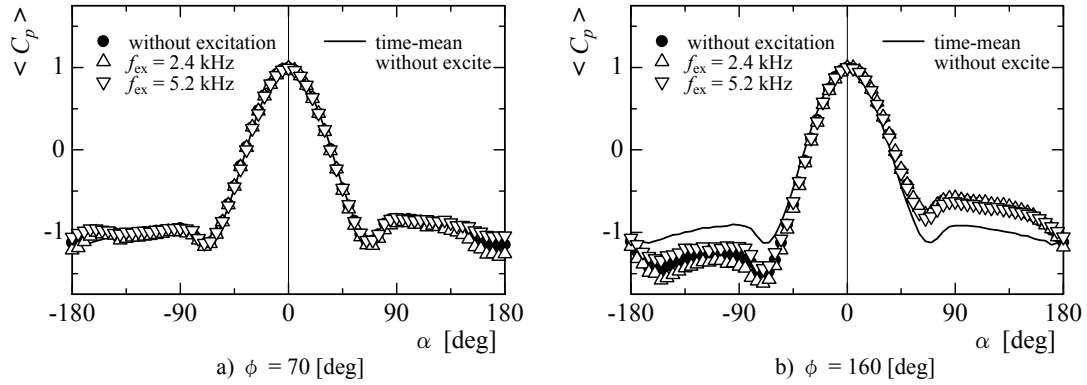


Fig.8 Phase averaged pressure distributions

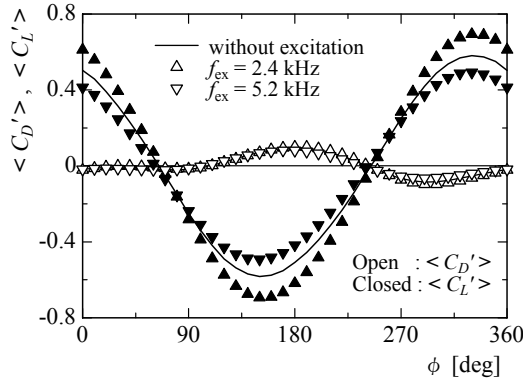


Fig.9 Variations of fluctuating drag and lift force

Table 1 Coefficients of fluctuating drag and lift force

	$\sigma_{\langle C_D' \rangle}$	$\sigma_{\langle C_L' \rangle}$
Without excitation	0.0548	0.414
$f_{ex} = 2.4$ kHz	0.0594	0.496
$f_{ex} = 5.2$ kHz	0.0456	0.350

4. CONCLUSIONS

In respect to the flow around a circular cylinder with periodic disturbance, mean and fluctuating pressure on the cylinder surface were measured and the following conclusions were obtained.

- [1] The pressure on the cylinder surface changes when the acoustic excitation with particular frequencies was imposed and the time-mean drag force increases and decreases according to the frequency. Its frequency agrees with that of the transition wave, which appears in the separated shear layer.
- [2] The influence of the periodic disturbance can be detected clearly on the fluctuating pressure and the frequency component of Karman vortex shedding is more affected at the top and bottom section of the cylinder.
- [3] The acoustic excitation is able to control the fluctuating forces associated with the vortex shedding and it brings about 20% of changes as for the fluctuating lift force.

REFERENCES

- [1] Hsiao, F.B. et al.: Experimental study of an acoustically excited flow over a circular cylinder, *Transport Phenomena in Thermal Control* (ed. G.J. Hwang), New York, 1989, Hemisphere, 537-546.
- [2] Hsiao, F.B. and Shyu, J.Y.: Influence of internal acoustic excitation upon flow passing a circular cylinder, *Journal of Fluids and Structures*, 1991, **5**, 427-442.
- [3] Peterka, J.A. and Richardson, P.D.: Effect of sound on separated flows, *J. Fluid Mech.*, 1969, **37**(2), 265-287.
- [4] Sheridan, J. et al.: The Kelvin-Helmholtz instability of the separated shear layer from a circular cylinder, *Proc. of IUTAM Symp. on Bluff-Body Wakes, Dynamics and Instabilities* (ed. H. Eckelmann et al.), Berlin, 1992: Springer-Verlag, 115-118
- [5] Zobnin, A.B. and Sushchik, M.M.: Influence of a high-frequency sound field on vortex generation in the wake of a cylinder, *Sov. Phys. Acoust.*, 1989, **35**(1), Jan.-Feb., 37-39.
- [6] Bloor, M.S.: The transition to turbulence in the wake of a circular cylinder, *J. Fluid Mech.*, 1964, **19**, 290-304.
- [7] Wei, T. and Smith, C.R.: Secondary vortices in the wake of circular cylinders, *J. Fluid Mech.*, 1986, **169**, 513-533.

RESPONSE OF NEAR-WALL STRUCTURE TO TIME-PERIODIC BLOWING IN A TURBULENT BOUNDARY LAYER

K. Kim and H. J. Sung

Department of Engineering Mechanics, Korea Advanced Institute of Science and Technology,
373-1, Guseong-dong, Yusong-gu, Daejeon, 305-701, Korea

ABSTRACT: Direct numerical simulations are performed to see the effects of time-periodic blowing frequency from a spanwise slot on a turbulent boundary layer. The time-periodic blowing frequency is given in a range $0 \leq f^+ (= f \nu / u_{\tau, in}^2) \leq 0.08$ at a fixed blowing amplitude of $A^+ = 0.5$. The effects of the blowing frequency are scrutinized by examining the phase- or time-averaged turbulent statistics. A most effective blowing frequency is obtained at $f^+ = 0.03$, where the maximum increases of Reynolds shear stress, streamwise vorticity fluctuations and energy redistribution are made. The phase-averaged stretching and tilting terms are studied for analyzing the increase of streamwise vorticity fluctuations which is closely related to turbulent coherent structures.

1. INTRODUCTION

Advances in the understanding the coherent structure of wall-bounded turbulent flow have intensified interest in controlling the near-wall turbulence. Recent direct numerical simulations have demonstrated a successful active control over the entire wall^[1,2]. From a practical point of view, however, this active control over the entire wall is difficult to implement because it requires a dense population of sensors and actuators on the wall. Many attempts have been made to devise a practical method for controlling wall bounded flows. Among the approaches considered to date, the use of local suction/blowing^[3,4] deserves more detailed study because it provides an efficient and simple means for locally actuating the wall-bounded flow. Moreover, the strength of the actuation can be controlled with relative ease by local suction/blowing.

Most previous experimental and numerical studies of local suction/blowing have focused on steady actuation^[5,6,7,8]. It is reported that the local steady blowing lifts up near-wall streamwise vortices, thereby reducing the interaction of the vortices with the wall. The steady blowing leads to a reduction in the skin friction near the wall, combined with an increase in the turbulent intensity and skin friction far downstream from the slot. In contrast to the previous studies that considered only steady blowing, a relatively few studies of unsteady suction/blowing were made experimentally and numerically^[9,10,11,12]. Park *et al.*^[9] performed experiments to probe the effects of periodic blowing and suction through a spanwise slot on a turbulent boundary layer. The higher forcing frequency induces greater changes in the turbulent structures of boundary layer. It is known that the near-wall streamwise vortices play a dominant role on the wall bounded flows^[13], however, the responses of near-wall vortices to the unsteady periodic blowing were not studied in detail.

In the present study, the effect of the blowing frequency on turbulent boundary layer is investigated by carrying out DNS. Main emphasis of this study is placed on the blowing frequency effect on near-wall turbulent flow structures downstream of the spanwise slot. The Reynolds number based on the momentum thickness at inlet is $Re_\theta = 300$, and the slot width is approximately 100 wall units. The localized time-periodic blowing is given by changing the vertical velocity on the spanwise slot. The blowing frequency is in a range of $0 \leq f^+ \leq 0.08$ at a fixed blowing amplitude ($A^+ = 0.5$). The frequency responses are scrutinized by examining the phase- or time-averaged turbulent statistics. A most effective blowing frequency is observed at $f^+ = 0.03$, where the maximum increases of Reynolds shear stress, streamwise vorticity fluctuations and energy redistribution are made. The phase-averaged stretching and tilting terms are analyzed to clarify the increase of streamwise vorticity fluctuations.

2. COMPUTATIONAL DETAILS

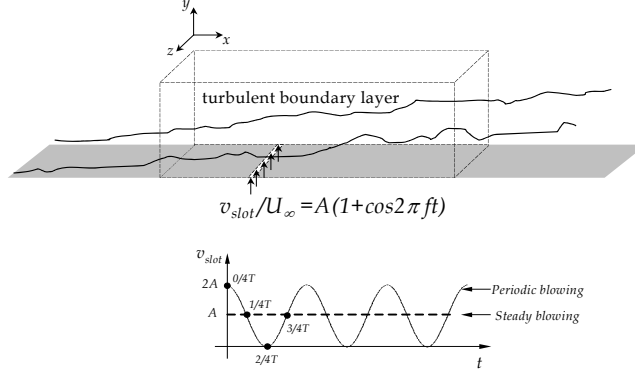


Fig. 1: Schematic diagram of the computational domain

The flow configuration, boundary conditions and other numerical procedures are summarized in the following. As shown in Fig. 1, the domain size is $200\theta_{in} \times 30\theta_{in} \times 40\theta_{in}$ in the streamwise, wall-normal and spanwise directions, where the corresponding mesh size is $257 \times 65 \times 129$. The mesh is uniform in the streamwise and spanwise directions, but a hyperbolic tangent stretching is used in the normal direction to cluster points near the wall. The mesh resolutions are $\Delta x^+ \approx 12.40$, $\Delta y_{min}^+ \approx 0.17$, $\Delta y_{max}^+ \approx 23.86$, and $\Delta z^+ \approx 4.96$, based on the friction velocity at the inlet. For DNS of spatially developing turbulent boundary layer with zero pressure gradient, realistic velocity fluctuations at the inlet are obtained using the method of Lund *et al.*^[14]. The convective outflow condition $(\partial u_i / \partial t) + c(\partial u_i / \partial x) = 0$ is used at the exit, where c is taken to be the mean exit velocity. A no-slip boundary condition is imposed at the solid wall. At the free-stream, the conditions $u = U_\infty$ and $\partial v / \partial y = \partial w / \partial y = 0$ are imposed. Periodic boundary conditions are used in the spanwise direction. The spanwise slot for periodic blowing extends from $x = 75.8\theta_{in}$ to $x = 82.0\theta_{in}$, where the location of the inlet is defined as $x = 0$. The slot width is $b^+ \approx 100$ in wall units. The periodic blowing at the slot is generated by varying the wall-normal velocity according to the equation:

$$v_{slot} / U_\infty = A(1 + \cos 2\pi f t) \quad (1)$$

The maximum blowing velocity ($v_{slot} / U_\infty = 2A$) is imparted at $t = 0/4T$ and the minimum ($v_{slot} = 0$) at $t = 2/4T$, where T is the blowing period. At $t = 1/4T$ and $3/4T$, the blowing velocities are the same as that of steady blowing with decelerating and accelerating phase, respectively. The amplitude of periodic blowing is $A^+ = 0.5$ in wall unit, which corresponds to the value of v_{rms} at $y^+ = 15$ without blowing. The blowing frequency ($f^+ = f\nu / u_{\tau, in}^2$) varies in a range $0 \leq f^+ \leq 0.08$, where $u_{\tau, in}$ is the friction velocity at the inlet and ν is the kinematic viscosity. The governing Navier-Stokes and continuity equations are integrated in time by using a fractional step method with an implicit velocity decoupling procedure^[15]. A second-order central difference scheme is used in space with a staggered mesh. The Reynolds number based on the momentum thickness at the inlet is $Re_\theta = 300$. The computation time step is $\Delta t U_\infty / \theta_{in} = 0.3$, which corresponds to $\Delta t^+ \approx 0.25$ in wall units. The total time over which statistical averages are calculated is $T_{avg} = 18000\theta_{in} / U_\infty$, which corresponds to 150, 460 and 1250 periods for $f^+ = 0.01$, 0.03 and 0.08, respectively. The imposition of periodic blowing may lead to periodic variations in the global physical quantities of the flow. Hence, it is necessary to represent each flow quantity as a superposition of three components

$$q(x, y, z, t) = \bar{q}(x, y) + \tilde{q}(x, y, t) + q''(x, y, z, t), \quad (2)$$

where the instantaneous quantity q is decomposed into a time-mean component \bar{q} , an oscillating component \tilde{q} and a random fluctuating component q'' .

3. RESULTS AND DISCUSSION

It is important to find the energy redistribution by the present unsteady blowing. The relative increase of turbulent intensity is defined as $\Delta\eta(\%) = (\eta_{max} - \eta_{max,o}) / \eta_{max,o} \times 100$, where the subscript "o" denotes no

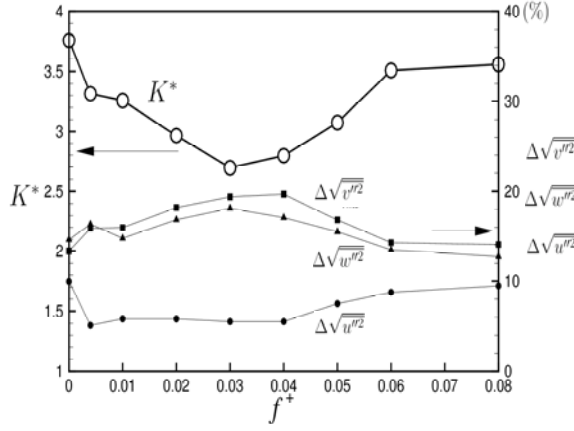
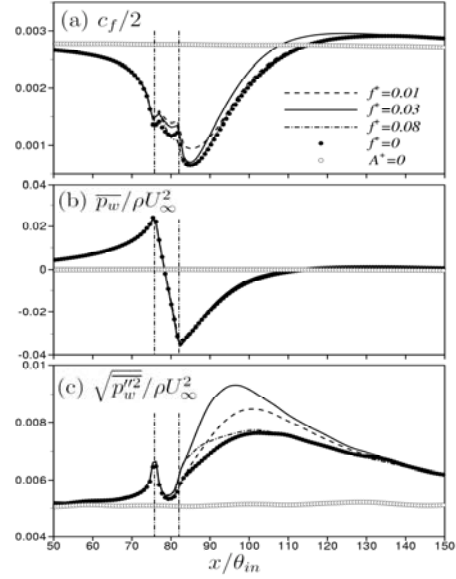


Fig. 2: Relative increases of turbulent intensities and the energy partition parameter K^* (Above)

Fig. 3: Time-averaged values of (a) skin friction coefficient, (b) wall pressure, (c) wall pressure fluctuations. (Right)



blowing. As displayed in Fig. 2, the increases of cross-stream components $\Delta v''_{rms}$ and $\Delta w''_{rms}$ are larger than that of streamwise component $\Delta u''_{rms}$. This means that the intercomponent energy transfer is enhanced by unsteady blowing. The behaviors of $\Delta v''_{rms}$ and $\Delta w''_{rms}$ indicate that they have a broad peak at around $f^+=0.03$. Next, to see the relative contribution to the turbulent kinetic energy of streamwise turbulent intensity and intensities normal to the mean flow, the energy partition parameter K^* is calculated, $K^*=2u''^2/(v''^2+w''^2)^{[16]}$. The parameter K^* is measured at which the increase of turbulent kinetic energy is maximum. It is obvious that K^* has a local minimum at $f^+=0.03$. The smaller value of K^* means that the energy redistribution is more active. However, as the blowing frequency increases further ($f^+=0.08$), K^* converges to that of $f^+=0$. This suggests that the flow is not sensitive to the higher frequency blowing.

Figure 3 shows the streamwise distributions of time-averaged skin friction c_f , wall pressure \bar{p}_w and rms of wall pressure fluctuations $p''_{w,rms}$. Three cases of the blowing frequency ($f^+=0.01, 0.03$ and 0.08) are chosen to distinguish the flow structures by unsteady blowing. The effective blowing frequency is chosen at $f^+=0.03$, which gives the minimum value of K^* . The lower and higher blowing frequencies are chosen at $f^+=0.01$ and $f^+=0.08$, respectively. $f^+=0$ corresponds to 'steady blowing' and $A^+=0$ is 'no blowing'. For all blowing cases in Fig. 3(a), c_f decreases rapidly near the slot and increases in the downstream. It is seen that the recovery of c_f at $f^+=0.03$ is faster than other two blowing cases. However, the variations of wall pressure \bar{p}_w in Fig. 3(b) are almost the same regardless of the blowing frequency. The adverse pressure gradient appears ahead and behind the slot, whereas the favorable pressure gradient occurs above the slot. As shown in Fig. 3(c), the wall pressure fluctuations $p''_{w,rms}$ are very sensitive to the effective blowing frequency ($f^+=0.03$).

Profiles of the time-averaged rms velocity fluctuations and Reynolds shear stress are shown in Fig. 4. The velocity fluctuations and Reynolds shear stress for blowing are increased downstream of the slot compared with the case of 'no blowing'. The maximum increase of u''_{rms} is located at around $x/\theta_{in}=100$. However, the maximum increases of v''_{rms} , w''_{rms} and $-u''v''$ are located in the farther downstream ($x/\theta_{in}=110$). It is interesting to find that the increase of u''_{rms} for $f^+=0.03$ is smaller than those for other frequencies, whereas the increases of v''_{rms} , w''_{rms} and $-u''v''$ for $f^+=0.03$ are larger than those for other frequencies. This suggests that $f^+=0.03$ is the most effective blowing frequency in promoting the energy redistribution. Park *et al.*^[9] reported that the transverse fluctuating components are more susceptible to disturbances than the streamwise component. On the other hand, the time-averaged turbulent intensities appear to be insensitive to the higher blowing frequency ($f^+=0.08$).

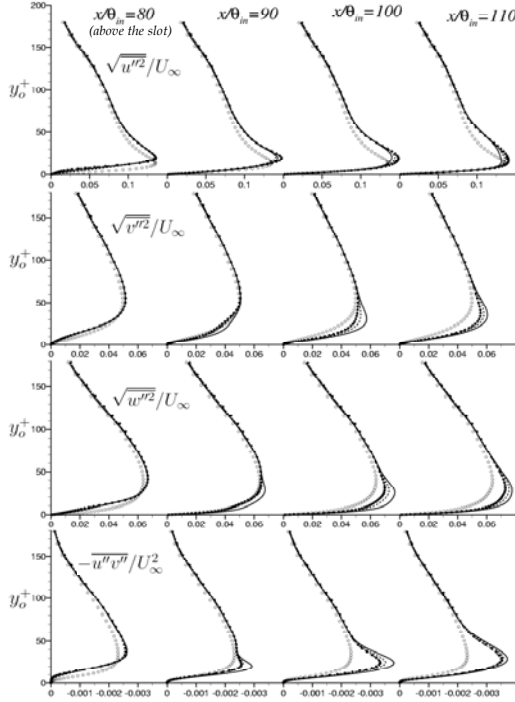


Fig. 4: Time-averaged turbulent intensities and Reynolds shear stress. -- $f^+=0.01$; — $f^+=0.03$; - · - $f^+=0.08$; • $f^+=0$; ○ $A^+=0$

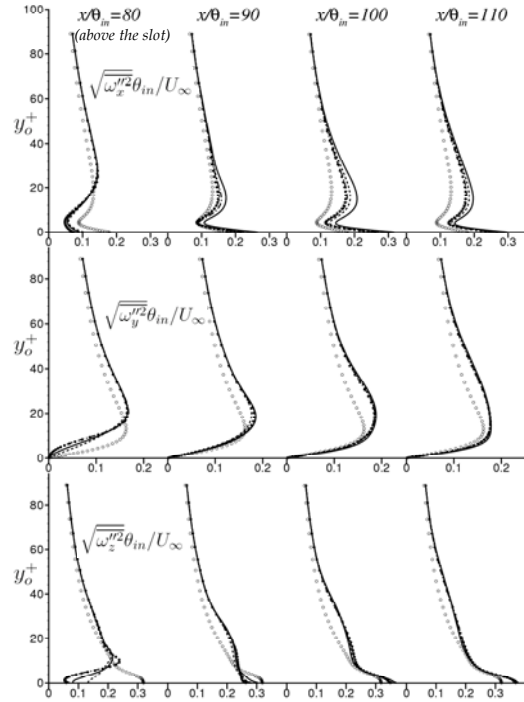


Fig. 5: Root time-mean square of vorticity fluctuations. -- $f^+=0.01$; — $f^+=0.03$; - · - $f^+=0.08$; • $f^+=0$; ○ $A^+=0$

Figure 5 shows the time-averaged rms vorticity fluctuations ($\omega_i''_{rms}$). All components of the vorticity fluctuations ($\omega_x''_{rms}$, $\omega_y''_{rms}$ and $\omega_z''_{rms}$) are enhanced downstream of the slot by periodic blowing. A closer examination of Fig. 5 indicates that $\omega_y''_{rms}$ and $\omega_z''_{rms}$ are enhanced by blowing regardless of the blowing frequency. However, $\omega_x''_{rms}$ is most enhanced at a particular blowing frequency ($f^+=0.03$). Accordingly, the most effective blowing frequency is $f^+=0.03$, at which the near-wall vortical structure is most activated. It is known that the location of local maximum of $\omega_x''_{rms}$ corresponds to that of the center of the streamwise vortex in the wall region^[17]. Recall that the maximum increases of wall pressure fluctuations and Reynolds shear stress are observed at $f^+=0.03$ (Figs. 3 and 4).

To see the effect of blowing on ω_x , the dynamic equation of ω_x^2 is derived^[6].

$$\frac{1}{2} \frac{d\omega_x^2}{dt} = \omega_x \omega_x \frac{\partial \omega_x}{\partial x} + \omega_x \left(\omega_y \frac{\partial u}{\partial y} + \omega_z \frac{\partial u}{\partial z} \right) + \omega_x \frac{1}{Re} \nabla^2 \omega_x \quad (3)$$

The first term of the right-hand side stands for the stretching (S), the second term for the tilting (T), and the last term for the diffusion (D), respectively. Contours of the phase-averaged stretching $\langle S \rangle - S_o$, tilting $\langle T \rangle - T_o$ and diffusion $\langle D \rangle - D_o$ are displayed in Fig. 6 for three blowing frequencies. Positive and negative values of the stretching and tilting denote, respectively, increase and decrease of their strengths, as compared to those in the case of no blowing. However, positive and negative values of the diffusion stand for, respectively, decrease and increase of its strength, because D_o is negative except very near the wall. The strength of each term significantly grows over downstream and their sum is also increased for three blowing frequencies, as compared to the case of 'no blowing'. This is consistent with the increase of $\omega_x''_{rms}$ in Fig. 5. For $f^+=0.01$ (Fig. 6a), the strengths of $\langle S \rangle$, $\langle T \rangle$ and $\langle D \rangle$ are weak on the slot at the phase of maximum blowing velocity ($t=0/4T$). However, they are strong at the immediate rear of the slot. As time goes by, $\langle S \rangle$, $\langle T \rangle$ and $\langle D \rangle$ are getting stronger and convect downstream. Their sum, which denotes the rate change of $\langle \omega_x^2 \rangle$, begins to increase near the slot at the maximum blowing phase and becomes

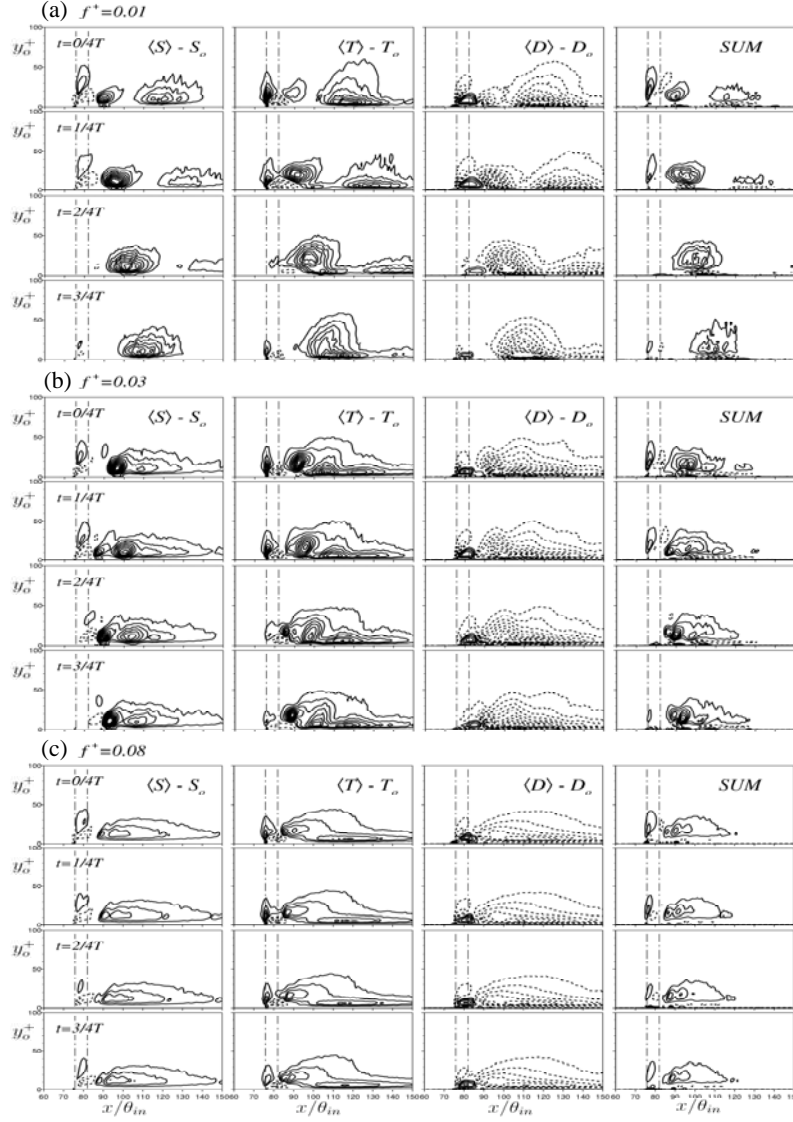


Fig. 6: Contours of phase-averaged stretching, tilting, diffusion and their sum; (a) $f^+ = 0.01$, (b) $f^+ = 0.03$, (c) $f^+ = 0.08$. Contour levels range from $-0.002 U_\infty^3 / \theta^3$ to $0.002 U_\infty^3 / \theta^3$.

stronger as it convects downstream. When the effective blowing frequency is given at $f^+ = 0.03$ (Fig. 6b), the stretching and tilting begin to increase at different blowing phase, i.e., stretching starts to increase at $t = 1/4T$, whereas tilting at $t = 2/4T$. Thus, the increases of stretching and tilting occur alternately in the downstream. As a result, the region of $SUM > 0$ is widely distributed over downstream during one period. This gives the maximum increase of $\omega_{x''rms}$ at $f^+ = 0.03$ in Fig. 5. For $f^+ = 0.08$ (Fig. 6c), the contours are almost the same regardless of the phase change and are similar to those of steady blowing^[6].

4. CONCLUSIONS

Detailed numerical analysis has been performed to see the effect of blowing frequency on a turbulent boundary layer. The slot width is $b^+ \approx 100$ in wall units and the blowing frequency varies in a range $0 \leq f^+ \leq 0.08$ with a fixed blowing amplitude ($A^+ = 0.5$). An effective blowing frequency is observed at

$f^+=0.03$, which gives the minimum value of K^* . The time-averaged wall pressure is invariant with the blowing frequency. However, the time-averaged skin friction and rms of wall pressure fluctuations are sensitive to the blowing frequency. Furthermore, the recovery of c_f is fast at $f^+=0.03$. The increase of u''_{rms} for $f^+=0.03$ is smaller than those for other frequencies, whereas the increases of v''_{rms} , w''_{rms} and $-u''v''$ for $f^+=0.03$ are larger than those for other frequencies. The time-averaged streamwise vorticity fluctuations $\omega_x''_{rms}$ is most enhanced at $f^+=0.03$, which activates the near-wall vortical structures. From the dynamic equation of ω_x^2 , the responses of stretching and tilting to the blowing frequency are analyzed. When the effective blowing frequency is given at $f^+=0.03$, stretching and tilting begin to increase at different blowing phase. The increases of stretching and tilting occur alternately in the downstream.

ACKNOWLEDGMENTS

This research was supported by a grant from the National Research Laboratory of the Ministry of Science and Technology, Republic of Korea.

REFERENCES

- [1] Choi H, Moin P and Kim J: Active turbulence control for drag reduction in wall-bounded flows. *J Fluid Mech.*, 1994, **262**, 75-110
- [2] Hammond EP, Bewley T R and Moin P: Observed mechanisms for turbulence attenuation and enhancement in opposition-controlled wall-bounded flows. *Phys. Fluids*, 1998, **10** (9), 2421-2423
- [3] Rebbeck H and Choi K-S: Opposition control of near-wall turbulence with a piston-type actuator. *Phys. Fluids*, 2001, **13**(8), 265-268
- [4] Jacobson SA and Reynolds WC: Active control of streamwise vortices and streaks in boundary layers. *J Fluid Mech.*, 1998, **360**, 179-211
- [5] Sano M and Hirayama N: Turbulent boundary layers with injection and suction through a slit. First report : Mean and turbulence characteristics. *Bull. J. Soc. Mech. Eng.*, 1985, **28** (239), 807-814
- [6] Park J and Choi H: Effects of uniform blowing or suction from a spanwise slot on a turbulent boundary layer flow. *Phys Fluids*, 1999, **11** (10), 3095-3105
- [7] Krogstad PÅ and Kourakine A: Some effects of localized injection on the turbulence structure in a boundary layer. *Phys Fluids*, 2000, **12** (11), 2990-2999
- [8] Kim K, Sung HJ and Chung MK: Assessment of local blowing and suction in a turbulent boundary layer. *AIAA J.*, 2002, **40** (1), 175-177
- [9] Park S-H, Lee I and Sung HJ: Effect of local forcing from a spanwise slot on a turbulent boundary layer. *Exp. Fluids*, 2001, **31**, 384-393
- [10] Rhee GH and Sung HJ: Numerical prediction of locally-forced turbulent boundary layer. *Int J Heat Fluid Flow*, 2002, **22** (6), 624-632
- [11] Park YS, Park S-H and Sung HJ: Measurement of Local Forcing on a Turbulent Boundary Layer Using PIV. *Exp. Fluids*, 2003, **34** (6), 697-707
- [12] Tardu SF: Active control for near-wall turbulence by local oscillating blowing. *J Fluid Mech.*, 2001, **439**, 217-253
- [13] Robinson SK: Coherent motions in the turbulent boundary layer. *Ann Rev Fluid Mech.*, 1991, **23**, 601-639
- [14] Lund TS, Wu X, and Squires KD: Generation of turbulent inflow data for spatially-developing boundary layer simulation. *J Comput Phys.*, 1998, **140**, 233-258
- [15] Kim K, Baek S-J, and Sung HJ: An implicit velocity decoupling procedure for the incompressible Navier-Stokes equations. *Int J Numer Methd Fluids*, 2002, **38** (2), 125-138
- [16] Neves JC, Moin P, and Moser RD: Effects of convex transverse curvature on wall-bounded turbulence. Part 1: Time velocity and vorticity. *J Fluid Mech.*, 1994, **272**, 349-381
- [17] Kim J, Moin P, and Moser R: Turbulence statistics in fully developed channel flow a low Reynolds number. *J Fluid Mech.*, 1987, **177**, 133-166

UNSTEADY PIPE FLOW TRANSITION TO TURBULENCE UNDER CONSTANT ACCELERATION

U. Liiv

Institute of Mechanics, Tallinn Technical University, Akadeemia tee 21, 12611 Tallinn, Estonia

ABSTRACT: Unsteady pipe flow from the rest with different values of constant acceleration has been observed. CTA and LDA apparatus have been used for investigation of the shear on the wall and 2D velocity distributions. Experiments indicate that in case of laminar-turbulent transition even under moderate accelerations the instantaneous Reynolds number Re_i exceeds quasi-steady flow Re_s more than two orders. Instabilities before transition are generated inside Tollmien-Schlichting waves. Dependence of the thickness of the Stokes layer from the instantaneous transition Reynolds number Re_t is presented.

1. INTRODUCTION

Unsteady flows in pipes are always encoupled with considerable local inertia forces depending on the values of acceleration of the flow. Due to the values of these local inertia forces all hydrodynamic quantities are not the same as those in steady flows. Early experimental investigations [1] on accelerating pipe flows unsteady friction factor indicates that the wall turbulence is generated at instantaneous Re_t until 2.5×10^5 depending on the value of acceleration. Experiments of the unsteady 2D flow field [2] carried out in Laboratory Hydrodynamics of the Tallinn Technical University show that turbulence is generated in a thin layer near the wall. Before turbulence generation, unsteady flow is characterized with uniform velocity distributions with gradients in a thin layer near the wall. Laminar-turbulent transition is caused by the instabilities inside Tollmien - Schlichting waves on the wall growing by the time. After the flow loses stability near the wall turbulence spreads rapidly over the cross - section of the flow. Turbulent quantities generated during the unsteady flow period obtain the values of the steady flow quantities after a long period of many times exceeding the regulation time of the valve.

Among large number unsteady transient phenomena investigations starting with the publications of Carstens [3] and Hino et al. [4] studying oscillatory pipe flow first established dependence of transient Stokes parameter from Re_t .

The results of the measurements of turbulence generated by instabilities and its spreading over the cross section are presented below.

2. EXPERIMENTAL SET-UP AND APPARATUS

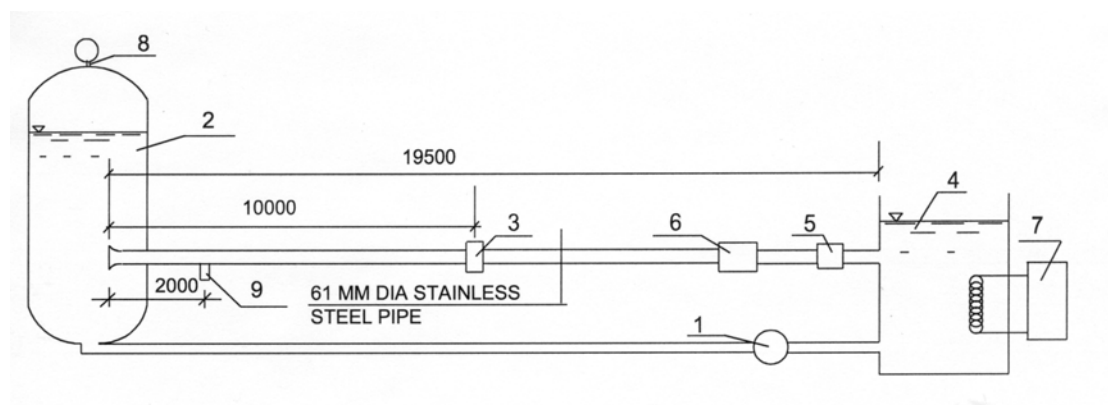


Fig. 1: Experimental hydraulic system

Experiments were carried out in the laboratory on a hydraulic system designed for the unsteady flow investigations. The closed type system (Fig.1) consists of the following parts: 1- pump, 2- upper tank, 3- test section, 4-lower tank, 5-quick opening valve, 6- magnetic flow meter designed for unsteady flow measurements,

7- cooling system, 8- upper tank pressure control system, 9- pressure transducer. Steady flow investigations indicate that the pipe friction confirms to the smooth pipe law until $Re = 3.0 \times 10^5$.

Before each test run the upper tank (2) was pressurised using pump (1) in the closed circuit system until certain level inside upper tank (2) was established. The pump was switched off and the system was left to rest for a while until the fluctuations had calmed down. The experiment was initiated by opening the valve (5). During the whole test run the pressure in the upper tank was kept constant with control system (8) by pressurising the air above the water. The cooling system (7) is keeping the temperature of the water in hydraulic system at $t = 18^\circ \text{C} \pm 0.5^\circ$. This facilitates the calculation with Constant Temperature Anemometer measurements, but also keeps constant the value of the viscosity coefficient, which is important because during the long testing sessions in closed contour the water temperature increases. Two different diameters 0.061 m and 0.033 m stainless steel pipes has been used.

Each run with the same initial conditions was repeated not less than 300 times to create data for ensemble averaging and statistical calculations of different hydrodynamic quantities.

Two different series of experiments have been provided:

1. wall shear measurements using flush mounted type 55R46 sensors together with measuring equipment 55M01
2. 2D velocity characteristics using a Tracker based 2 Channel LDA apparatus 55N01.

Both apparatus used are manufactured by DANTEC;

A special device was designed to establish the flush mounted CTA sensor through the wall of the pipe allowing to clamp the device and establish the sensitive element inside the viscous sub layer near the wall (Fig.

2). The calculated value of the coordinate of the sensitive film element was $y^+ = yu_* / \nu = 6$.



Fig. 2: Device to clamp flush mounted 55R46 CTA sensor

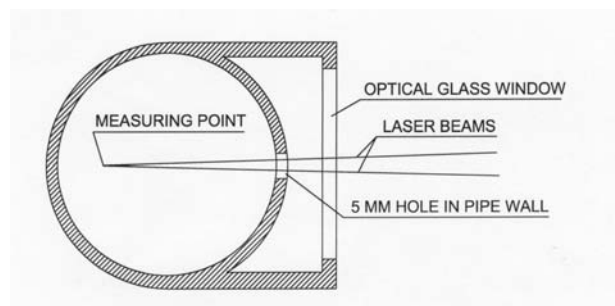


Fig.3: Cross section of the velocity measurements section

Another technical problem raised when measuring velocities inside the pipe was due to uneven refraction of the laser beams through the round surface of the pipe. A special section was established consisting of a plane optical glass window and a hole in pipe wall (Fig. 3). Assuming the axisymmetric flow, the velocities were measured at the opposite side of the hole.

Experimental data has been recorded on-line in a computer with frequency of 1.5 kHz per channel.

3. EXPERIMENTAL RESULTS AND DISCUSSION

Based on the CTA measurements on the above described experimental set-up already in 1977 the values of friction coefficient f at different values of accelerated from rest pipe flow have been published [1,2]. The results of one of the unsteady runs of that investigation is presented on Fig. 4. Analysing the experimental data of the

measured friction velocities u_* we see that fluctuations are not observed until a rapid increase of the friction velocity u_* occurs.

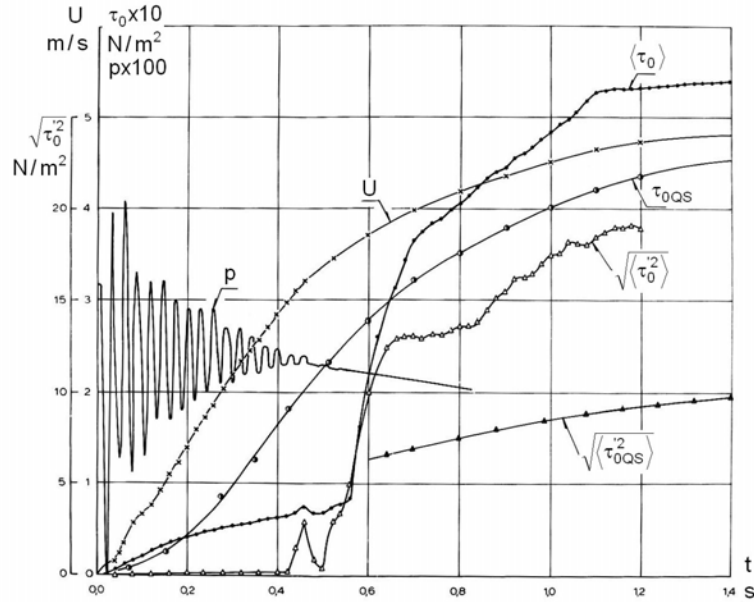


Fig.4: Comparison of the measured unsteady and calculated quasi steady quantities

A comparison of the measured wall shear stresses $\langle \tau_0 \rangle$ and shear intensities $\sqrt{\tau_0'^2}$ calculated on the basis of measured instantaneous mean velocity U , and quasi-steady quantities τ_{0QS} and $\sqrt{\tau_{0QS}'^2}$ are presented in Fig. 4. The pressure recordings p are also presented.

The results indicate that during the starting phases of the flow before first burst of the turbulent intensities arise, shear stress on the wall of the pipe is less than that for quasi-steady case, but then at time moment $t=0.5$ s it increases rapidly. At the same time also i.e. when turbulent fluctuations are generated $\langle \tau_0 \rangle$ increases suddenly and at time moment 1.2 s quasi-steady values exceed steady ones by 20%. Data presented clearly shows that at the time moment when mean velocity has obtained 90% of the final value, the measured quantities of unsteady shear stresses and turbulent intensities are much higher than those for the corresponding quasi-steady values. From that the first conclusion can be made: even when the mean acceleration rate becomes zero, additional time is necessary to get down with the turbulent quantities.

On the ground of the 2D velocity measurements at 16 different points of the pipe radius over the cross section of the 0.061 m pipe axial component of velocity distributions u_z at different time moments are presented in Fig. 5. The measurements show that until turbulence is generated near the wall uniform axial velocity distribution exists without any turbulence outside the wall area between values r/R 0.95 and 1.0. Radial velocity component measurements and flow visualisation indicate that transition occurs when Tollmien-Schlichting waves loose stability at instantaneous Reynolds number $Re_t = 1.8 \times 10^5$. First turbulence bursts appear in the area of dimensionless radius between 0.96-0.98. At the same time wall shear stress (Fig. 4) increases rapidly. Final steady flow axial velocity distribution with $Re = 3.0 \times 10^5$ is presented in Fig. 5 with circles.

On Fig.6, near wall area measurement results of the axial velocity between time moments 0.56 and 0.78 are presented i.e. time interval when transition from laminar to turbulence occurs. Data presented shows that high value of the intensity of the mass transfer in the area between dimensionless radius 0.95 and 0.85.

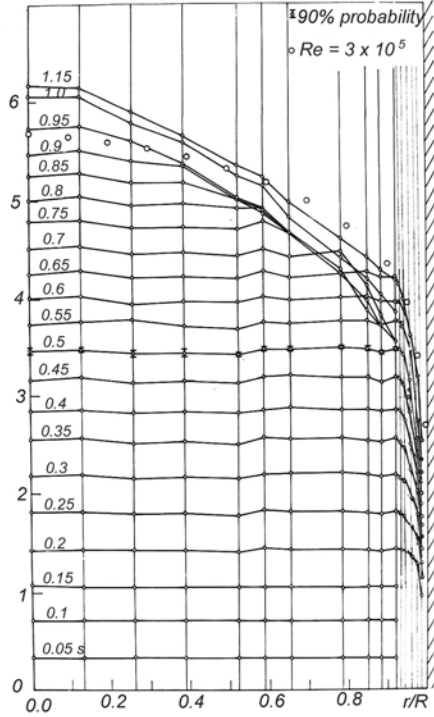


Fig.5: Axial velocity distribution at different time moments

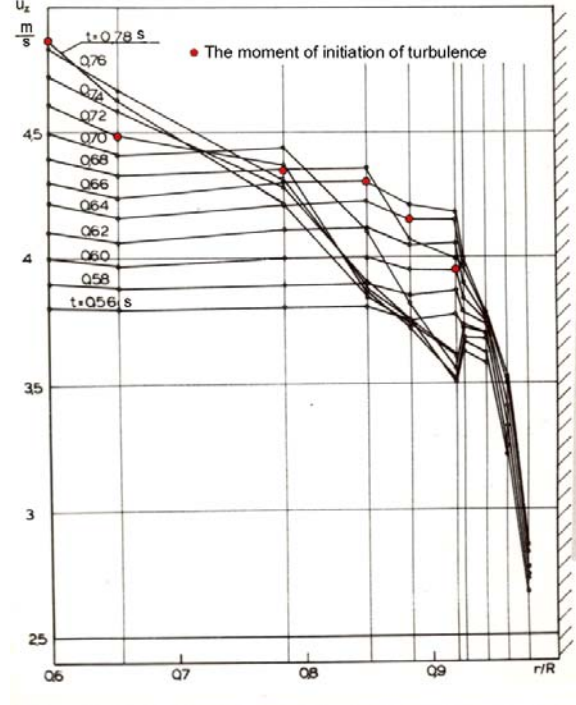


Fig. 6: Measured wall region axial velocities at transition moments

Vizualisation using high speed camera and measured 2D velocity field in the area allows to establish that the first turbulent bursts appearing near the wall with dimensionless coordinate r/R between 0.96 and 0.98. According to the measured data, turbulence is spreading simultaneously to the wall and to axis of the pipe generating on the wall a layer which is characterized with turbulent fluctuations. After passing the value of the maximum acceleration of the mean flow, turbulence is spreading rapidly over the whole cross section of the pipe.

Based on the measured velocities a turbulent mixing factor ξ dependance on dimensionless time $t - t_0 / \Delta t$ is presented on Fig.7 showing the speed of the turbulence spreading during the laminar-turbulent transition of the starting pipe flow.

Here t -corresponds to the turbulence generating at the point, t_0 -moment of turbulence generation on the wall and Δt - time of turbulence spreading from the wall to the axis of the pipe.

Oscillatory flow investigation by Hino et al. [4] established critical Re number of the transition using Stokes layer Reynolds number as

$$Re_{\delta} = U\delta_S / \nu \quad (1)$$

where U - velocity in Stokes layer, δ_S - Stokes layer thickness, ν -kinematic viscosity.

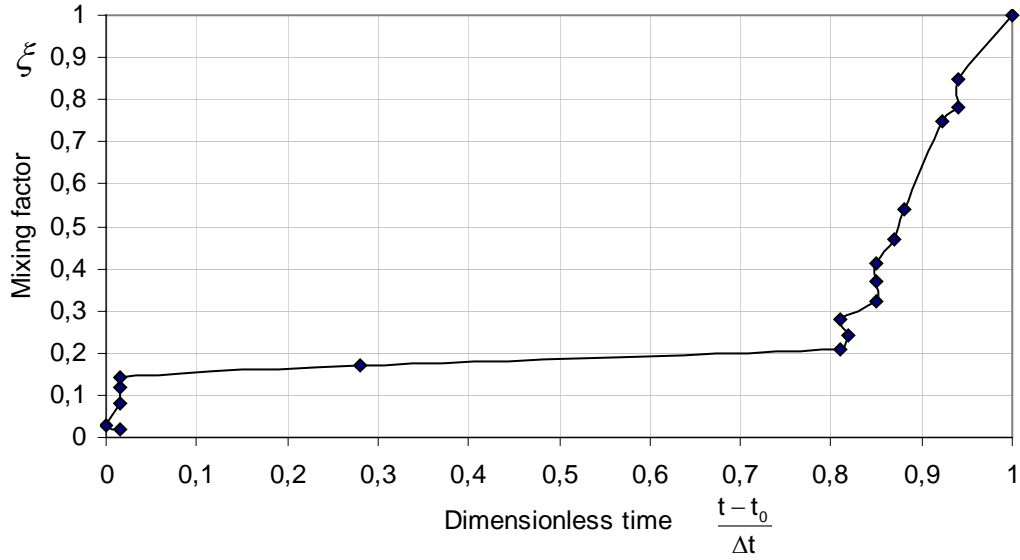


Fig. 7. Turbulence spreading over the cross section after stability loss in the wall region

According to [4] Stokes parameter was calculated as

$$\lambda_s = d / 2\delta, \quad (2)$$

and transient Reynolds number as

$$Re_t = U_t d / \nu \quad (3)$$

Analyzing the measured near wall velocities at starting pipe flow, we found the formula for the thickness of the dynamic boundary layer as

$$\delta_s = 3,3\sqrt{\nu t} \quad (4)$$

Using (2) and (4) we obtained

$$\lambda_s = d / 6,6\sqrt{\nu t} \quad (5)$$

where U_t is mean velocity at the transition moment, d - diameter of the pipe and t - time.

Data obtained from the experimental transient moment of the starting pipe flow for different rates of acceleration with pipe diameters 0.061 and 0.033 m and adding data from [5,6] with pipe diameters 0.050, 0.036, 0.025 and 0.012 m we got dependance between Stokes layer λ_s thickness and instantaneous transient Reynolds number Re_t . Results of these calculations are presented on Fig. 8. Obtained from [4] corresponding values and the dashed line with $Re_{\delta}=550$ describing the transition of the oscillatory flow are also presented. In comparison a line with $Re_{\delta}=5580$, describing transition of the pipe flow from the rest is presented with solid line.

4. DISCUSSION AND CONCLUSIONS

1. Earlier investigations show that laminar-turbulent transitions in starting pipe flow occurs at instantaneous Reynolds number prevailing steady flow Reynolds number until more than two orders.
2. During starting pipe flow transition a turbulent layer is generated on the wall.
3. Turbulence spreading of the over the cross section depends on the value of acceleration.
4. Dependence of Stokes layer thickness from transient Reynolds number Re_t is presented.

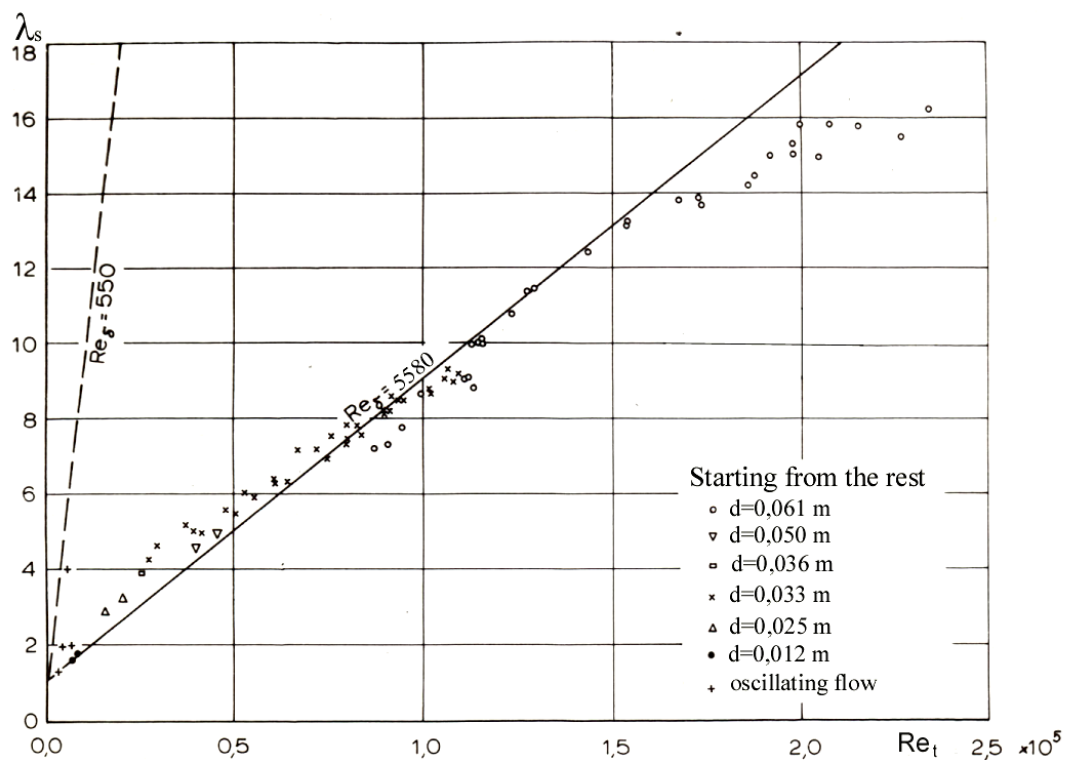


Fig.8. Stokes layer thickness at the moment of transition

ACKNOWLEDGEMENTS

This work is partly funded from the sources of Estonian Science Foundation Grant G4855. Hereby the author wishes to thank his colleagues whose contribution was irreplaceable in carrying out the above discussed experiments.

REFERENCES

- [1] Koppel T., Liiv U. An Experimental Investigation of the Starting Pipe Flow, *Proc. Acad. Sci. USSR, Fluid and Gas Mech.*, 1977, **6**, 79-85. (In Russian)
- [2] Liiv U. Using CTA and LDA Techniques in Unsteady Pipe Flow Investigations, *Proc. XXX IAHR Congress, Theme D*, 2003. *Thessaloniki Greece*, 441-448
- [3] Carstens M.R. Transition from Laminar to Turbulent Flow in Pipe, *J. Hydr. Div. ASCE*, 1957, *Vol. 83 No HY6*, 1450/1-1459/30
- [4] Hino M., Savamoto M., Takasu S. Experiments of Transition to Turbulence in an Oscillatory Pipe Flow, *J. Fluid Mech.*, 1976, **75**, part 2, 193-207
- [5] Letelier L.M.F., Leutheusser H.J., Skin Friction in Unsteady Laminar Pipe Flow *J. Hydr. Div. Proc. ASCE*, 1976, **102**, No. 1, 41-56
- [6] H.J. Leutheusser, K.W. Lam, Laminar to Turbulent Transition in Accelerated Fluid Motion, *Proc. XVII th Congr. IAHR, Germany*, 1977, *vol. 2*, 343-350

DEVELOPMENT OF SUBHARMONIC SINUOUS MODE IN LOW-SPEED STREAKS

Yasufumi Konishi and Masahito Asai

Department of Aerospace Engineering, Tokyo Metropolitan Institute of Technology, Tokyo, Japan

ABSTRACT: The nonlinear development of streak instability modes is examined up to the turbulent stage experimentally through artificially producing spanwise-periodic low-speed streaks in a flat plate laminar boundary layer. The experiment is focused on the subharmonic sinuous mode of the streak instability. The sinusoidal motion of low-speed streaks caused by the streak instability continues three or four wavelengths downstream beyond the nonlinear saturation stage, and subsequently breaks down into smaller-scale vortices. After the breakdown, near-wall low-speed streaks with lateral spacing of 100 wall units newly develop, and the mean velocity profile starts to exhibit the log-law. It is also found that the interaction between the quasi-streamwise vortices developing along the neighboring streaks causes large-scale arch-like vortices to develop in the region away from the wall.

I. INTRODUCTION

Recent direct numerical simulations on the wall turbulence strongly suggest that the instability of low-speed streaks is a key mechanism by which near-wall turbulence structures are generated and sustained^[1-6]. Inflectional velocity profiles across each low-speed streak in the normal-to-wall and spanwise directions are generally unstable. So the instability of such velocity profiles can lead to the breakdown of the streak shear layers into coherent quasi-streamwise vortices though the viscous diffusion effect operates to suppress the progress of the instability.

The development and breakdown of low-speed streaks were also observed prior to the onset of wall turbulence in boundary layer transition. In the transition initially caused by Tollmien-Schlichting waves^[7], low-speed streaks appear in the late stage of the secondary high-frequency instability, while in the by-pass transition caused by high-intensity free-stream turbulence, the low-speed streaks are directly generated by free-stream turbulence at the initial stage of the transition. It was observed that when the low-speed streaks are intensified, they undergo oscillatory motions due to the streak instability leading to the subsequent breakdown into turbulent spots^[8].

To examine how the streak instability leads to the onset of wall turbulence in detail, it is important to realize laminar low-speed streaks initially as well as to introduce well-controlled artificial disturbances, as has been done in the previous studies^[9,10]. In the present experimental study on the evolution of streak instability, spanwise-periodic low-speed streaks are generated in a laminar boundary layer by using small pieces of screen set normal to the boundary-layer plate with an equal interval in the spanwise direction. In our previous stability experiment^[11], the linear instabilities to the fundamental and subharmonic sinuous modes were examined in detail for the periodic low-speed streaks of various spanwise intervals and the subharmonic sinuous modes were found to be more amplified than the fundamental sinuous modes unless the streak spacing is much larger than the streak width. So, in the present study on the nonlinear development of the streak instability, we focus on the development of the most amplified subharmonic sinuous mode.

II. EXPERIMENTAL SETUP AND PROCEDURE

The whole experiment is conducted in a low turbulence wind tunnel of open jet type. The wind tunnel has three damping screens spanning the diffuser and five damping screens and a honeycomb in the settling chamber of 1200×1200 mm in cross section. The area ratio of the contraction to the test section of 400×400 mm is 9. This facility is the same as that used in our previous experiment^[11]. As illustrated in Fig. 1, a boundary-layer plate, which is 10 mm thick and 1100 mm long, is set parallel to the

oncoming uniform flow in the test section. The free-stream velocity U_∞ is fixed at 4 m/s throughout the experiment. The free-stream turbulence is less than 0.1% of U_∞ . The periodic low-speed streaks are produced in the boundary layer by using small 40-mesh screens (wire-gauzes) set normal to the boundary-layer plate at a station 500mm downstream of the leading edge. Without the screen, Blasius boundary layer develops with the displacement thickness of about 2.5mm at the x -station 500mm downstream of the leading edge. The screens whose width and height are 6mm and 3mm respectively are set with an equal interval of 15mm in the spanwise direction. In order to excite the streak instability, well-controlled external disturbances are introduced into the laminar low-speed streaks by alternately sucking and blowing air through small holes. As explained below, we here focus on the sinuous mode. In order to excite a sinuous instability mode, holes of 2mm in diameter are drilled at locations at both edges of each screen, 13.5mm downstream of the screens, and are connected separately to two loudspeakers by vinyl hoses. The loudspeakers are driven with sine-wave signals which are 180deg out of phase.

A constant-temperature hot-wire anemometer is used to measure time-mean and fluctuation velocities in the streamwise direction, U and u . As for the coordinate system, x is the streamwise distance measured from the leading edge, y the normal-to-wall distance, and z the spanwise distance. The x -position of the screens, $x = 500\text{mm}$, is denoted by x_0 .

III. LOW-SPEED STREAKS DOWNSTREAM OF SCREENS

First let us show the laminar low-speed streaks artificially generated by using the screens. Figures. 2 and 3 illustrate the flow field downstream of the screens in terms of the mean velocity U/U_∞ and the r. m. s. value of u -fluctuation u'/U_∞ , in the x - z plane at $y = 3\text{mm}$ and in the cross-section at $x-x_0 = 60\text{mm}$ respectively. We see the development of the regularly aligned streaky structure with the spanwise spacing $\lambda = 15\text{mm}$, in the region below $y = 4\text{mm}$. The distinct low-speed streaks extend far downstream beyond $x-x_0 = 400\text{mm}$ though the velocity defect across each low-speed streak fills up gradually with x . The velocity profiles across each low-speed streak are unstable to varicose and sinuous modes. According to our previous results^[9-11], the growth of the varicose modes is very sensitive to the ratio of lateral width to thickness of the horizontal shear layer associated with the low-speed streaks, and they can not grow so largely for the present streak geometry. Indeed, Figure. 3 shows that the u' -distribution in y - z plane is no other than that of the sinuous instability mode. Such naturally-developing disturbances grow downstream, but u'/U_∞ is only 2% even at $x-x_0 = 400\text{mm}$. Thus the low-speed streaks remain laminar in the whole observation region up to $x-x_0 = 400\text{mm}$ owing to the low background (wind tunnel) turbulence. This enables us to examine the streak instability by means of artificial disturbances.

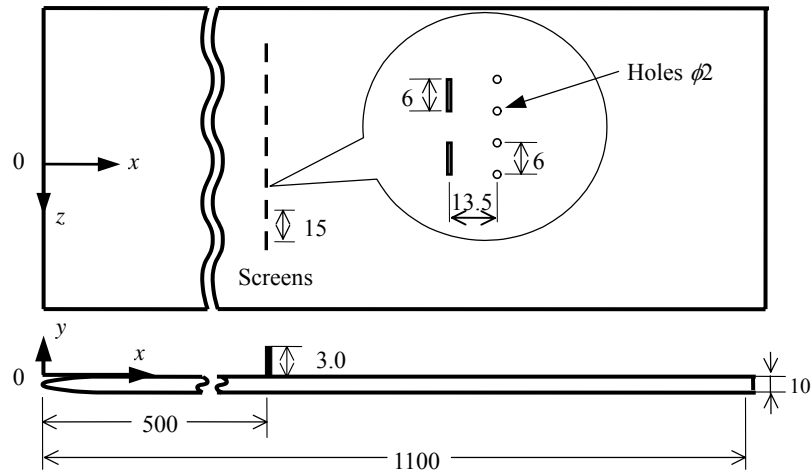


Fig. 1: Schematic of the experimental setup (dimensions in mm).

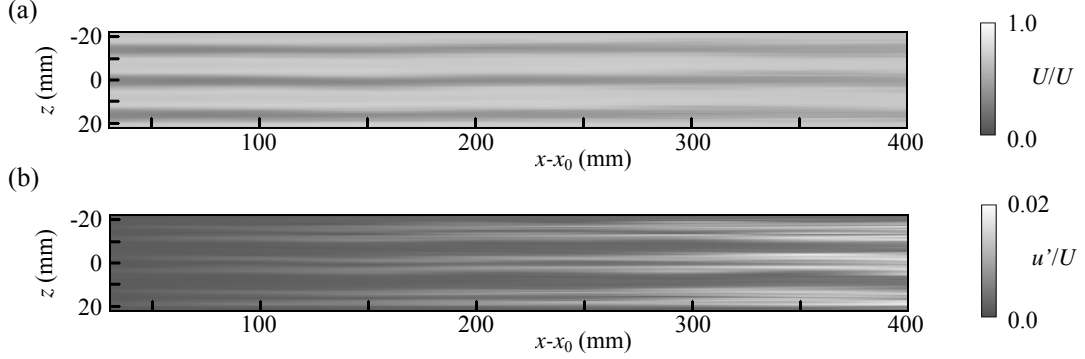


Fig. 2: Distributions of mean velocity U/U_∞ in (a) and r.m.s. value of u -fluctuation u'/U_∞ in (b) in the x - z plane at $y = 3\text{mm}$.

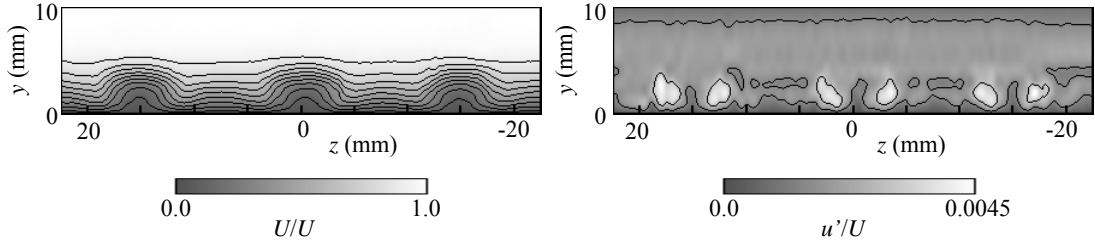


Fig. 3: Distributions of U/U_∞ and u'/U_∞ in the y - z plane at $x-x_0 = 60\text{mm}$.

IV. DEVELOPMENT OF STREAK INSTABILITY

In the present experiment, the subharmonic sinuous mode is excited in the periodic low-speed streaks. The growth of the sinuous mode can generate a train of quasi-streamwise vortices of alternate sign of vorticity, which are considered to be dominant vortices in near-wall turbulence. According to our previous experiment on the linear instability, the subharmonic mode, which is 180° out of phase for the neighboring streaks and therefore has the spanwise periodicity of twice the streak spacing 2λ , is more amplified than the fundamental mode with the same periodicity as the streak spacing λ ($=15\text{mm}$) for the low-speed streaks with the present geometry.

Figure 4 illustrates the development of the subharmonic sinuous mode excited at the most amplified frequency 60Hz in terms of the maximum r. m. s. value u'_m/U_∞ . The disturbance continues to grow exponentially until u'_m/U_∞ exceeds about 0.2 around $x-x_0 = 120\text{mm}$. Figure 5 displays the low-speed streaks at the saturation stage in terms of instantaneous iso-velocity contours in the cross-section at $x-x_0 = 160\text{mm}$. Owing to the growth of the subharmonic sinuous mode, low-speed streaks oscillate with large amplitude in the spanwise direction and interact with the neighboring low-speed streaks. We may expect that being associated with the streak oscillation, the traveling quasi-streamwise vortices are generated and developed along each oscillating low-speed streak. Figures 6(a) and (b) display the distributions of u'/U_∞ in the x - y plane at $z = 0$ and in the x - z plane at $y = 3\text{mm}$ respectively. The disturbances become weak around $x-x_0 = 210\text{mm}$, suggesting that the wavy motion of low-speed streaks disappears around there. The disturbances grow again beyond $x-x_0 = 250\text{mm}$. This suggests that low-speed streaks are developed again beyond there.

To examine the flow development further downstream, flow visualization was done by means of smoke-wire technique. Figure 7 displays a top view picture of the flow visualization. We see the appearance of large-scale arch-like vortices beyond $x-x_0 = 200\text{mm}$, which no doubt results from the

interaction and pairing of quasi-streamwise vortices, and is an important feature of the growth of subharmonic sinuous instability modes. Beyond $x-x_0=200\text{mm}$, it seems that such large-scale vortices break down into smaller vortices. This breakdown stage corresponds to the region where the disturbances become weak (Fig. 6).

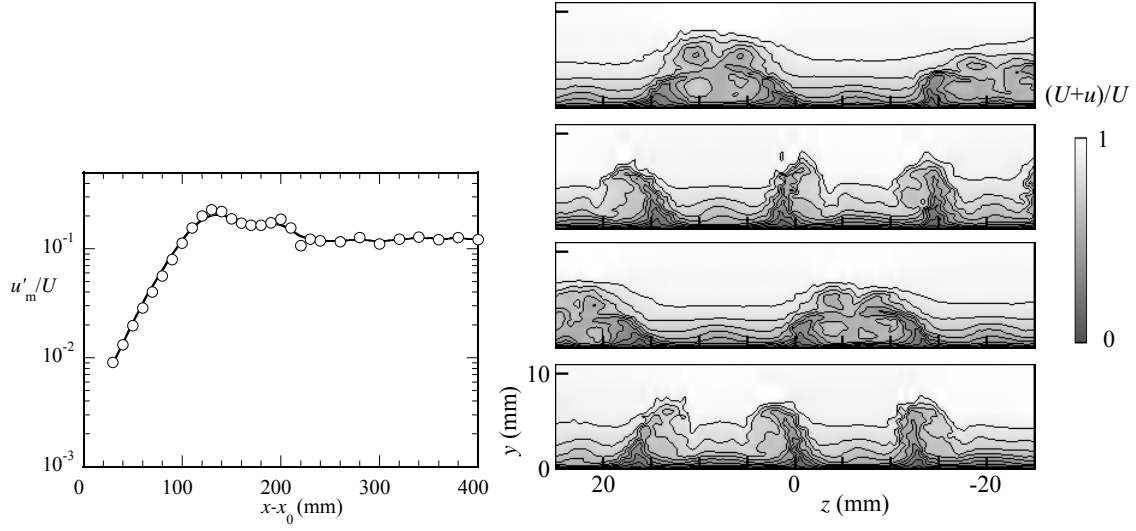


Fig. 4: u'_m/U_∞ versus x . The forcing frequency is 60Hz.

Fig. 5: Ensemble-averaged velocity field in y - z cross section at $x-x_0=160\text{mm}$. Time interval between pictures is one forth of the forcing period (1/60sec).

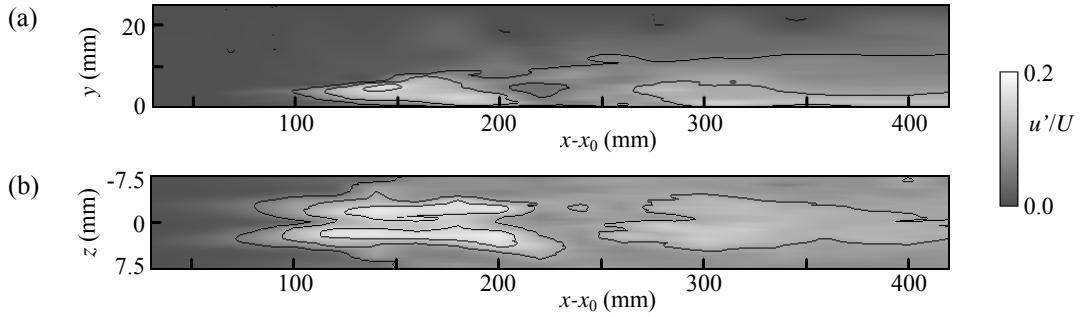


Fig. 6: Distributions of u'/U_∞ . (a) x - y plane at $z=0$, (b) y - z plane at $y=3\text{mm}$. Forcing frequency is 60Hz.

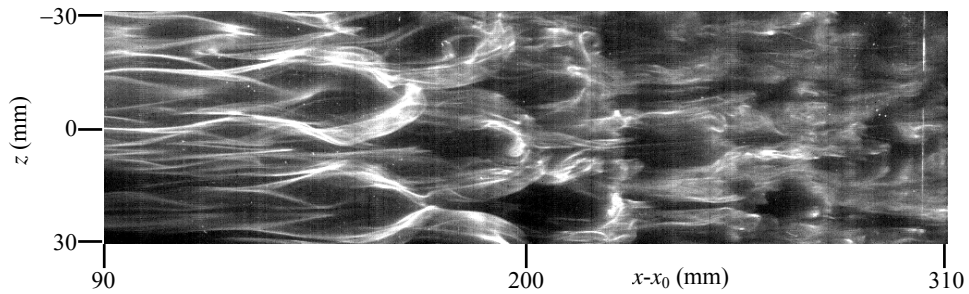


Fig. 7: Flow visualization of the streak instability. Smoke is released from $(x-x_0, y)=(30\text{mm}, 1.5\text{mm})$.

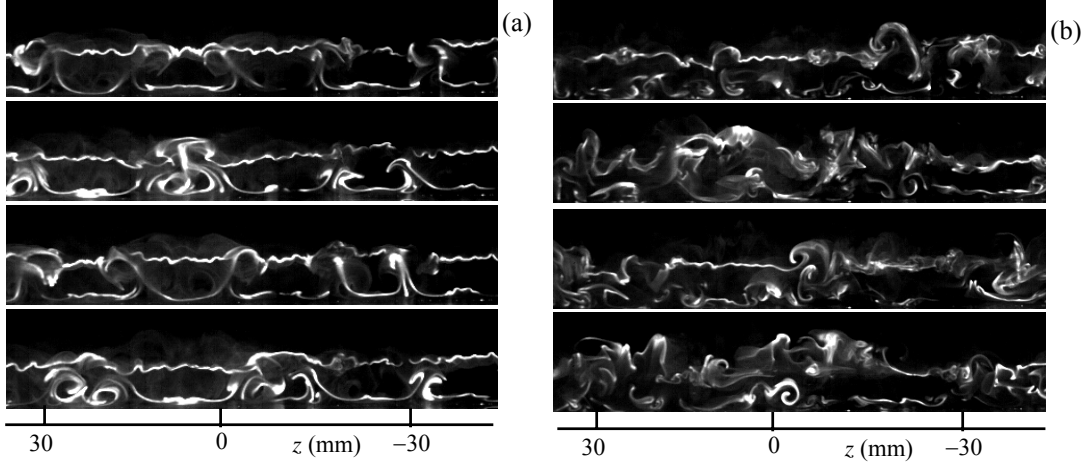


Fig. 8: Flow visualization of the streak instability. Cross-sectional view at $x-x_0=160\text{mm}$ in (a) and 240mm in (b). Smoke is released from the x -location 30mm upstream of the observation x . Time interval between pictures is one forth of the forcing period ($1/60\text{sec}$).

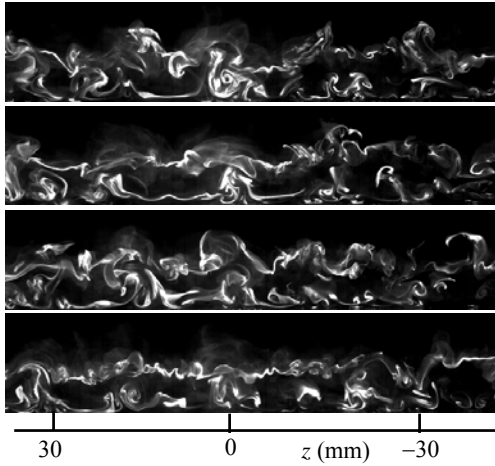


Fig. 9: Flow visualization of the streak instability. Cross-sectional view at $x-x_0=330\text{mm}$. Smoke is released from $x-x_0=300\text{mm}$. Time interval is one forth of the forcing period ($1/60\text{sec}$).

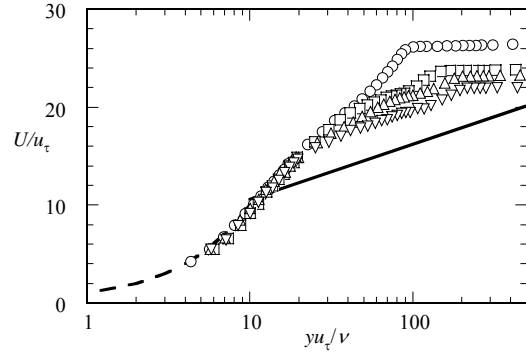


Fig. 10: Mean velocity distributions averaged over the region between $z = -7.5\text{mm}$ and 7.5mm at various x -locations. $x-x_0 = 160\text{mm}, 210\text{mm}, 270\text{mm}, 330\text{mm}$. $--- U/u_\tau = yu_\tau/v$
 $U/u_\tau = 5.62 \log(yu_\tau/v) + 5.0$.

Figures 8(a) and (b) display the cross-sectional view pictures at $x-x_0 = 160\text{mm}$ and 240mm , respectively. At $x-x_0 = 160\text{mm}$, we see development of quasi-streamwise vortices of alternative sign of vorticity (in half forcing cycle) caused by the sinuous instability of low-speed streaks. At $x-x_0 = 240\text{mm}$, such regularly-aligned streamwise vortices seem to disappear as seen from the fact that there is little lift-up smoke, which is consistent with the decrease in u' in Fig. 6. Figure 9 displays the near-wall flow further downstream, at $x-x_0 = 330\text{mm}$. We can see more active motions of near-wall smoke than in Fig.

8(b). It is also worth noting that the mean spacing of the lift-up smoke in this stage (Fig. 9) corresponds to about 100 in wall unit.

Finally, the evolution of the mean velocity field is explained. Figure 10 illustrates the mean velocity distributions $U(y)$ at four stations, $x-x_0 = 160\text{mm}$, 210mm , 270mm and 330mm in the present forced flow. Here, each velocity distribution was obtained by taking the average over the spanwise interval between $z = -7.5\text{mm}$ and $z = 7.5\text{mm}$ (i.e. over the streak spacing $\lambda=15\text{mm}$) at each x -station. At $x-x_0 = 160\text{mm}$, the distribution is still far from the log law distribution in spite that the streak instability has already advanced and quasi-streamwise vortices have been generated. It is after the streak breakdown occurring beyond $x-x_0 = 270\text{mm}$ that the mean velocity distribution $U(y)$ start to exhibit the log-law. It is noted that the distribution of u -fluctuation $u'(y)$ also approach that of wall turbulence beyond $x-x_0 = 270\text{mm}$.

IV. CONCLUSION

In the present experimental study, the nonlinear development of subharmonic sinuous mode of the streak instability was examined up to the stage of the appearance of wall turbulence structure through producing spanwise-periodic low-speed streaks in a laminar boundary layer by using a small piece of screen set normal to the wall. The velocity measurements and visualization pictures clearly demonstrated that the sinuous streak instability causes a train of quasi-streamwise vortices of alternative sign of vorticity to develop. The wavy motion of low-speed streaks continues three or four wavelengths downstream beyond the nonlinear saturation stage, and subsequently the associated vortical structure breaks down into smaller-scale structures. After the streak breakdown, the mean velocity profile starts to exhibit the log-law, and newly generated low-speed streaks have the same lateral spacing as that of developed wall turbulence. The interaction between the quasi-streamwise vortices developing along the neighboring streaks causes large-scale arch-like vortices to develop in the region away from the wall.

ACKNOWLEDGMENTS

This work was in part supported by a Grant-in-Aid for Scientific Research from the Japan Society for the Promotion of Science and a Grant-in-Aid for Special Scientific Research from the Ministry of Education, Sports, Culture, Science and Technology, Japan.

REFERENCES

- [1] Hamilton JM, Kim J and Waleffe F: Regeneration mechanisms of near-wall turbulence structures, *J. Fluid Mech.* 1995, **287**, 317-348.
- [2] Jeong J, Hussain F, Schoppa W and Kim J: Coherent structures near the wall in a turbulent channel flow, *J. Fluid Mech.* 1997, **332**, 185-214.
- [3] Jimenez J and Pinelli A: The autonomous cycle of near-wall turbulence, *J. Fluid Mech.* 1999, **389**, 335-359.
- [4] Schoppa W and Hussain F. Coherent structure dynamics in near-wall turbulence, *Fluid Dyn. Res.* 2000, **26**, 119-139.
- [5] Kawahara G and Kida S: Periodic motion embedded in plane Couette turbulence: regeneration cycle and burst, *J. Fluid Mech.* 2001, **449**, 291-300.
- [6] Itano T and Toh S: The dynamics of bursting process in wall turbulence, *J. Phys. Soc. Japan.* 2001, **70**, 703-716.
- [7] Nishioka M and Asai M: Evolution of Tollmien-Schlichting waves into wall turbulence, In: Tatsumi T eds. *Turbulence and Chaotic Phenomena in Fluids*, North-Holland, 1984, 87-91.
- [8] Matsubara M, Bakchinov AA, Fransson JHM and Alfredsson PH. Growth and breakdown of streaky structures in boundary-layer transition induced by freestream turbulence, In: Fasel H and Saric W eds. *Laminar-Turbulent Transition*, Springer, 2000, 371-376.
- [9] Asai M, Minagawa M and Nishioka M. Instability and breakdown of a near-wall low-speed streak. In: Fasel H and Saric W eds. *Laminar-Turbulent Transition*, Springer, 2000, 269-274.
- [10] Asai M, Minagawa M. and Nishioka M. The instability and breakdown of a near-wall low-speed streak, *J. Fluid Mech.* 2002, **455**, 289-314.
- [11] Konishi Y and Asai M. Experimental investigation of the instability of laminar low-speed streaks. *Proc. 9th Asian Congress of Fluid Mech.* Isfahan, Iran. May, 2002.

SPATIAL AND TEMPORAL STRUCTURE OF A TIME DEPENDENT PIPE FLOW

Y. Satoh, Y. Takeda and D. Sugiyama

Div. of Mechanical Science, Graduate School of Eng., Hokkaido University, Kita-13 Nishi-8, Sapporo, Japan

ABSTRACT: Time dependent velocity distribution of an oscillating pipe flow has been measured by ultrasound Doppler method. Velocity field showed typical pulsatile flow nature as totally different from a stationary pipe flow.

Time domain Fourier transfer was used to obtain temporal characteristics of this flow, as being space dependent power spectrum. By decomposing temporal characteristics and analyzing their spatial dependence of each model, we found the energy is more concentrated in the boundary region (named as HPA – Higher Power Area), and it appears that turbulence starts to be generated in this area by increasing Reynolds number.

1. INTRODUCTION

The theoretical solution of purely oscillating flow was determined by Uchida^[1], and Annular Effect was known as preceding of the phase near the wall of the pipe. Experiments on oscillating pipe flow have been carried out by Christian von Kerczek^[2] for the Stokes layer in oscillating flow and Merkli & Thoman, Hino^{[3][4]} for transition to turbulent flow.

In earlier experiments, it was possible to measure at only one spatial point at the same time. In this experiment, Ultrasonic Doppler Method (UDM) made possible measurement on a line at the same time. The spatial structure of the oscillating pipe flow can be available with UDM.

2. STABILITY DIAGRAM

Figure 1 shows the stability diagram of purely oscillating pipe flow. The types of oscillating pipe flow can be classified in terms of the Reynolds number R_δ and Stokes parameter λ into laminar flow, weakly turbulent flow and conditionally turbulent flow. In weakly turbulent flow, turbulence is generated weakly. In conditionally turbulent flow, turbulence is generated suddenly in the decelerating phase. R_δ is defined as $R_\delta = U\delta/\nu$ using the Stokes-layer thickness $\delta = (2\nu/\omega)^{1/2}$ and the cross-sectional mean velocity amplitude $U = A\omega$. λ is defined as $\lambda = 1/2d(\omega/2\nu)^{1/2}$. (ν =kinematic viscosity, ω =angular frequency, A =amplitude and d =inner diameter of the pipe)

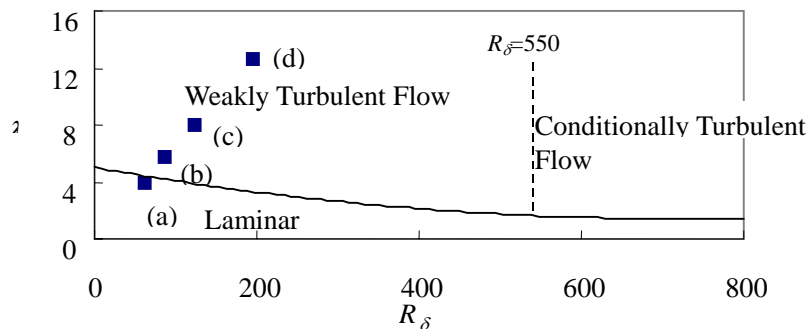


Fig. 1: Stability diagram, Hino *et al.*^[4]

3. EXPERIMENTAL ARRANGEMENT

The general arrangement of the equipment is shown in figure 2. The pipe is connected to the reservoir at one end. The oscillations are driven by an oscillating piston at the other end. A liner motion stepping motor makes the monotonic oscillation of piston. The pipe has an inner diameter of 26 mm and a length of 2000 mm. The measuring section is in a large water tank to prevent changing of temperature.

Velocity was measured by Ultrasonic Velocity Profiler (UVP) with a basic frequency 4 MHz. The transducer is fixed above the pipe with an angle of 78° between the ultrasonic beam axis and the pipe axis. The tracer is Grilex5P1 ($\rho_t=1.05\text{g/cm}^3$). 20 % Glycerol-water solution is used for the fluid to make the density of fluid closer to the density of the tracer.

Coordinate axes are shown in figure 2. The origin O is set on the center of the pipe. The x -axis has the direction of the axis of the pipe. The r -axis has the direction of the radius of the pipe. The x -component of the piston x_t is the intersection of the x -axis and the ultrasonic beam axis.

The piston moves with sin-wave $x=A \sin \omega t$ (x =position of piston head, A =amplitude of sin-wave, ω =angular frequency and t =time). A was kept constant $A=100$ [mm]. ω was set at 0.31, 0.62, 1.25 and 3.14 [rad]. Then $R_\delta=61.5, 87.0, 123.0$ and 194.5 and $\lambda=4.0, 5.7, 8.0$ and 12.6 (Figure. 1 (a) ~ (d)). The measuring points are set every $r/D=0.028$ from $r/D=-0.5$ to $r/D=0.5$ every $x/D=0.769$ from $x/D=5$ to $x/D=23.4$.

4. EXPERIMENTAL RESULTS AND ANALYSIS

Figure 3 shows an example of an instantaneous velocity profile in the accelerating phase. The velocity near the wall is higher than center (Annular effect). Figure 4 is a typical example of the velocity-time series at one spatial point showing a regular sinusoidal motion.

Each time series data was analyzed by FFT in order to see the temporal characteristics of the flow.

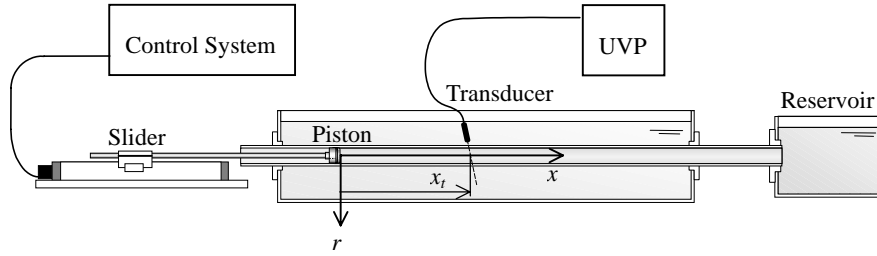


Fig. 2: Experimental arrangement and coordinate axis

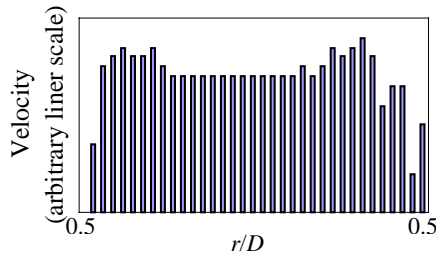


Fig. 3: Example of velocity profile

($R_\delta=123.0, \lambda=8.0, x/D=21.15, \theta=1.3\pi$)

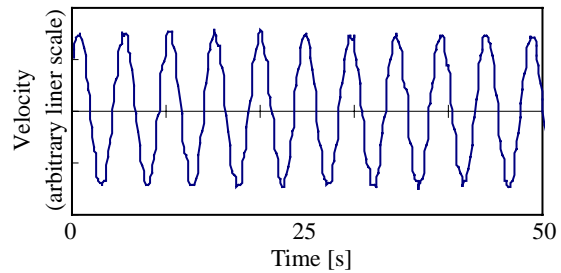


Fig. 4: Example of velocity-time series

($R_\delta=123.0, \lambda=8.0, x/D=21.15, r/D=0$)

Then, analyzed data was averaged over x -axis for $5 < x/D < 23.4$. The space dependent power spectra are shown in Figure 5 for various Reynolds number. The coordinate is the radial position and the abscissa is frequency. The collar represents the magnitude of the power. These graphs show the distribution of the power on the r -axis. The power of the base frequency is much higher than the others at every position. When R_δ and λ are increased, the higher order harmonics can be recognized clearly especially near the wall.

5. DISCUSSION

Figure 6 shows the spatial distribution of the power of the base frequency at various Reynolds number. The distribution has one broad peak in the inner region of the pipe at $R_\delta=61.5$, $\lambda=4.0$ (a). The

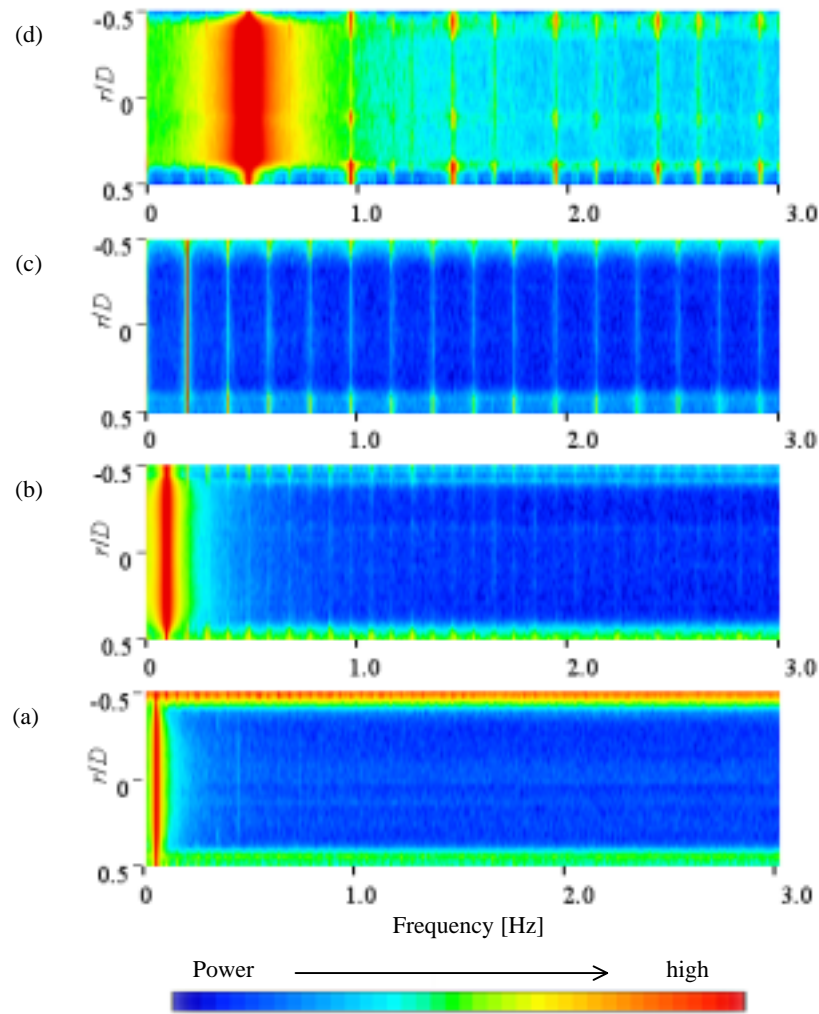


Fig. 5 : Space dependent power spectrum

(a) $R_\delta=61.5$, $\lambda=4.0$ (b) $R_\delta=87.0$, $\lambda=5.7$

(c) $R_\delta=123.0$, $\lambda=8.0$ (d) $R_\delta=194.5$, $\lambda=12.6$

distribution has two peaks outside of the central region at $R_\delta=87.0$, $\lambda=5.7$ (b). We call those peaks Higher Power Area (HPA). Two HPAs appear too at $R_\delta=123.0$, $\lambda=8.0$ (c). But the location is closer to the wall and the space between each HPA is wider than (b). The distribution looks like a trapezoid at $R_\delta=194.5$, $\lambda=12.6$ (d). For all cases power is lower just next to the wall.

Figure 7 shows the similar spatial distribution of the power of the second harmonic mode. Two HPAs appear near the wall, but their location is closer to the wall than that of the base frequency. The distribution looks almost flat in the inner region for all cases.

The case (a) corresponds to laminar flow according to Hino^[4] and Fig.1. The spatial distribution of the base frequency is higher in the inner region. This seems reasonable since oscillation is driven by a sinusoidal motion of the piston and the energy is given to fluid uniformly. On contrary for (c) to (d), Most of the power is distributed near the wall. This indicates that this mode is generated by being caused by a boundary layer. It may be considered that the energy of the basic mode is transferred to this higher harmonic mode inside this boundary layer, and as a result, the power of the base frequency is much lower than in the inner region.

From this result, flow transition from laminar to turbulent flow might be defined as following. For laminar flow the energy is concentrated only on the basic mode and there is no HPA of the fundamental frequency and are the power of the higher harmonic mode is low. When R_δ and λ are increased, HPA appears with fundamental frequency outside of the central region as well as for the higher harmonic mode. The HPA of harmonic mode appears just next to the wall at (b) and is moving to the central region of the pipe by increasing R_δ . The power itself appears to increase. Consequently, the flow is considered to transit to weekly turbulent flow.

This result also indicates that the boundary layer is given the energy from the basic mode through the higher harmonic mode by nonlinear mechanisms because the power of fundamental mode is lower relative to other region and that of the harmonic frequency is higher near the wall. In other word, the fact that the power of fundamental frequency is higher near the wall when R_δ and λ are increased means the flow in this area is following the motion of the piston more faithfully. It corresponds to see the annular effect. However when R_δ and λ are small, the peak of the power of base frequency is at the center. Annular Effect may not be seen in laminar flow.

6. CONCLUSION

Spatial and temporal characteristics of the oscillating pipe flow was investigated. From the space dependent power spectra, flow transition might be defined using the appearance of HPA and the behavior of their location. The transition scheme observed seems to support the earlier investigation. It suggests a possible future work on the flow transition based on the energy transfer among various harmonic modes.

ACKNOWLEDGMENTS

The authors wish to thank the supporting work of Mr. T. Sampo.

REFERENCES

- [1] Uchida S. The pulsating viscous flow superposed on the steady laminar motion of incompressible fluid in a circular pipe: *Z. Angew. Math. Phys.* 1956, **7**, 403-422
- [2] Kerczek CV and Davis SH: Liner stability theory of oscillatory Stokes layers , *J. Fluid Mech.* 1974, **62** (4), 193-207
- [3] Merkli P and Thomann H: Transition to turbulence in oscillating pipe flow , *J. Fluid Mech.* 1975, **68** (3), 567-575
- [4] Hino M, Sawamoto M, Takasu S: Experiments on transition to turbulence in an oscillatory pipe flow , *J. Fluid Mech.* 1976, **75** (2), 193-207
- [5] Elkholy AH. Sinusoidal excitation of viscous fluids in pipes: *Int. J. Pres. Ves. & Piping* 70 1997, 161-165

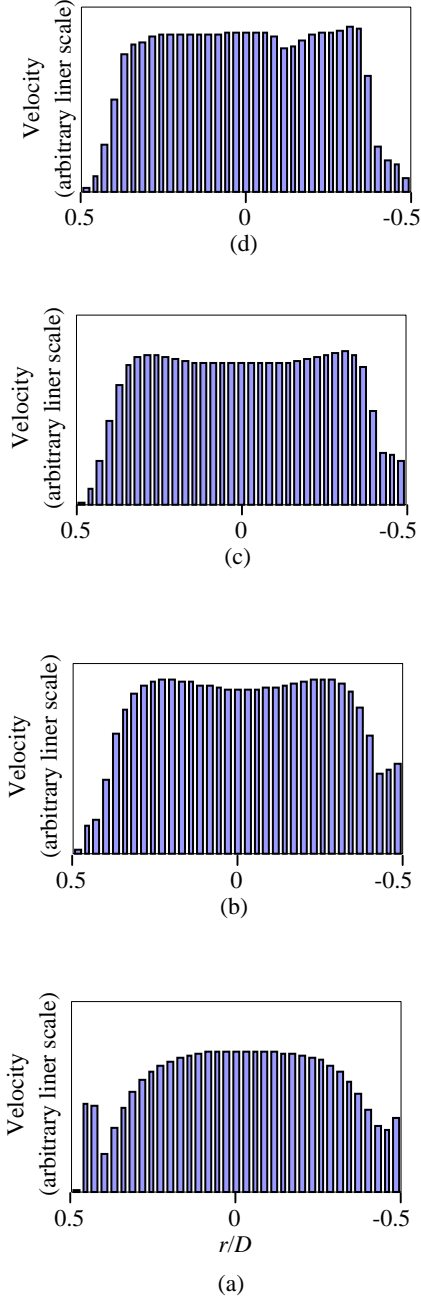


Fig. 6 : Spatial distribution of the power of base frequency

(a) $R_\delta=61.5, \lambda=4.0$ (b) $R_\delta=87.0, \lambda=5.7$
(c) $R_\delta=123.0, \lambda=8.0$ (d) $R_\delta=194.5, \lambda=12.6$

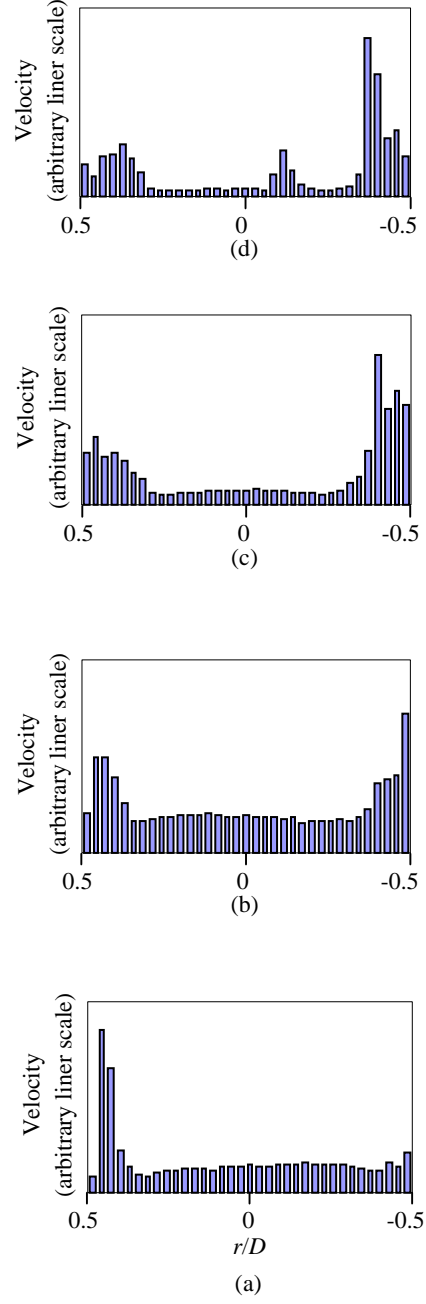


Fig. 7 : Spatial distribution of the power of second harmonic

(a) $R_\delta=61.5, \lambda=4.0$ (b) $R_\delta=87.0, \lambda=5.7$
(c) $R_\delta=123.0, \lambda=8.0$ (d) $R_\delta=194.5, \lambda=12.6$

Mixing in an oscillatory flow in a container

J. Hariharan & Kidambi Rangachari
Computational & Theoretical Fluid Dynamics Division,
National Aerospace Laboratories, Bangalore 560 017, India.

ABSTRACT : We consider fluid mixing in a periodically lid driven rectangular container, at low Reynolds number. We compare mixing patterns produced by two calculational procedures - a) the velocity field is computed from the steady Stokes equation. This is the traditional approach. b) the velocity field is computed from the linearised Navier-Stokes equation where the unsteady term is retained. Similar mixing patterns are obtained from both approaches for an initial dye-line corresponding to the experimental condition in [3]; they are in good agreement with the experimental pattern as well. Poincare maps are employed to identify initial tracer locations that would lead to substantial differences in finite time mixing patterns obtained from the quasi-steady and the unsteady approaches.

1 Introduction

A large body of experimental and numerical work exists on the technologically important problem of mixing of and by fluids, especially in the low Reynolds number regime [3] where the Reynolds number Re is based on the lid velocity. Experimental work consists of setting up of periodic flow fields by appropriate boundary motions and then following the evolution of a fluid element (usually a dye in the form of a line or a blob) for a certain number of time periods. For two-dimensional flows, it is essential for good mixing that the flow fields be unsteady. For these low Re flows in two-dimensional rectangular containers (the object of this paper), experiments have traditionally focussed on generating good mixing by having both the top and bottom ‘lids’ move. In fact, for the lid motion protocols and the parameters traditionally adopted, this is the only way to generate good mixing. Numerical work consists of three steps, in sequence - (i) computation of the velocity field for given boundary motions (which involves solving a PDE) followed by (ii) the calculation of the motion of a fluid particle (which involves integrating a two or three dimensional system of ODEs where the right hand sides are known from the earlier step) and (iii) an assessment of the mixing characteristics of the flow which are well-known to be correlated with whether a flow is regular or chaotic.

Computation of the velocity fields is more or less standard, at least for the container geometries and lid motion protocols of most interest (rectangular and cylindrical). Extensive numerical computations exist for rectangular cavity flows from very small to quite large Re [5]. Analytic methods based on eigenfunction expansions are also available for the steady Stokes regime [2], [4]. The unsteadiness of the flow field is purely due to the time-dependent boundary motion; the flow field is quasi-steady rather than really unsteady. The solution of the ODES, which would give the particle paths, can seldom be achieved in closed form - a numerical integration by one of the many standard methods is the only resort. Mixing analyses usually take the form of location of periodic points of the flow, generation of Poincare maps and evolution of lines or blobs of particles. Quantitative estimates of mixing are pretty hard to make - the typical calculation finds the stretching rates of material line or area elements. The former is calculated for two dimensional situations (the stretching rate for an area element is always one in this case) whereas in three dimensions both rates provide an estimate for mixing. Analytical work wherein the Lyapunov exponents can be calculated and actual mixing efficiencies computed is limited to very simple idealised flow fields.

An analytic solution of the linearised Navier-Stokes equation (or the unsteady Stokes equation) for a periodic two dimensional lid-driven rectangular container was given in [6]. It was shown there, that under certain conditions, it is meaningful to retain the unsteady term while dropping the nonlinear convective term in the Navier Stokes equation i.e. a linearisation of the N-S equations makes sense. The retention of this term led to the flow field being truly unsteady and revealed interesting inertial effects in the field - in particular, a lagging of the flow with respect to the lid and formation of various transient eddy structures when the lid reversed its direction of motion. In this paper, we consider how the mixing patterns are affected by the retention of the unsteady term.

2 Analysis

2.1 The linearised Navier-Stokes equation

Consider a rectangular container of width L and depth H completely filled with a Newtonian fluid of density ρ and kinematic viscosity ν . The lid of the container, assumed to make perfect contact with the fluid, oscillates in its own plane generating a velocity field in the fluid. We use a two-dimensional cartesian coordinate system with \hat{x} aligned with the direction of the lid motion and with \hat{z} perpendicular to it and upwards; the origin will be at the middle of the container on the plane of symmetry. Let Ω and a be the frequency and amplitude of the lid motion and U be its maximum linear speed. Non-dimensionalising all lengths by L , time by Ω^{-1} , velocities by U and the pressure by $\rho\nu U Re / L$ and assuming the Strouhal number $Sr = L/a \gg 1$, the field is determined by the single scalar equation

$$\nabla^4 \psi - iRe \nabla^2 \psi = 0 \quad (1)$$

where the ‘oscillatory’ Reynolds number $Re = \Omega L^2 / \nu$ and ψ the reduced stream function. The actual stream function is obtained by taking the real part of $\psi(x, z) e^{it}$. The boundary conditions on the reduced stream function are

$$\psi(\pm 1/2, z) = \psi_{,x}(\pm 1/2, z) = 0, \quad \psi(x, \pm h/2) = \psi_{,z}(x, -h/2) = 0, \quad \psi_{,z}(x, h/2) = u_0(x). \quad (2)$$

The lid speed

$$u_0(x) = \begin{cases} 1.0 & 0 \leq |x| < \frac{1}{2} - \delta \\ 0.5\{1 + \cos[\pi(|x| - (1/2 - \delta))/\delta]\} & \frac{1}{2} - \delta \leq |x| \leq \frac{1}{2} \end{cases} \quad (3)$$

Thus $u_0(x)$ is just one over most of the lid but goes monotonically to zero near the sidewalls; δ has been taken to be 0.1.

2.2 The velocity field

We briefly recall the eigenvalue expansions for the streamfunction ψ from [6]. These can be written in terms of a symmetric and an antisymmetric part -

$$\psi_s(x, z) = \sum_n a_n f_n(x; \lambda_n^u) \frac{\cosh \lambda_n^u z}{\cosh \lambda_n^u h/2} + \sum_n b_n f_n(x; \lambda_n^l) \frac{\cosh \lambda_n^l z}{\cosh \lambda_n^l h/2} \quad (4a)$$

$$\psi_a(x, z) = \sum_n c_n f_n(x; \lambda_n^u) \frac{\sinh \lambda_n^u z}{\sinh \lambda_n^u h/2} + \sum_n d_n f_n(x; \lambda_n^l) \frac{\sinh \lambda_n^l z}{\sinh \lambda_n^l h/2}. \quad (4b)$$

Here the $f_n(x)$ are given by

$$f_n(x) \sim \cos \lambda_n x + B \cos \sqrt{\lambda_n^2 - iRe} x \quad (5)$$

with the eigenvalues λ_n the roots of

$$\lambda \tan \frac{\lambda}{2} = \sqrt{\lambda^2 - iRe} \tan \frac{1}{2} \sqrt{\lambda^2 - iRe} \quad (6)$$

and the scalar $B = -\cos \frac{1}{2} \lambda / \cos \frac{1}{2} \sqrt{\lambda^2 - iRe}$. The a_n , b_n , c_n and d_n are complex scalars that have to be determined from the boundary conditions. The boundary conditions on $z = h/2$ are

$$\psi_s(x, \pm h/2) = \psi_a(x, \pm h/2) = 0, \quad \psi_{s,z}(x, h/2) = \psi_{a,z}(x, h/2) = \frac{1}{2} u_0(x). \quad (7)$$

The scalars can be determined by the least squares procedure that was described in detail in [4]. Briefly, we truncate all sums in (4) to N terms, choose M equidistant points on $[0, 1/2]$ and determine the $4N$ coefficients in such a way that the boundary conditions are satisfied in a least square sense on these points. For all the calculations here, $N = 20$ and $M = 2N$.

2.3 Particle trajectories

With the computation of the velocity field in hand, one can calculate the trajectory of an individual particle that is being advected by this velocity field. The coordinates of the particle (x, z) satisfy the pair of ODEs

$$\frac{dx}{dt} = \frac{1}{Sr} \frac{\partial \Psi}{\partial z}, \quad \frac{dz}{dt} = -\frac{1}{Sr} \frac{\partial \Psi}{\partial x} \quad (8a,b)$$

(8) is a Hamiltonian system with $\Psi(x, z, t)$ being the Hamiltonian function. The phase space of this system is the scaled (with \sqrt{Sr}) physical $x - z$ space in the case of steady motions and the scaled torus $S^1 \times [-1/2, 1/2] \times [-h/2, h/2]$ (i.e. a torus of rectangular cross-section) in the case of a time periodic flow. If Ψ is independent of time, as in the case of flow in a container driven by a lid moving with constant velocity, (8) is a one degree-of-freedom system possessing one constant of motion Ψ . This system is integrable and the phase space is foliated into curves on which Ψ is constant. A particle starting on a particular streamline stays on that streamline. The mixing is very poor.

If Ψ is separably time dependent such that $\Psi(x, z, t) = \psi(x, z)f(t)$ where $f(t)$ can be an arbitrary function of time, (8) is formally a two degree-of-freedom system which generally requires two constants of motion to be integrable. However, for this special form of Ψ , (8) is again an integrable system as it can be written as a Pfaffian differential equation in the two variables x, z . Only a single lid moving, in the traditional quasi-steady approximation gives rise to this situation. Note that the actual details of the lid motion don't matter. The mixing is again very poor and that is the reason why both lids have to be moved to obtain good mixing.

If Ψ cannot be written in separable form, then the flow field is truly unsteady. This is traditionally accomplished by moving the lids either in a discontinuous fashion or in a sinusoidal mode but with a phase lag. It is important that the lids follow different protocols (that is why the phase-lag is important); otherwise Ψ can again be written in separable form. This is a truly two degree-of-freedom system; Hamiltonian theory tells us that such systems are capable of exhibiting chaotic solutions.

Equations 8(a),(b) are integrated by a fourth order RK method with a timestep $\delta t = 0.001 T$ where T is the time period of the lid motion. The calculations have been checked with a smaller step $\delta t = 0.0001 T$.

3 Results & Discussion

A number of experiments on mixing in two-dimensional rectangular containers have been performed ([3] and references therein). In these experiments, the liquid filling the container is glycerine and both the top and bottom walls move (otherwise the mixing is poor); discontinuous and sinusoidal motions of the walls are the commonly employed protocols. In the experiments, the walls move only in one direction - they can be either co-rotating or counter-rotating. The eigenfunction expansion procedure used in [6] cannot be used directly for the discontinuous protocol since the wall motions now consist of an infinite number of frequencies. However, the procedure directly applies to the sinusoidal protocol and these are the cases with which we compare here.

It has been estimated that 'simple' mixing flows, such as those corresponding to the experiments which have been performed, can take 10^2 years of computational time in a megaflop machine [1]. Hence, we compute for a case where results are available for a small number of periods. The case that we focus on is case (b) on page 206 of [3]. The rectangular container has width $L = 10.3 \text{ cm}$ and height $h = 6.2 \text{ cm}$. The top and bottom lids move according to a sinusoidal protocol SP as

$$v_{top} = U_{top} \sin^2\left(\frac{\pi t}{T_{top}} + \alpha\right),$$

$$v_{bot} = -U_{bot} \sin^2\left(\frac{\pi t}{T_{bot}}\right).$$

$U_{top} = U_{bot} = 2.69 \text{ cm/s}$, the time periods $T_{top} = T_{bot} = T = 20 \text{ sec}$ and the phase angle $\alpha = \pi/2$ are the experimental values used. Using the non-dimensionalisation of §2, the container is of unit width and $h = 0.6019$. Using $\nu = 11.876 \text{ m}^2/\text{s}$, we get $Re = 2.80643$, $Sr = 1.2029$.

The mixing patterns produced after 14 periods, due to an initial dye-line extending from $(-0.31068, h/2)$ to $(-0.26214, h/2)$ by the quasi-steady and unsteady computations are shown in figures 1 (a) and (b). The macroscopic patterns are very similar to each other and to that in figure 7.5.4(b) of Ottino(1989). Gross features that are seen in the experimental mixing pattern are fairly well reproduced in the computation. In these calculations the evolution of the horizontal diameter of the blob is traced rather than the entire blob itself. This is because of the enormous amount of time that the computation takes due to the severe stretching and folding of the dye line due to the flow. For example, a line initially with three points stretches to have around 10,000 points at the end of the fourteenth period in the unsteady calculations. Points are added such that a minimum distance of 0.02 is maintained between neighbours.

Figure 2 shows the Poincare map obtained by strobing a particle trajectory at each period, for 10,000 periods. Clear differences are discernible between the quasi-steady (figure 2(a)) and the unsteady maps (figure 2(b)) even for the small $Re = 2.80643$. Barring a thin strip near the side walls, a chaotic sea covers the rest of the container in both cases though there are a couple of elongated islands in the quasi-steady case. The central island of figure 2(a) (quasi-steady computation) is larger than the corresponding island of figure 2(b); the three satellite islands surrounding the central island in figure 2(a) have all but disappeared in figure 2(b).

We now present a result that shows that there exist possible initial dye-line locations which will lead to vastly different mixing patterns at the end of a finite number of periods. With the Poincare maps of figure 2 as guide, we choose the initial dye-line to be the segment $[(0.05, 0.24), (0.08, 0.24)]$; this segment lies in one of the satellite islands of figure 2(a) but the chaotic sea in figure 2(b). We expect the mixing to be poor in the former case and better in the latter - this is actually seen in figures 3(a) and (b).

We have examined the effect of the unsteady inertial term on mixing in a double lid driven container. We have compared the computational mixing patterns due to a flow with a low $Re = 2.80643$ with the corresponding experimental one and found that they compare well. An examination of the Poincare maps for the quasi-steady and unsteady cases shows that this is not surprising; the dye-line in question lies initially in the chaotic sea in both cases and thus undergoes severe stretching and folding. However, even for this low Re , there exist initial dye locations which lead to vastly different mixing patterns when the two approaches are used to calculate them. This typically happens when the said location is in the chaotic sea in one of the Poincare maps but in an island in the other. Thus, if the dye element would have been placed here in the experiment, the mixing pattern after a finite number of periods would have been vastly different from the one that a quasi-steady computation would have given. It is another matter that, to the authors' knowledge, such a computation does not seem to have been done till now even for the experimental conditions in Ottino (1989).

References

- [1] Franjione, J.G. & Ottino, J.M. 1987 Feasibility of numerical tracking of material lines and surfaces in chaotic flows. *Phys. Fluids* 30 : 3641 – 3643.
- [2] Meleshko, V.V., Malyuga, V.S. & Gomilko, A.M. 2000 Steady Stokes flow in a finite cylinder. *Proc. R. Soc. Lond. A* 456 : 1741 – 1758.
- [3] Ottino, J.M. 1989 The kinematics of mixing: stretching, chaos, and transport. *Cambridge University Press*
- [4] Shankar, P.N. 1993 The eddy structure in Stokes flow in a cavity. *J. Fluid Mech.* 250 : 371–383.
- [5] Shankar, P.N. & Deshpande, M.D. 2000 Fluid mechanics in the driven cavity. *Annu. Rev. Fluid Mech.* 32 : 93–136.
- [6] Shankar, P.N., Kidambi, R. & Hariharan, J. 2003 Oscillatory eddy structure in a container. *J. Fluid Mech.* 493 : 163–185

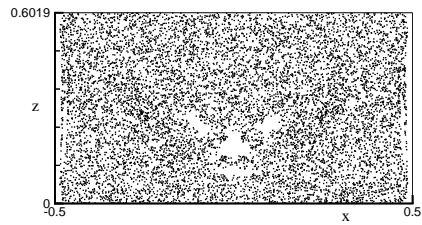


(a)

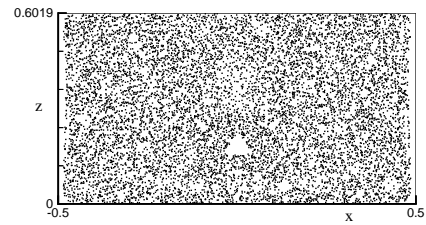


(b)

Figure 1: Mixing pattern after 14 periods. (a) Quasi-steady computation (b) Unsteady computation.

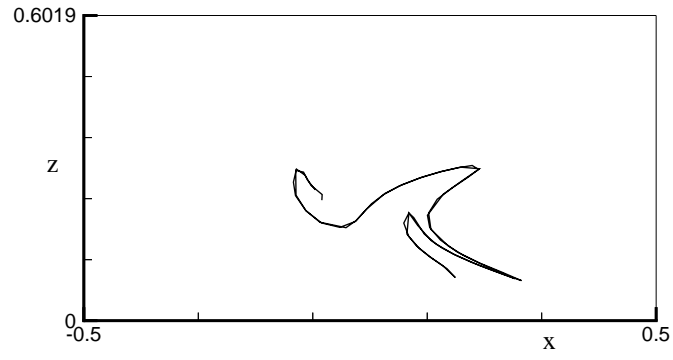


(a)

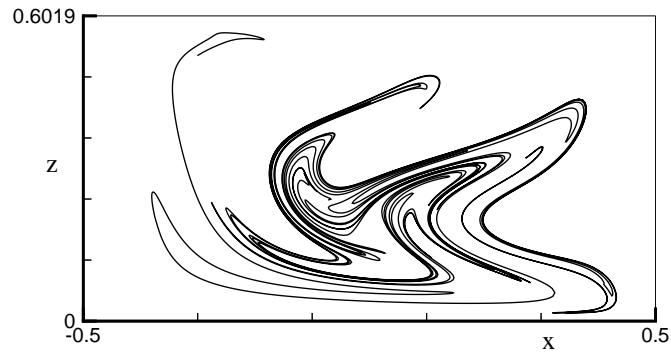


(b)

Figure 2: Poincare maps corresponding to figure 1. The maps are generated by iterating the single initial condition $(0.2, 0.2)$ for 10000 periods. (a) Quasi-steady calculation (b) Unsteady calculation.



(a)



(b)

Figure 3: Mixing pattern due to the initial line segment $[(0.05, 0.24), (0.08, 0.24)]$ after 14 periods. (a) Quasi-steady calculation (b) Unsteady calculation.

UNSTEADY INCOMPRESSIBLE VISCOUS FLOWS AROUND TWO CIRCULAR CYLINDERS IN TANDEM

Z.D. Su and H.J. Zhang

Department of Metrological Engineering, China Institute of Metrology, Hangzhou 310034, China

Y. Liu

Department of Mechanical Engineering, The Hong Kong Polytechnic University, Hong Kong, China

ABSTRACT: Cross flow over two cylinders in tandem has been numerically and experimentally studied. The Reynolds numbers under consideration are 200 and 1000 and the spacing ratios are 2.0, 3.0, 4.0 and 5.0. The computation is carried out by the finite element method. The Laser Induced Fluorescence experiments are carried out to verify the calculated results. In the case of $Re = 200$, the calculations are quite consistent with the experimental visualization. Both the calculations and experimental visualization indicate that the critical spacing ratio is between 4.0 and 5.0. In the case of $Re = 1000$, the calculations are also consistent with the experimental visualization. However, the critical L/D is reduced to between 3.0 and 4.0 due to the instability of high momentum shear layer.

1. INTRODUCTION

Multiple cylinders in a cross flow is one of the most revealing and basic problems in the general subject of fluid-structure interaction. The present study concentrates on the numerical and experimental visualization of flow pattern for two tandem cylinders in a cross flow. A schematic view of the problem is shown in Fig. 1. Two cylinders in tandem are placed in a uniform flow of velocity U , L is the center-to-center distance between the cylinders and D is the cylinder diameter. The flow is considered to be incompressible. There are three regimes for flow past two tandem circular cylinders^[1, 2]. Various degree of the wake interference between two cylinders depending on the spacing ratio L/D can trigger different aspects of vortex shedding such as intermittent shedding and co-shedding^[3, 4]. The first flow regime is observed when two cylinders are in contact or very close. In this case two cylinders act like a single cylinder. The second flow regime is observed when the spacing ratio is in the range, $1.2 \sim 1.8 < L/D < 3.4 \sim 3.8$. A separation bubble is formed behind the upstream cylinder and is captured by the downstream cylinder. There is a reattachment of the shear layer emanating from the first cylinder to the wall of the second one. The wake is formed behind the downstream cylinder due to separation occurring on its surface. Finally, the third flow regime is observed when $L/D > 3.4 \sim 3.8$. Vortex shedding occurs from both cylinders. The wake behind the second cylinder is called binary, because each vortex is formed by the combination of one vortex shed from the upstream cylinder and another by the downstream cylinder. The spacing at which this occurs is called the critical spacing^[5, 6, 7].

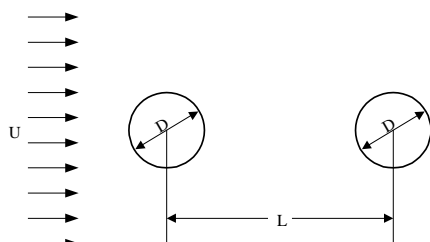


Fig.1: Schematic view of the problem

It is generally agreed that increasing Reynolds number will result in decreasing the critical spacing ratio. The cases of Zdravkovich^[7] considered are in subcritical Reynolds number flow regime in which the critical spacing ratio was about $L/D = 3.8$. In the certain range of Reynolds numbers, the critical spacing ratio doesn't change remarkably with Reynolds number. But for the supercritical flows, the critical spacing ratio could be smaller than 2.8^[8]. On the other hand, even for the subcritical case, Liungkrona *et al.*^[9] reported that the critical spacing could be larger than 4 for $Re = 3000$. Other flow characteristics besides the flow pattern were also studied experimentally. Arie *et al.*^[10] measured pressure distributions and forces acting on the two tandem cylinders. They found that the drag of the

downstream cylinder is greatly reduced due to the existence of the upstream cylinder and overall drag of two cylinders is less than that of the single cylinders. Liungkrona *et al.* ^[9] also investigated the surface pressure on the two tandem cylinders with various ranges of free stream turbulence intensities and spacing ratios.

The flow field around two circular cylinders in tandem has also been investigated numerically. Tezduyar *et al.* ^[11] investigated a similar problem with $L/D = 1.5$ and a Reynolds number, $Re = 100$, using a finite element formulation with the streamline-upwind/Petrov-Galerkin (SUPG) method. Li *et al.* ^[12, 13] developed a finite element program to simulate the vortex shedding. The computations were carried out at $Re = 100$ for $L/D = 2.0, 3.0, 4.0$ and 6.0 . Slaouti and Stansby ^[14] studied the flow around two circular cylinders in tandem using the random-vortex method at $Re = 200$ with several spacing ratios. Mittal *et al.* ^[15] employed a stabilized finite element formulation to study incompressible flows past a pair of cylinders in tandem at $Re = 100$ and 1000 with $L/D = 2.5$ and 5.5 . Their results showed that when $Re = 1000$ and $L/D = 2.5$, both cylinders have their own vortex shedding. Farrant *et al.* ^[16] used the cell boundary element method to solve the flows around two cylinders in tandem with $L/D = 4.0$ at $Re = 200$. Meneghini *et al.* ^[17] simulated the flow around two cylinders in tandem by finite element method. The calculations were carried out with $L/D = 1.5, 2.0, 3.0$ and 4.0 at $Re = 200$. For the results of Slaouti and Stansby ^[14], Farrant *et al.* ^[16] and Meneghini *et al.* ^[17], when $Re = 200$ and $L/D = 4.0$, both cylinders have their own vortex shedding. Recently, Jest and Kallinderis ^[18] used a second order streamline upwind Petrov-Galerkin projection scheme to compute flow past two circular cylinders in tandem at $Re = 1000$. Their result indicated that the critical spacing ratio is about 2.38.

In this paper we report our computational results for flows past two circular cylinders in tandem at $Re = 200$ and 1000 for $L/D = 2.0, 3.0, 4.0$ and 5.0 . The numerical technique is a finite element method using an operator-splitting time stepping scheme. The Laser Induced Fluorescence (LIF) experiments are conducted to verify the calculated results.

2. RESEARCH METHODS

2.1 Finite Element Method

The two-dimensional computation domain is a $60D \times 20D$ rectangular region, the upstream length is about $10D$, while the downstream length is $50D$, and the two cylinders are symmetric about the centerline.

The Navier-Stokes equations are solved using a finite element method and the non-linear coupling terms in the equations are treated separately at different fractional time steps, by an operator-splitting time-stepping method ^[19]. The variational form of the above numerical system is discretized with Galerkin finite element procedures. The boundary conditions are chosen as $u = 1$, $v = 0$ at the inlet and along the top and bottom boundaries. On the cylinder surface, $u = 0$ and $v = 0$ are specified. At the outlet boundary, $\partial u / \partial n = 0$ is imposed.

Since the boundary layer is expected to be thin near the cylinder, a fine mesh is specified near the cylinder surface. 6-noded triangular element is used. The number of nodes is about 99500, and the number of elements is numerically determined to be about 49750, which is adequate to resolve the velocity and the boundary layers. These numbers are determined by using different meshes, from coarse to progressively finer meshes, until the drag coefficient is mesh-convergent to within a prescribed tolerance of about 0.5%.

2.2 Experimental Method

The Laser induced Fluorescence (LIF) experiments are carried out in a water tunnel, with a $150 \text{ mm} \times 150 \text{ mm}$ cross-section and 500 mm in working length. The cylinder models are constructed of glass with $D = 10 \text{ mm}$ and the cylinder aspect ratio is 15. The front cylinder has two-dye injection ports of 0.5 mm diameter located at mid-span and near the points of boundary layer separation.

The mid-section of two cylinders are illuminated with a scanning light sheet generated by a 5W Argon-ion laser source (Spectra-Physics Stabilite 1017). A scanner controller is used to control the scanning frequency of the light sheet with a range from 1.5 ms to 12.5 ms . Dye streaklines are illuminated by this Argon-ion laser and recorded with a JVC GY-DV500 digital Camcorder. The shutter time used

here is 0.008s, which is fast enough to capture the motion of the streak line. The video results were firstly recorded in mini digital tape, and then transferred to a PC computer memory stick after the analysis of video results with Sony PC120X digital video camera.

The fluorescent dye Rhodamine is injected into the front cylinder. Under the illumination of Argon-ion laser, the Laser Induced Fluorescence (LIF) occurs. The fluorescent color of Rhodamine is brilliant yellow. Compared with the still camera photo, a more detailed description of the flow pattern could be achieved by searching videotape carefully.

There are two methods used in this experiment to monitor the flow velocity: one is the orifice flowmeter and another is to use the tracing seed particles and timer. The discrepancy of velocity and the corresponding Reynolds number are conservatively estimated to be less than 5%.

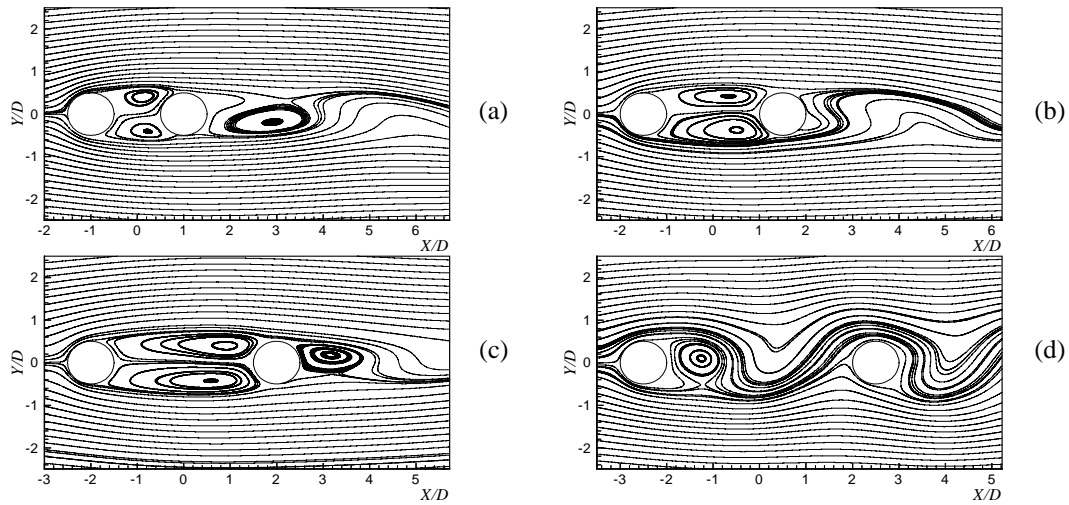


Fig.2: Streamline patterns at $Re = 200$ for $L/D = 2.0$ (a), 3.0 (b), 4.0 (c) and 5.0 (d)

3. RESULTS AND DISCUSSIONS

The calculated stream-function fields around two circular cylinders in tandem at $Re = 200$ for $L/D = 2.0, 3.0, 4.0$ and 5.0 are shown in Fig. 2. When the two cylinders are close to each other ($L/D = 2.0$), as shown in Fig. 2a, the two outer shear layers separated from the upstream cylinder transit the inter-space of the two cylinders and reattach to the downstream cylinder, forming two standing vortices of equal sizes between the two cylinders. A regular vortex shedding occurs behind the rear cylinder. When L/D is increased to 3.0 (Fig.2b) and 4.0 (Fig.2c), the two standing vortices of equal sizes have been lengthened gradually. When L/D is further increased to 5.0 (Fig.2d), the rear cylinder is far enough apart from the front cylinder. As a result, regular vortex shedding from the upstream cylinder can be freely convected. The upstream cylinder also emits its own vortices simultaneously. To verify these numerical results, the experimental visualization is shown in Fig.3. Like the calculated flow patterns, when $L/D = 4.0$ (Fig.3a), shear layers transit the inter-space of the two cylinders, and no vortex sheds from upstream cylinder. When $L/D = 5.0$ (Fig.3b), it can be clearly seen that vortices shed from the both cylinders.

The case of $Re = 1000$ is also studied both numerically and experimentally for $L/D = 2.0, 3.0, 4.0$ and 5.0 . Similar to the discussion in Fig. 2, when $L/D = 2.0$ (Fig.4a) or $L/D = 3.0$ (Fig.4b), intermittent rolling-up of the two separated shear layers from the front cylinder is set in and they are seen alternately to reattach at the rear cylinder. This pair of rolling-up shear layers also results in two standing vortices with unequal size right after the front cylinder. The main difference between $Re = 1000$ and $Re = 200$ case is that the critical spacing ratio for $Re = 200$ is larger than four, but that of $Re = 1000$ is smaller than four. The most likely explanation for this behavior is that the high momentum fluid leads to a greater instability of the shear layer. When $L/D = 4.0$ (Fig.4c) and $L/D = 5.0$ (Fig.4d), both cylinders shed their

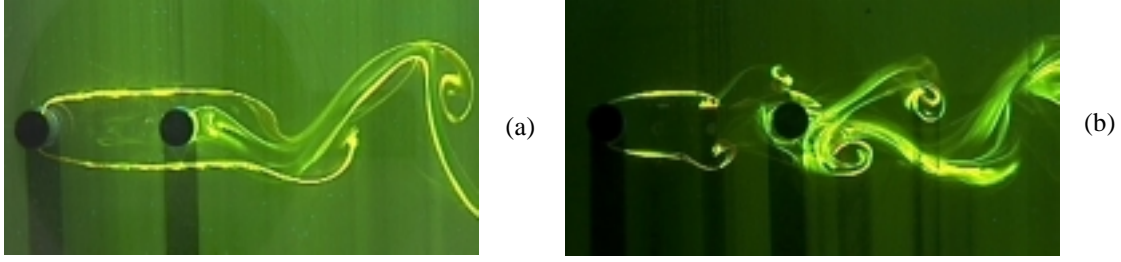


Fig.3: Experimental visualizations at $Re = 200$ for $L/D = 4.0$ (a) and 5.0 (b)

own vertices. The experimental visualization at $Re = 1000$ is shown in Fig. 5 for comparison. When $L/D = 3.0$ (Fig.5a), the shear layers separated from the upstream cylinder transit the inter-space of the two cylinders and no vortex shedding occurs in the front cylinder. When $L/D = 4.0$ (Fig.5b), both cylinders shed vortices.

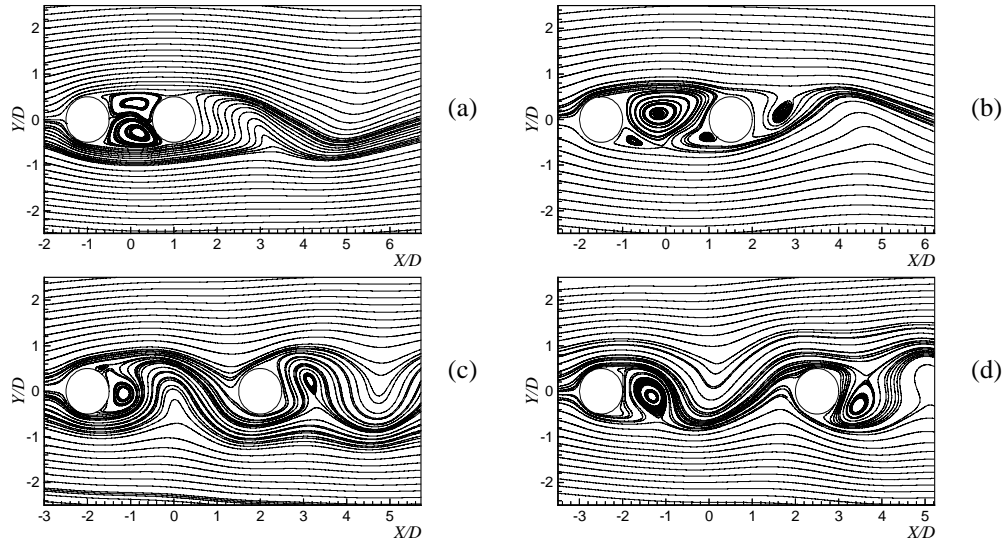


Fig.4: Streamline patterns at $Re = 1000$ for $L/D = 2.0$ (a), 3.0 (b), 4.0 (c) and 5.0 (d)

When the two cylinders are placed in a small spacing ratio in tandem, there is no distinct vortex shedding behind the upstream cylinder. The downstream cylinder experiences a negative drag force and is pushed upstream. When L/D is larger than the critical value, the lift fluctuation of the downstream cylinder is stronger than that of the upstream cylinder. The detailed time series of lift and drag and their spectral analysis are also studied, and will be presented in our later papers.

4. CONCLUSION

A numerical study of two cylinders in tandem in a cross flow has been carried out at $Re = 200$ and 1000 . An operator-splitting time-stepping finite element method is used to solve the flow field. The LIF experiments are conducted to verify the calculated visualization results. The computations and experiments are carried out for four L/D , 2.0 , 3.0 , 4.0 and 5.0 .

The calculations and visualization experiments lead to following conclusions:

- (1) The agreement between numerical and experimental visualization is quite well.
- (2) For $Re = 200$, the critical L/D is between 4.0 and 5.0 . However, for $Re = 1000$, the critical L/D is reduced to between 3.0 and 4.0 due to the instability of high momentum shear layer.

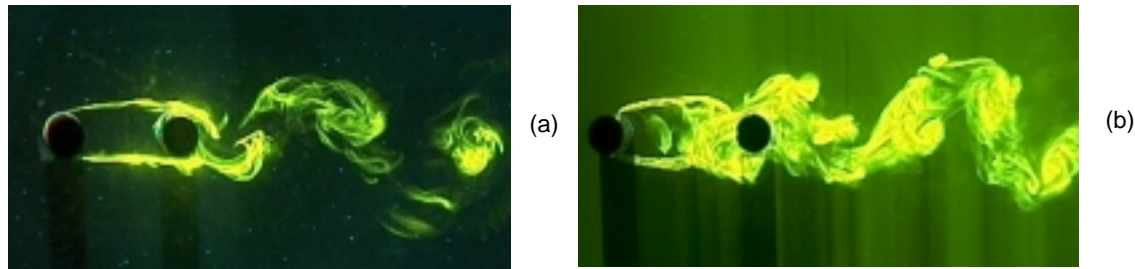


Fig.5: Experimental visualizations at $Re = 1000$ for $L/D = 3.0$ (a) and 4.0 (b)

ACKNOWLEDGMENTS

The authors wish to acknowledge the special funding support by China Institute of Metrology under Grant No. 08-2003.

REFERENCES

- [1] Zdravkovich MM: The effect of interference between circular cylinders in cross flow. *J. Fluids and structures*, 1987, **1**, 239-261.
- [2] Sumner D, Price SJ and Paidoussis MP: Flow-pattern identification for two staggered circular cylinders in cross-flow. *J. Fluid Mech.* 2000, **401**, 263-303.
- [3] Ishigai S, Nishimura X and Cho X: Experimental study on structure of gas flow in tube banks with axis normal to the flow. *Bull. JSME*, 1972, **16**, 949-956.
- [4] Kiya M, Mochizuki O, Ido Y, Suzuki T and Arai T: Flip-flopping flow around two bluff bodies in tandem arrangement. *Bluff-body wakes, Dynamic and instabilities* IUTAM Springer, Berlin, 1992, 15-18.
- [5] Igarashi T: Characteristics of the flow around two circular cylinders arranged in tandem. *Bull. JSME* 1981, **25**, 349-357.
- [6] Zdravkovich MM and Pridden DL: Interference between two circular cylinders; series of unexpected discontinuities. *J. Wind Eng. and Ind. Aerodyn.* 1977, **2**, 255-270.
- [7] Kiya M, Arie M, Tamura H and Mori H: Vortex shedding from two circular cylinders in staggered arrangement. *J. Fluids and Eng.* 1980, **102**, 166-173.
- [8] Gu ZF and Sun TF: On interference between two circular cylinders in staggered arrangement at high subcritical Reynolds numbers. *J. Wind Eng. and Ind. Aerodyn.* 1999, **80**, 287-309.
- [9] Liungkrona L, Norgerg C and Sunden B: Free-stream turbulence and tube spacing effects on surfaces pressure fluctuations of two circular. *J. Fluids and Structures* 1991, **5**, 701-727.
- [10] Arie M, Kiya M, Moriya M and Mori H: Pressure fluctuations on the surface of two circular cylinders in tandem. *J. Fluids and Eng.* 1983, **105**, 161-167.
- [11] Tezduyar TE, Liou J, Ganjoo JDK and Behar M: Solution techniques for the vorticity-stream function formulation of two-dimensional unsteady incompressible flows. *Int. J. Numer. Meth. Fluids* 1990, **11**, 515-539.
- [12] Li J, Chambarel A, Donneaud M and Martin R: Numerical study of laminar flow past one and two circular cylinders. *Computers and Fluids* 1991, **19**, 155-170.
- [13] Li J, Sun J and Roux B: Numerical study of an oscillating cylinder in uniform flow and in the wake of an upstream cylinder. *J. Fluid Mech.* 1992, **237**, 457-478.
- [14] Slaouti A and Stansby P K: Flow around two circular cylinders by the random-vortex method. *J. Fluids and Structures*, 1992, **6**, 641-670.
- [15] Mittal S, Kumar V and Raghuvanshi A: Unsteady incompressible flows past two cylinders in tandem and staggered arrangements. *Int. J. Numer. Meth. Fluids* 1997, **25**, 1315-1344.
- [16] Farrant T, Tan M and Price WG: A cell boundary element method applied to laminar vortex shedding from circular cylinders. *Computers and Fluids* 2001, **30**, 211-236.
- [17] Meneghini JR, Saltara F, Siqueira CLR and Ferrari JA Jr.: Numerical simulation of flow interference between two circular cylinders in tandem and side-by-side arrangements. *J. Fluids and Structures* 2001, **15**, 327-350.
- [18] Jester W and Kallinderis Y: Numerical study of incompressible flow about fixed cylinder pairs. *J. Fluids and Structures* 2003, **17** (4): 561-577.
- [19] Liu Y, So RMC, Lau YL and Zhou Y: Numerical studies of two side-by-side cylinders in a cross flow. *J. Fluids and Structures* 2001, **15**, 1009-1030.

CHARACTERISTICS OF LONGITUDINAL VORTEX FORMED BY RECTANGULAR ORIFICE

H. Abe and H. Yoshida

(Institute for Energy Utilization, National Institute of Advanced Industrial Science and Technology, 305-8564, Japan)

H. Iijima

(Department of Mechanical Engineering, Nihon University, 101-8308, Japan)

ABSTRACT: Longitudinal vortices were artificially formed by using a vortex generator (VG), which consisted of set of two orifices with rectangular cross section. The new VG is supposed to minimize extra flow drags caused by VG itself unlike the solid type vortex generator currently used. Moreover, the new VG can be applicable to various flow conditions, because it is expected to have potential ability for generating vortices with arbitrary sizes and strengths.

1. INTRODUCTION

Control of flow separation is one of the most important fluid engineering subjects and has been widely studied by many researchers.^{1,2)} For the purpose of passive flow control, the solid fin type vortex generators (hereafter, VGs) are often installed on the wings and the intakes of the airplanes. The solid type VGs are known to be useful devices for regulating local flows and suppressing separations.^{3,4)} However, since the solid VGs always extrude into the flow, they are prone to cause extra drags⁵⁾ irrespectively at work and not at work. Moreover, they are not always adaptable to the change of the flow conditions. In this study, we propose a new type of vortex generator without any extrusions and extra flow drags caused by them. This is referred to as the micro jet vortex generator (MJVG).^{6,7)} Aiming at producing longitudinal vortices with arbitrary sizes and strengths, we are developing various types of MJVGs with similar control effects to the ordinary solid type VGs. There are various researches on the flow control by using jets^{8,9)} and synthetic jets.¹⁰⁾ Most authors, however, have paid attention to interaction between the impinging jet and the boundary layer. On the other hand, we are interested in the interaction between longitudinal vortex and boundary layer. Therefore, generating longitudinal vortices is the first step of our research. In this paper we report results of MJVG actuator consisting of a pair of tilted slits under development.

2. METHOD OF EXPERIMENT

Figure 1 shows the schematic diagram of the test section of the open-circuit blower type wind tunnel used for the measurements. The longitudinal vortex is formed in the air by a rectangular orifice¹¹⁾ of 1 x 3 mm flush mounted on a flat plate in a boundary layer as shown in Figure 2. Actually, the orifice has a special three dimensional structure beneath the surface as shown in Fig.2. We have confirmed that two dimensional straight sub-surface structure scarcely generates single longitudinal vortex. The blowing air of the jets is provided by an air compressor. The velocity measurement was conducted by using the hot wire anemometry of I-type. The free stream velocity U_0 was set to be constant as 5.0 m/sec. The laminar boundary layer thickness was 10 mm at the location of the rectangular orifice. At this location establishment of the Blasius type velocity distribution was confirmed. The coordinate system and its origin are set as shown in Figs.1 and 2.

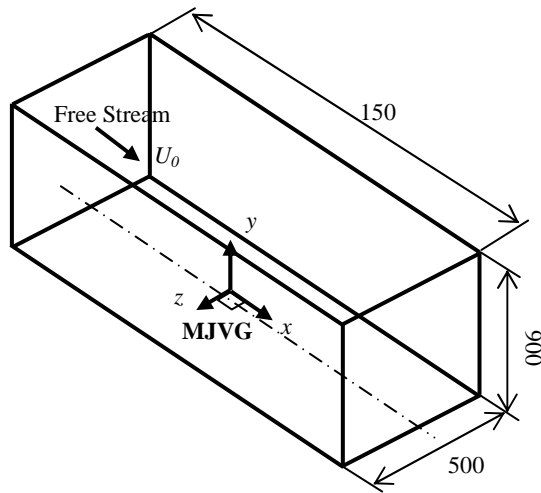


Fig. 1: Sketch of the boundary layer flat plate
in the test section of the wind tunnel

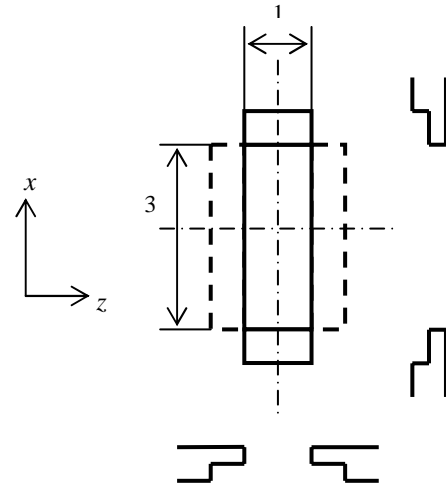
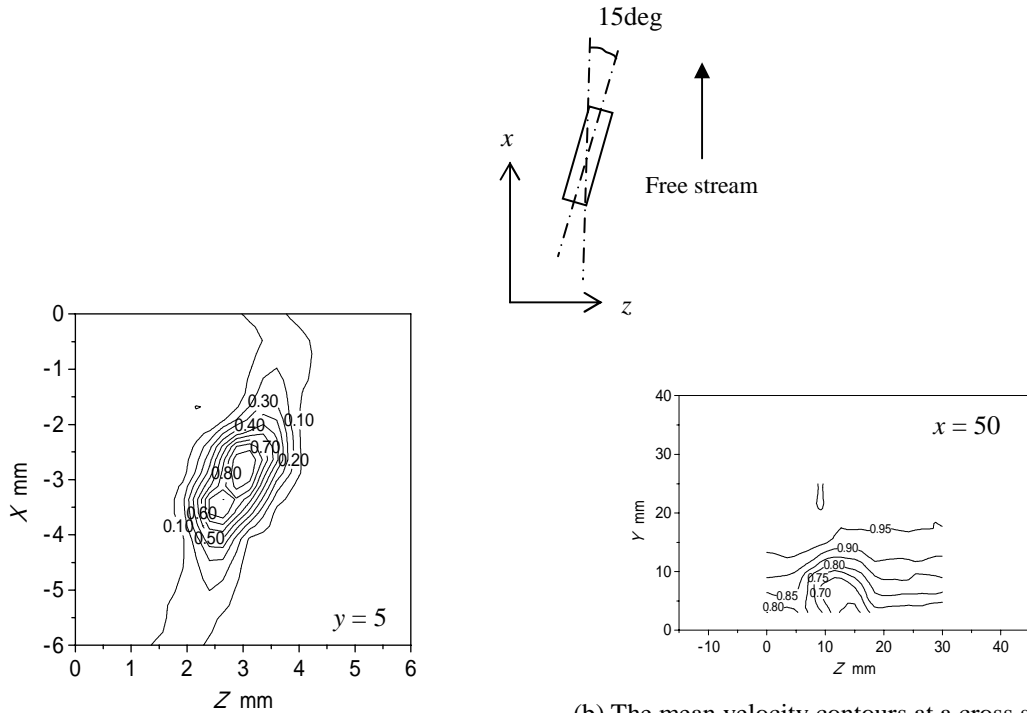


Fig. 2: Sketch of the rectangular orifice

3. RESULTS

Figure 3a shows the jets velocity contours by a single rectangular orifice without mean stream. The maximum jet velocity, V_{\max} , is 10 m/sec. The jet velocity V is normalized by each maximum jet velocity, V/V_{\max} . We have investigated methods of making single longitudinal vortex by jet blowing from wall. Figure 3b shows velocity contour near the wall with free stream $U_0 = 5$ m/sec. Judging from the result shown in Fig.3b, the longitudinal vortex is actually considered to be formed by the shear layer in the left hand side of the two peaks in the contour shown in Fig.3a. The direction of rotation is counter-clockwise because contour of high velocity in left side is closer on wall than right one. However, the shear layer in the right hand side of the peaks in Fig.3a, which directly faces to the free stream, does not form longitudinal vortex. This result means that the incident angle between longitudinal axis of the orifice and direction of free stream, i.e. 15 deg. is very important for formation of single longitudinal vortex. In other words, there seems to be the optimum incident angle for generating an ideal longitudinal vortex. At least we can say that a longitudinal vortex was formed at the angle of 15 deg.



(a) Velocity distribution of jet, $U_0 = 0$ m/sec

(b) The mean velocity contours at a cross section,
 $U_0 = 5$ m/sec

Fig. 3: Velocity distribution of jet and velocity contour at cross section, $V_{\max} = 10$ m/sec

When we install three different pairs of rectangular orifices on the wall in the laminar boundary layer, the downstream flow fields at $x = 50$ mm are like shown in Fig.4. In the following three patterns, distance between vortices is mainly decided by the incident angles of orifices to the free stream. It is not necessarily decided by the pitch of the orifices, in the present cases the pitch is 20 mm. In the case of pattern 1 shown in Fig.4a, a pair of co-rotating vortex appears. In this case, the directions of their rotation are counter-clockwise. In the case of pattern2, shown in Fig.4b, a pair of counter rotating vortices appears.

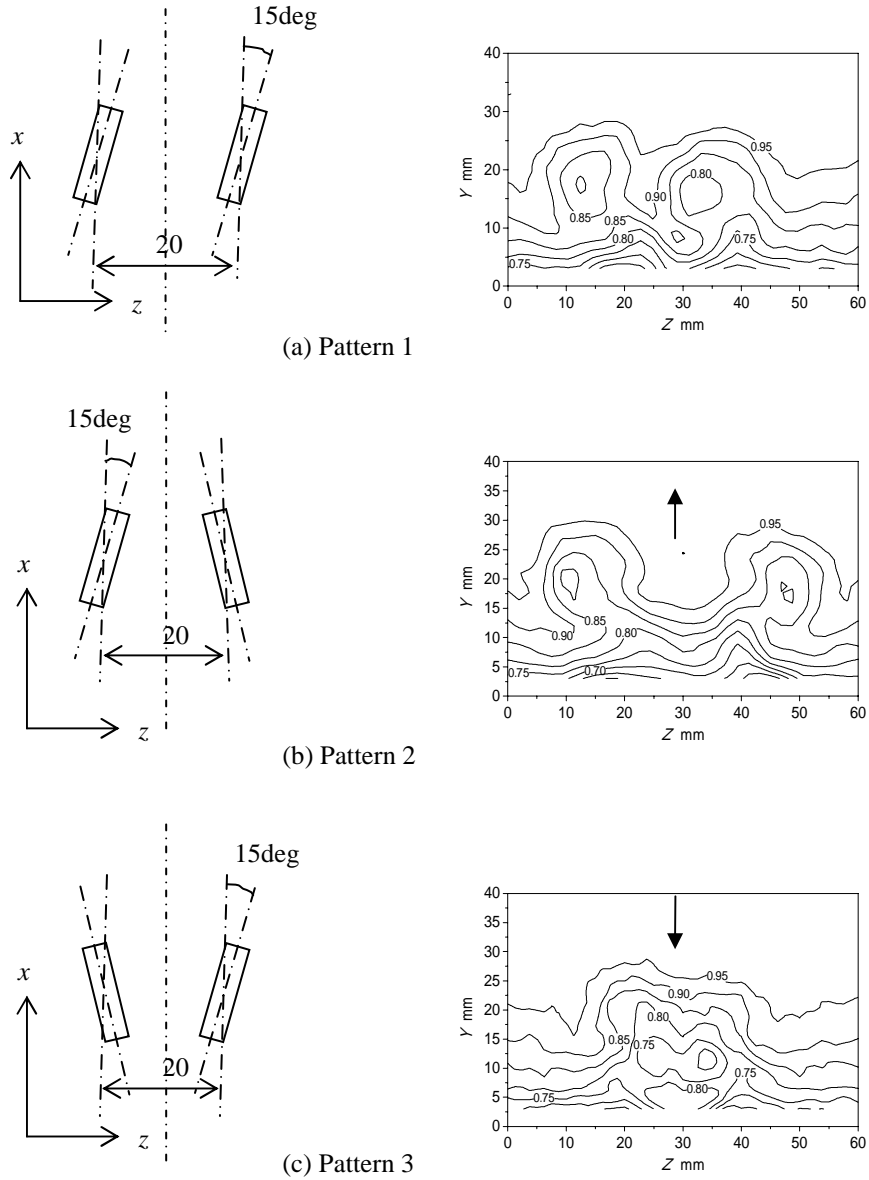


Fig. 4: The mean velocity contours at a cross section of $x = 50$ mm, $V_{max} = 20$ m/sec, $U_0 = 5$ m/sec

Judging from the contour, the boundary layer thickness in the middle point of two vortices seems to be thicker than that in the outside. This means that the clear common-flow-up exists at the middle point. In the case of pattern 3 shown in Fig.4c, the velocity contour shows us a pair of counter rotating vortices. However, in this case down wash seems to occur at the middle point of vortices on the contrary to the case of pattern 2.

4. CONCLUSION

By using a rectangular orifice, we tried to establish a new vortex generator, which has similar flow control effects to the ordinary solid type vortex generators. Through a series of experiments, we found that the present vortex generator can actually generate a longitudinal vortex. In this paper only the experimental facts are reported qualitatively. In future the precise mechanism of the vortex generation will be discussed more quantitatively.

ACKNOWLEDGMENTS

This research was carried out at the Center for Smart Control of Turbulence and funded by the Ministry of Education, Culture, Sports, Science and Technology of Japan through the Organized Research Combination System.

REFERENCES

- [1] Schlichting, H.: *Boundary layer theory*, 7th edition, New York, 1979.
- [2] Gad-el-Hak: *Flow control*, Cambridge University Press, London, 2000.
- [3] Pauley, W.R., and Eaton, J.: Experimental study of the development of longitudinal vortex pairs embedded in a turbulent boundary layer, *AIAA J.*, **26** (1988), pp.816-823.
- [4] Hara, H., Shizawa, T. and Honami, S.: A study of interaction of a pair of longitudinal vortices with a horseshoe vortex around a wing - 2nd report, *Bulletin of JSME B*, **65** (1999), pp.3971-3976 (in Japanese).
- [5] Kusunose, K. and Yu, N.J.: Vortex generator installation drag on an airplane near its cruise condition, *AIAA paper 2003-932*, Reno, January 2003.
- [6] Abe H., Segawa T., Matsunuma T. and Yoshida H.: Micro jet vortex generator for active control of flow separation, *Proc. Int. Conf. on Power Eng'g. ICOPE*, Xi'an, China, Oct. 2001, pp. 1054-1059.
- [7] Abe, H.: Japanese Patent No.2001-058702, 2001.
- [8] Johnston, J. P. and Nishi M.: Vortex generator jets - Means for flow separation control, *AIAA J.*, **28** (1990), pp. 989-994.

- [9] McCormick,D.C., Lozyniak,S.A., McMartin,D.G, Lorber,P.F.: Compact, high-power boundary layer separation control actuation development, Proc. *ASME FEDSM2001-18279*, 2001.
- [10] Glezer,A., Amitay,M.: Synthetic jets, Annual Rev. *Fluid Mech.* **34** (2002), pp.503-529.
- [11] Japanese Patent proposed.

LARGE SCALE MOTIONS INDUCED IN EDGE-TONE PHENOMENA

Y.Kawai, Y.Tsuji and Y.Kukita

Department of Energy Engineering & Science, Nagoya University, Nagoya 464-8603, Japan

ABSTRACT: Coherent large scale motions induced in a turbulent jet impinging on a flat plate are studied in this paper. This kind of flow is well known as accompanying a large-scale eddies. It is called an edge-tone phenomenon and appears in various cases in industrial applications. The edge-tone noise is generated by these eddies enhanced in the flow. In order to reduce the loud noise, we first have to identify eddies and then control them. It is reported in this study that the coherent eddies are well captured using the wavelet analysis and their contribution to turbulence energy is analyzed by mean of three decomposition analysis and conditional sampling.

1. INTRODUCTION

Impinging turbulence is usually observed in the industrial facility. When the turbulence jet collides the sharp body, we observe the edge-tone phenomena, which is due to the boundary instability inside the nozzle exit and the feedback system from the sharp body. As the edge tone is generated by the vortex pairs beside the sharp body, most attempts have been made so far to reduce the noise by intercepting them.^{[1][2]} It is generally accepted that large vortexes are effectively controlled by the initial condition at the nozzle and then the noise level is dramatically decreased.^[2] However, it is not clear how to identify the large scale vortex and how much they contribute to the total turbulence energy. In this study, using the wavelet analysis, we characterize these eddies and quantitatively analyze the turbulence energy contained in them by means of three-decomposition procedure.

In this flow field a flat plate is attached in the developed two-dimensional turbulent jet. The free jet collides the edge of the plate and then the wall jet is developed on it. We have mostly paid attention to the turbulence fluctuation level on the plate and its relation to the large vortex pairs caused by the edge tone. In the previous analysis^{[3][4]}, edge-tone eddies are conditioned by Fourier series. It was found that the edge-tone eddies can survive far away from the edge, and they have a significant contribution to the turbulence level. Kolmogorov scale is independent of edge-tone eddies but the integral length scale is not.^[5] This result indicates that the edge-tone is restricted mostly by the macroscopic flow conditions. Here, the eddies are conditioned by the wavelet. It is better because the eddies are randomly localized in space and in time. The final goal is to realize the enhancement of heat transfer rate on the plate by using the edge-tone eddies. This may be a useful application from the point of engineering for the multi jet cooling of arrays of electronic packages, the impingement cooling of the inner surfaces of turbine blade, and the impingement drying of textile, paper, film and so on.

2. EXPERIMENTAL CONDITIONS

The experiments were carried out by a wind tunnel of blow-down type. Its nozzle exit size is 10mm × 200 mm. This wind-tunnel consists of four parts, which are blower, diffuser, setting-chamber, and contraction-nozzle. The blower is directly connected to the three-phase AC-motor with 0.4 kW, and the normal flow rate is 18m³/min. The setting-chamber is a square of 200 mm per a side which has a honeycomb and three mesh screens in order to reduce the turbulence intensity. The interval between each screen is set at the length of more than hundred times of mesh size. The aspect-ratio of construction nozzle is 20, thus the two-dimensionality is achieved enough.

The flat plate has the dimension of 735 mm in length, 200 mm in width, and 6 mm thickness. This plate is fixed in the position of self-preserving area in jet, where it is 200 mm from the nozzle exit when the Reynolds number is $Re \equiv U_j \cdot b_j / \nu = 22000$. The plate is made of a bakelite due to decreasing the cooling effect by the hot-wire at close to the wall. The leading edge is in the shape of ellipse recommended by Narashimha because it doesn't generate a separation when the jet flow collides the plate. Velocity fluctuations are measured by a I-type probe operated by a constant temperature anemometry. Data are sampled by 10kHz for thirty second and they are digitized by 12-bit A/D converter.

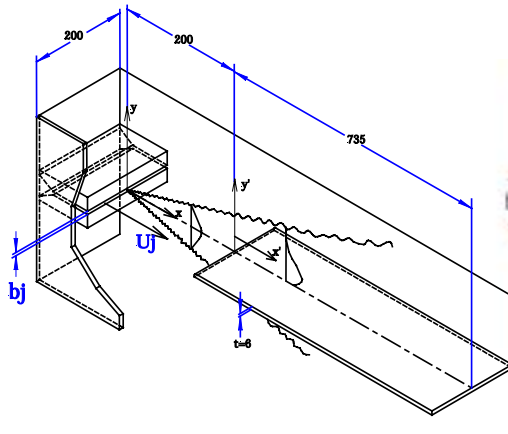


Fig. 1: Detail sketch of test section.

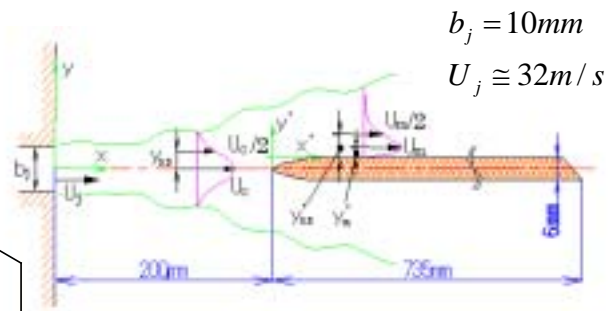


Fig. 2: Schematic view of experimental facility and the coordinate system.

2.1 NOMENCLATURE

b_j : Height of the nozzle exit. U_c : Mean velocity on the centreline as a function of x .

U : Mean velocity in the direction of x . U_j : Mean velocity at the nozzle exit.

u : Velocity fluctuation in the direction of x . u' : Root mean square value of u .

U_m : Maximum mean velocity on the wall as a function of x' .

$y_{0.5}, y'_{0.5}$: Location from the centreline where the local mean velocity equals to the half of U_c or U_m .

x, y, z : Coordinate system with its origin at the nozzle exit.

x', y', z' : Coordinate system with its origin at the leading edge of flat plate.

3. WAVELET ANALYSIS

The orthogonal wavelet expansion of a function $f(t)$ takes the flowing form

$$f(t) = \sum_j \sum_k d_k^{(j)} \phi_{j,k} \quad , \quad d_k^{(j)} = \int_{-\infty}^{+\infty} \phi_{j,k}(t) f(t) dt \quad (1)$$

where $d_k^{(j)}$ ($j, k \in Z$, where Z is the set of all integers) is an expansion coefficient and $\phi_{j,k}$ is a complete orthogonal data set of wavelets generated from an analyzing wavelet $\phi(t)$ by discrete transformation and

discrete dilations. It is usual to take the discrete dilation in octaves, and to make the wavelet as follows

$$\phi_{j,k}(t) = 2^{j/2} \phi(2^j t - k) \quad (2)$$

with the orthonormality condition

$$\int_{-\infty}^{+\infty} \phi_{j,k}^*(t) \phi_{j',k'}(t) dt = \delta_{jj'} \delta_{kk'} \quad (3)$$

where δ_{ij} is the Kronecker's symbol. Note that j is the dilation parameter and k indicates the temporal position of time in the form of $k/2^j$. The analyzing wavelet constructed by Daubechies is used here. In this study, total data point 262144 is divided into $4096 = 2^{12}$ points data box. Then the dilation parameter is $1 \leq j \leq 11$. Its relation to the Fourier frequency is listed in Table 1 for convenience.

Wavelet dilation parameter j	1	2	3	4	5	6	7	8	9	10	11
Fourie frequency	4.9	9.8	20	39	78	156	312	625	1250	2500	5000

Table. 1 Relation between wavelet dilation parameter and Fourier frequency.




4. THREE DECOMPOSITION ANALYSIS

Instantaneous velocity fluctuation \tilde{u} is usually decomposed into its mean U and fluctuation u' . If the periodic motions or some organized motions are contained, the contribution from these is expressed by u_θ and the rest of u' is expressed as u_s .

$$\tilde{u} = U + u' = U + u_\theta + u_s \quad (4)$$

The periodic component u_θ is reconstructed by means of wavelet transform instead of Fourier expansion. Because the contained periodic motion is not exactly periodic. Then the wavelet basis is better than that of Fourier expansion in which the orthogonal basis are not localized in space and in time.

5. RESULTS AND DISCUSSIONS

It is actually observed that a periodic motion is caused by edge-tone eddies. In the frequency spectrum, as is shown in Fig. 3, there are sharp spikes at 40 Hz and 80 Hz. These frequencies are significantly affected by the nozzle exit velocity U_j and the distance between nozzle and leading edge L . The contour of two peak frequencies is plotted in Fig.4. The edge of the plate is located at $(x, y) = (200, 0)$. Broken line indicates half-value position $y_{0.5}, y'_{0.5}$. Each frequency region is bounded by slash mark. The mark  indicates 40Hz region,  is 80Hz,  is express both frequencies. It was found that both frequencies exist in wide range in front of the edge and above the plate. In front of the leading edge, where the each region become widely to downstream, but they get narrow on the plate in the downstream. It is noted the 40 Hz peak is observed even in the extent far away from the leading edge until $x = 650$ mm. This indicates that the edge-tone eddies can survive over the flat plate in the downstream and have an effect on the flow.

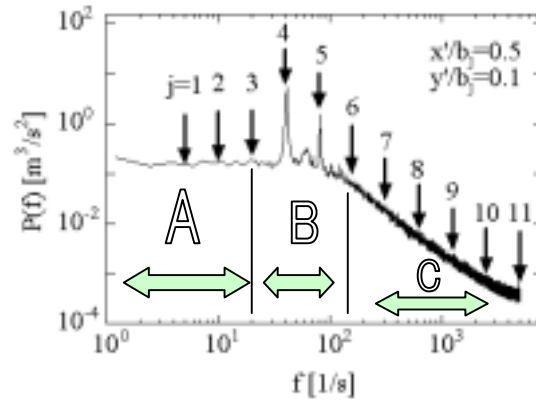


Fig.3: Power spectrum of velocity fluctuation at $(x'/b_j, y'/b_j) = (0.5, 1.0)$.

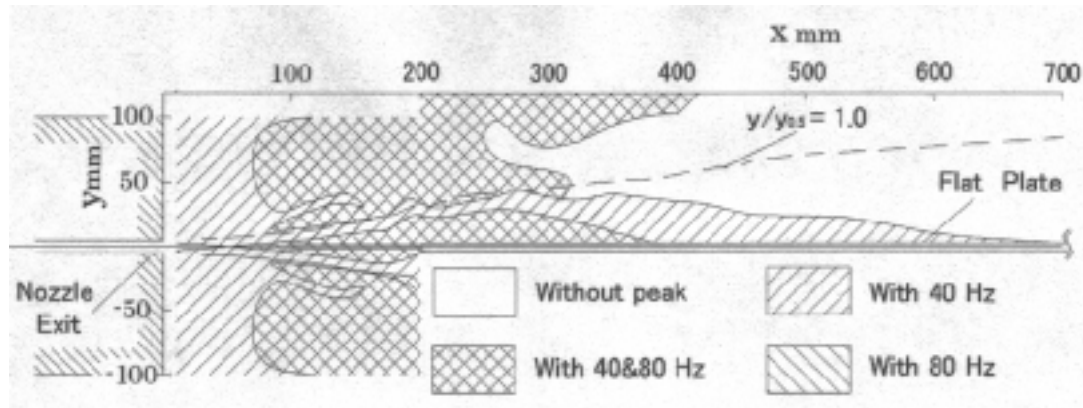


Fig. 4: Contour of peak frequency in the velocity spectrum. Two different frequencies are observed . The brokenline indicates the location where the local mean velocity is equal to the half of the center line velocity.

The velocity fluctuation is decomposed in to each dilation sector by way of Eq. (1). Typical example is shown in Fig.5. Here, $j=0$ indicates the original signal and the smaller j values represent the larger fluctuations. Watching these signals, we find that the periodic motions are captured by $j=4,5,6$ and small random fluctuations are reconstructed by $j=7,8,9,10,11$. On the other hand, $j=1,2,3$ component seem to depend on the large-scale motions.

The frequency space is divided into three different regions. They are indicated in Fig.3 and are named as A; $j=1,2,3$, B; $j=4,5,6$, and C; $j=7,8,9,10,11$, respectively. Therefore, the non-periodic motions consist of A and C or the component u_s is written as follows.

$$u_s = u_1 + u_2 \quad , \quad u_1 = \sum_{j=1}^3 \sum_k d_k^{(j)} \phi(2^j t - k) \quad , \quad u_2 = \sum_{j=7}^{11} \sum_k d_k^{(j)} \phi(2^j t - k) \quad (5)$$

It is emphasized here again that we use the discrete wavelet decomposition instead of Fourier transform. It is because the localized structure in time can be conditioned.

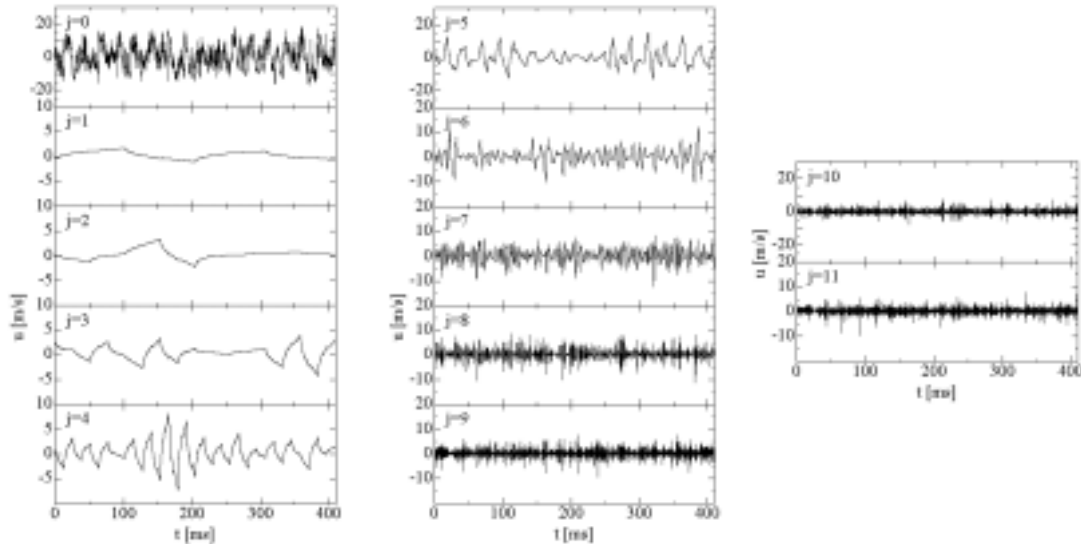


Fig.5 Typical example of wavelet decomposition for each j sector. Here, $j = 0$ indicates the original signal and smaller j values represent the larger fluctuations. The periodic motions are reconstructed by $j = 4, 5, 6$.

The turbulence intensity is considered by mean of three decomposition analysis. The root mean square value of u' , u_1 , u_θ , and u_2 are plotted in Fig. 6. The component u' has a large value around the edge, but decreases downstream while the strong intensity remains closer to the wall. As Fig. 6(a) and (c) are qualitatively similar with each other, the periodic component has the significant contribution to u' . The large scale anisotropic component u_1 indicates small value near the leading edge, but the component u_2 indicates large, because the small scale fluctuations are generated by the interaction of jet and the leading edge. This situation is well captured by Fig. 6(b) and (d). The solid line is the location where the mean velocity becomes half. The distribution of u_θ conditioned by edge-tone frequency is plotted in Fig. 7. It is clear that the edge-tone eddies are captured and they move in the downstream. They have a large intensity near the wall and survives until far away from the edge. This result is consistent with Fig. 4 in which the peak frequency of 40Hz exist until $x = 650$ mm.

6. CONCLUSIONS

Coherent eddies generated by edge-tone are well captured by wavelet decomposition. They can survive on the flat plate far away from the leading edge until $x = 650$ mm. They have a significant contribution to turbulent intensity u' . If the non-periodic component u_s is decomposed into u_1 and u_2 , where u_1 represents large scale and u_2 are small scale, u_1 develops downstream similar to the location $y'/y'_{0.5} = 1.0$. On the other hand, u_2 has large intensity around the edge and decreases gradually in the downstream. Conditioning the component u_s , the edge tone eddies are clearly identified on the plate. They indicate large turbulence intensity close to the wall region.

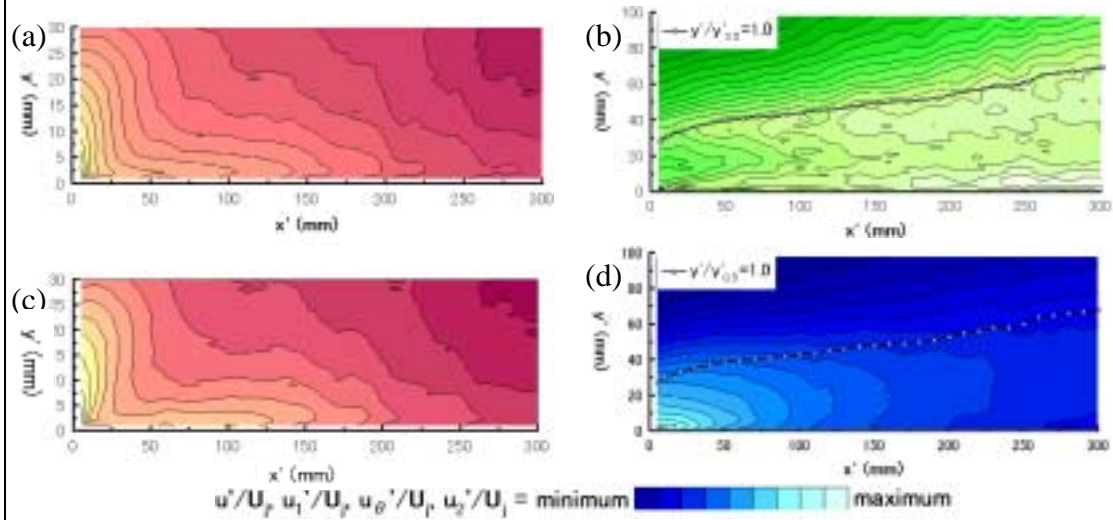


Fig. 6 Contour map of r.m.s. of each component over the flat plate. (a) u' , (b) u_1 , (c) u_θ , (d) u_2 -component.

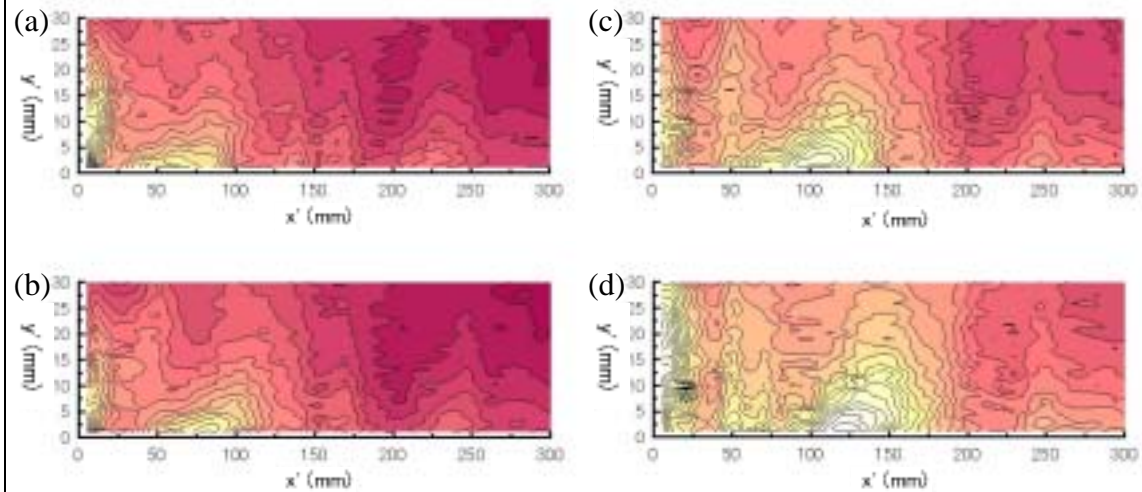


Fig. 7 Contour map of u_θ conditioned by edge-tone frequency. (a) $T/8$, (b) $2 \cdot T/8$, (c) $3 \cdot T/8$, (d) $4 \cdot T/8$

REFERENCES

- [1] D. Rockwell, In proceedings of International Symposium on Nonsteady Fluid Dynamics, FED-Vol.92, p379
- [2] S. Ziada, J. Fluid and Structures, Vol.9(1995), p907.
- [3] Y.Kawai, H.Yamada, Y.Tsuji and Y.Kukita, Impinging Shear Flow and Edge-tone Phenomena; Enhancement of Heat Transfer Rate and its Possibility, Proc. 3rd Int. Sym. On Advanced Energy Conversion Systems and Related Technology, Dec.15-17, Nagoya (2001), CD-ROM publications.
- [4] Y.Kawai, Y.Tsuji and Y.Kukita, Scale of vortex structure and turbulence property in impinging jet, submitting to

FLOW CHARACTERISTICS OF SINGLE-LOBE FORCED MIXER

S. Yu and R. Mao

School of MPE, Nanyang Technological University, Singapore, 639798

ABSTRACT: In the present experimental investigation the characteristics of two types of vortices, namely the normal Kelvin-Helmholtz and streamwise vortices, generated in the near wake of single-lobe forced mixer have been examined and evaluated at two velocity ratios, $r = U_1/U_2 = 1:1$ and $0.4:1$. The single-lobe mixer was designed to eliminate the interaction between the neighboring vortices generated by the adjacent lobes ^[1]. Hot-wire anemometry was used to study the Kelvin-Helmholtz vortices, using spectrum analysis; while laser Doppler anemometry was employed to study the streamwise vortices. It was found that there were two main frequencies for the Kelvin-Helmholtz vortex in the wake of the lobe forced mixer; and both of them were higher than the case of plane free shear layer. For the single-lobe forced mixer flow, the Strouhal Numbers increase with the Reynolds Number while increasing the velocity ratios cause the Strouhal Number to decrease gradually. Consequently the Strouhal Numbers would reach certain constant values at high Reynolds Number. The initial mean streamwise vorticity and the subsequent decay were almost the same for the two velocity ratios.

KEYWORDS: Two-stream mixing, single-lobe forced mixer, Kelvin-Helmholtz vortex, vortex shedding frequency, hot-wire anemometry (HWA), streamwise vortex, laser Doppler anemometry (LDA).

1. INTRODUCTION

Two-stream mixing is one of the most important and popular topics among many research areas in fluid mechanics. It is well established that vorticity dynamics affect and control the mixing process to a great extent. Through proper design of the splitter plate geometry lobe forced mixer is one typical example to generate strong streamwise vortices in the mixing layer. Besides the streamwise vortices, the small scale Kelvin-Helmholtz vortices would also be generated simultaneously, due to the velocity difference between the two mixing streams. Many researchers, for example Povinelli *et. al.* (1980), Paterson (1982, 1984), Presz *et. al.* (1987), Barber *et. al.* (1988), Eckerle *et. al.* (1992), Presz *et. al.* (1994) and Yu *et. al.* (1997, 1999), have studied the fluid dynamic characteristics of the lobe forced mixer. In their investigations, the gross features of the flow field were investigated, with particular attention to the streamwise vortices. McCormick and Bennett (1993)^[2] used smoke injection technique and triple-sensor hot-film probe to study the vortical and turbulent structure of lobe forced mixer flow. By measuring the mean wavelength of the KH vortices and comparing with plane free shear layer, they found that the scale of the K-H vortices shed from the trailing edge of the lobe forced mixer was about

one-fourth of the planar case. This finding was exciting, but only one flow condition has been tested. The objectives of the present project are to examine the individual characteristics of the K-H vortices and the streamwise vortices respectively. This is important to understand the enhanced mixing performance of the lobe forced mixer, and the information would be helpful to design lobe forced mixers with more efficient mixing performance.

2. EXPERIMENTAL ARRANGEMENTS

The experiments were carried out in an open circuit, suction type wind tunnel located in Thermal and Fluids Research Laboratory, Nanyang Technological University. The wind tunnel is a low-speed wind tunnel; with the test section 200 mm high, 200 mm wide and 500 mm long. The turbulence level of the on-coming streams at either side of the splitter plate is about 1%. The temperature of the air is kept constant at $T = 20^\circ\text{C}$ during the whole course of the experiments. There is a flat splitter plate embedded on the centerline to separate the airflow into two same parts. By incorporating two different course of screens on the upper and lower half of the bell mouth, the velocities of the upper (U_1) and lower (U_2) streams can be varied from 0 to 10.4 m/s. Two velocity ratios ($r = U_1/U_2$) 1:1 and 0.4:1 have been carried out, with the Reynolds Number varying from 9,200 to 40,000, which based on the mean velocity of the on-coming flows and the wavelength of the mixer model ($I = 60\text{ mm}$):

$$Re = \frac{\bar{U} \times I}{\nu} \quad (1)$$

The model was mounted at the end of the flat splitter plate on entry to the test section of the wind tunnel. A flat splitter plate has been tested in spectrum analysis as a baseline for comparison, which was to simulate the plane free shear layer. The forced mixer model tested in the present investigation has only one lobe, so as to eliminate any possible interactions between neighboring lobes, as shown earlier in the experiments of Yu and Yip (1997). The geometry of the mixer model is shown in Fig. 2, which is made of 2 mm thick fiberglass with blunt trailing edge. The model has parallel sidewalls and semi-circular trailing edge.

Because the frequency response of the Constant Temperature Anemometer (CTA) is high enough in the present experiments, hot-wire together with CTA have been utilized successfully to measure the K-H vortex shedding frequencies. Laser Doppler anemometer (LDA) has been used to evaluate the streamwise vortices. Fine water particles with the size 5~10 μm generated by a commercial nebulizer were used to seed the airflow. Three-orthogonal mean velocities (\bar{U} , \bar{V} and \bar{W}) together with their corresponding *rms* fluctuations (u' , v' and w') have been acquired in the project, with the measuring area corresponding to $-0.75 \leq y/I \leq +0.75$, $-1 \leq z/I \leq +1$ and at eight downstream locations.

3. RESULTS AND DISCUSSION

3.1 Kelvin-Helmholtz Vortices

3.1.1 Vortex Shedding Frequency

For the flat plate, the K-H vortex shedding frequency was in direct proportion to the mean velocity, provided the velocity ratio kept constant; while for the lobe forced mixer, due to the complex velocity fields, there were always two main frequencies in the wake, as revealed in the measurements. Referring to Fig. 2, for the regions in the wake of the semi-circle part of the trailing edge, the dominant frequency was the same in this region, as referred to as f_C ; while for the regions behind the parallel side-walls of the trailing edge, the dominant frequency was the same too, as expressed as f_L . For the same on-coming flow conditions, f_C was always higher than f_L ; and both of these two frequencies were higher than that of the flat plate.

3.1.2 Roshko Number

The Roshko number is usually adopted to correlate periodic wakes, which is non-dimensional frequency defined as:

$$Ro = \frac{f \times l^2}{g} \quad (2)$$

It is found that for both point C and L, the individual Roshko Number varies linearly with the Reynolds Number (increase from 9,200 to 40,000) in the present investigation. At point C and velocity ratio $r=0.4$ for example, the Roshko Number varies as below:

$$Ro_c = 13.1 Re - 76300 \quad (3)$$

3.1.3 Strouhal Number

The Strouhal Number of the flat plate was found to be constant, i.e., 0.031 ± 0.002 , which was based on the mean momentum thickness of the upper and lower boundary layers. This result fits well with the CFD result of Monkewitz and Huerre (1982)^[3].

For the forced mixer, the Strouhal Number is defined as the ratio of the nominal length (l) to the mean wavelength of the K-H vortices here:

$$St = \frac{f \times l}{U} = \frac{l}{l_{KH}} = \frac{Ro}{Re} \quad (4)$$

As shown in Fig. 3, the Strouhal Number increases with the Reynolds Number while the increase in velocity ratio comes a decrease. At point C and velocity ratio $r=0.4$ for example, the Strouhal Number variation is:

$$St_c = 13.1 \frac{76300}{Re} \quad (5)$$

Stable values of Strouhal Number can normally be achieved at Reynolds Number higher than 10^5 . The velocity ratio affects Strouhal Number behind point C more significantly than behind point L.

3.2 Streamwise Vortices

The mean streamwise vorticity can be normalized as follows:

$$C_I = \frac{\Gamma}{U \times l} \quad (6)$$

in which Γ is the streamwise circulation of the plane **I**, where **I** encompasses half lobe:

$$\Gamma = \oint_I \mathbf{w} \times d\mathbf{A} = \oint_I U_s \times dl = \int_{AB} \bar{V} \times dy + \int_{BC} \bar{W} \times dz + \int_{CD} \bar{V} \times dy + \int_{DA} \bar{W} \times dz \quad (7)$$

The results of the normalized streamwise circulation for the two cases are plotted in Fig. 4. As measured by LDA, their initial magnitudes of mean normalized streamwise vorticity were of little difference. The circulation decreased almost exponentially for both two cases.

4. CONCLUSIONS

Hot-wire anemometry and laser Doppler anemometry have been employed in the present investigation to measure and evaluate the respective characteristics of the Kelvin-Helmholtz vortex and the streamwise vortex generated in the wake of single-lobe forced mixer, with two velocity ratios, 1 and 0.4.

- (1) There are two dominant K-H vortex shedding frequencies in the wake of the forced mixer flow. Both of them are higher than the plane free shear layer.
- (2) The two Strouhal Numbers of the single-lobe forced mixer flow increase with the Reynolds Number while the increasing ratios decrease gradually until the Strouhal numbers reach certain stable values.
- (3) The initial magnitude of the mean streamwise vorticity and the subsequent decay rate are almost the same for the two cases with different velocity ratios.

ACKNOWLEDGEMENTS

The authors wish to acknowledge the graduate scholarship from the school of MPE, NTU for Mr. Mao.

REFERENCES

- [1] Yu SCM and Yip TH. Measurements of velocities in the near field of a lobe forced mixer trailing edge. *The Aeronautical J. of the Royal Aeronautical Society*, 1997, No. 2165: 121-129
- [2] McCormick DC and Bennett Jr JC. Vortical and turbulent structure of a lobe mixer free shear layer, *AIAA J*, 1994, **32**(9), 1852-1859
- [3] Monkewitz PA and Huerre P. The influence of the velocity ratio on the spatial instability of mixing layers, *Phys. Fluids*, 1982, **25**:1127-43

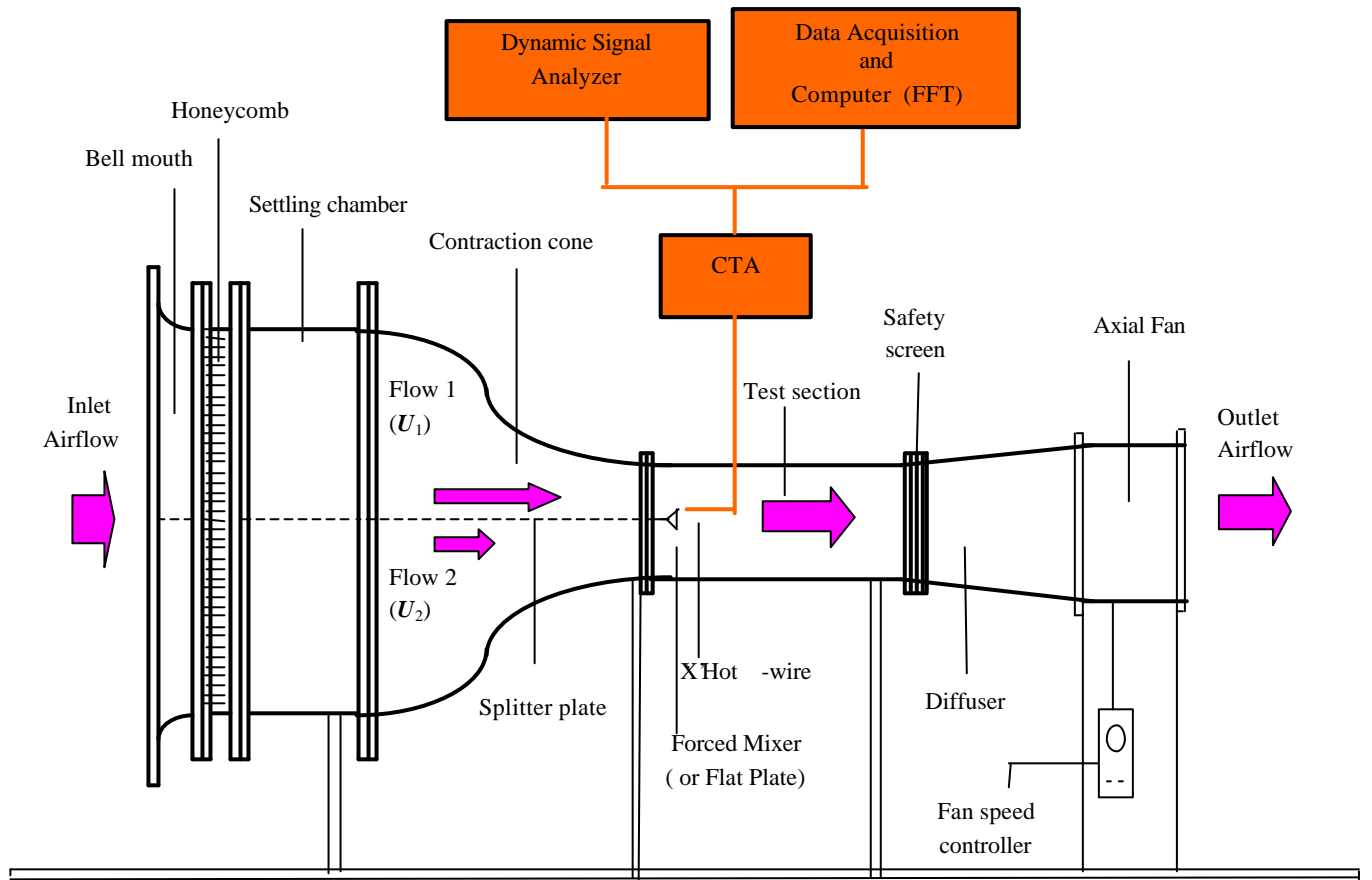


Fig. 1: Experimental arrangements

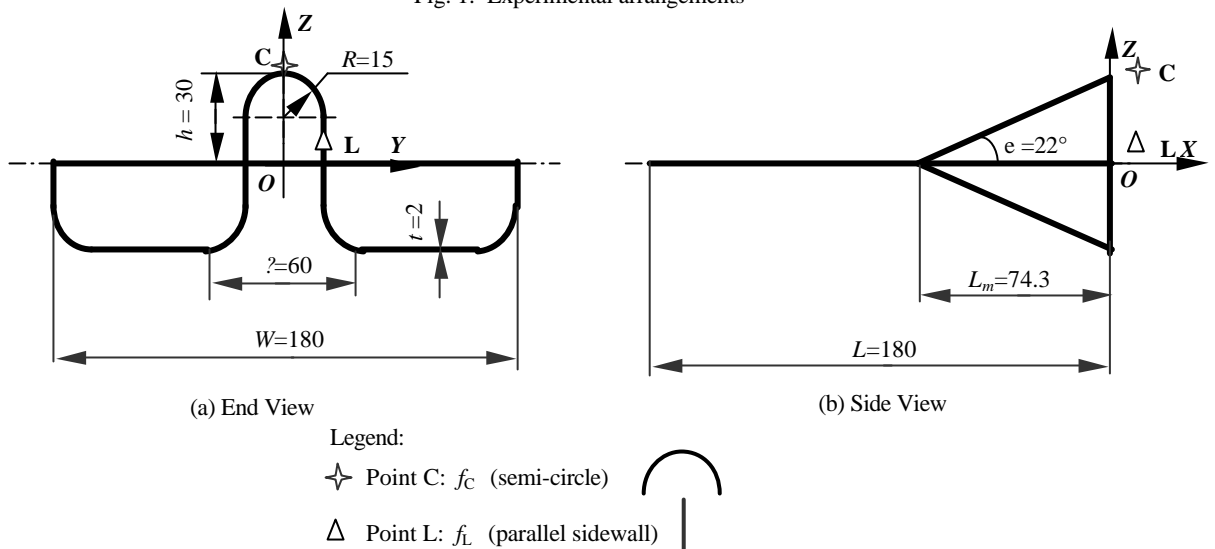


Fig. 2: Schematic diagram of the single-lobe forced mixer (dimensions in mm) and locations of the two dominant frequencies in the near wake flow

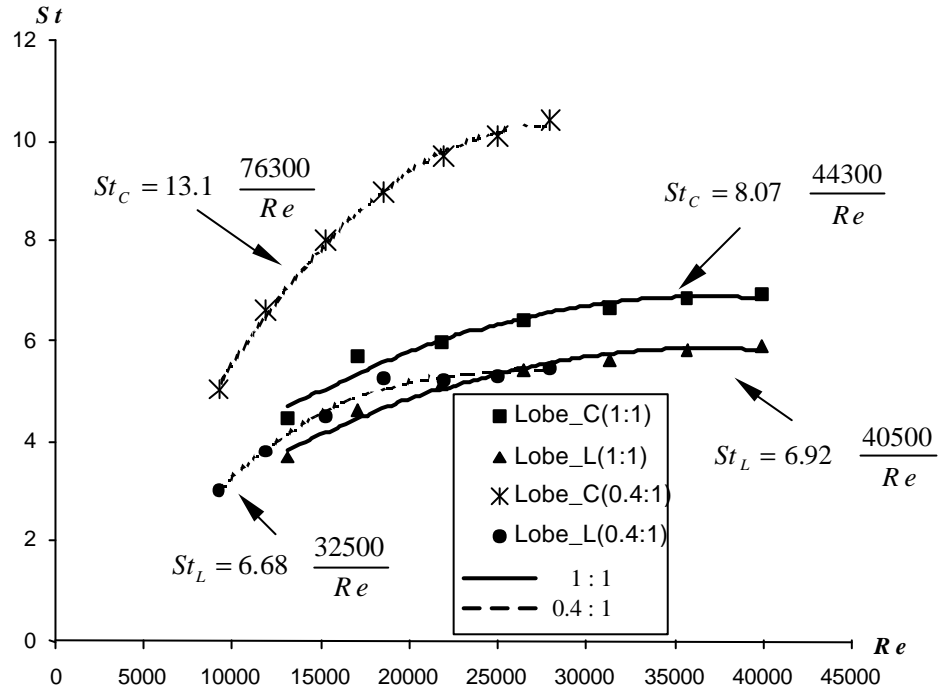


Fig. 3: The Strouhal Number variation with the Reynolds Number for the single-lobe forced mixer (Lobe_C and L)

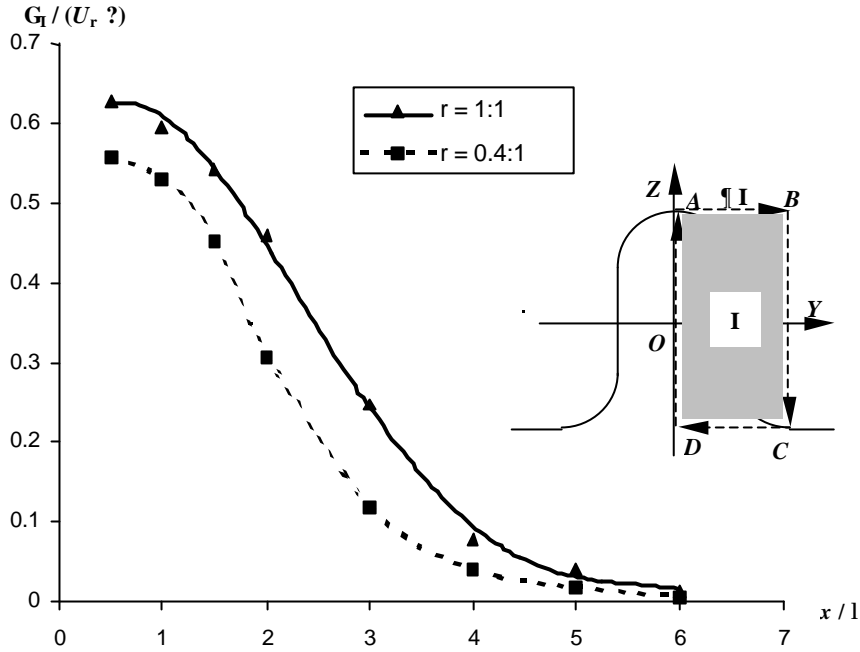


Fig. 4: Variations of the normalized streamwise circulation with downstream distance after the trailing edge of single-lobe forced mixer